Recurrent Spatio-Temporal Snowmelt Patterns: Synthesis and Application Over the Snake River Basin

A Dissertation
Presented in Partial Fulfillment of the Requirements for the
Degree of Doctor of Philosophy
with a
Major in Biological Engineering
in the
College of Graduate Studies
University of Idaho
by
Craig D. Woodruff

Approved by:
Major Professor: Russell J. Qualls, Ph.D.
Committee Members: Karen Humes, Ph.D.; Dev Shrestha, Ph.D.; Sarah Wu, Ph.D.
Department Administrator: Dev Shrestha, Ph.D.

May 2022

Abstract

Snow is a vital component of available freshwater world-wide. Remote sensing of snow offers daily world-wide imagery at moderate resolutions; however, the data availability is reduced due to cloud coverage. The spatial and temporal availability of remote sensing allows us to extract the recurrent pattern of snowmelt. Patterns are exceptionally useful for snowmelt runoff modeling. In this work, we expand, apply, and determine sensitivities of these patterns to better understand and utilize them. The recurrent spatial pattern of snowmelt can be extracted with multiple years of remotely sensed data with a Principal Component Analysis (PCA), which we term the PCA Model. The qualities of the PCA model allow us to represent snowmelt linearly in time over 16 years (r-squared 0.946 - 0.992). With a linear and repeatable relationship, we can normalize snowmelt and compare of multiple years and adjust snow depletion for secondary snowfall events. We also use another multivariate technique to extract the recurrent pattern of snowmelt. The K-means Cluster method produces a model of the recurrent pattern of melt which can be used to remove cloud cover with spatial accuracies of 84.6 – 96.0% when compared against independent data. Sensitivities of the PCA model to user decisions were investigated. By varying the user decision of what is considered snow or no snow we increased average spatial accuracies of the PCA model versus cloud free (<10% cloud cover) images from the previously published 92.61% to 95.46%. Spatial and temporal scaling sensitivities of the model were also presented. The model performs with excellent average spatial accuracy (>90%) when compared against four years of independent data for large Hydrologic Unit Code (HUC) 6 boundary sizes. An analysis of the number of years required to develop a robust pattern demonstrated with only three years the pattern captured by the model is exceptionally similar with minimum correlations greater than 0.97. The intrinsic attributes of PCA model are a significant step forward in understanding and spatially representing snowmelt.

Acknowledgments

I would like to thank Dr. Russell Qualls for his guidance throughout my graduate career. He has helped me develop professionally and academically. I would also like to thank my committee members Dr. Humes, Dr. Shrestha, and Dr. Wu. They have given me valuable guidance in writing my dissertation, coursework, and directed me to helpful resources. Many of the chapters in this thesis are based on skills I acquired in coursework suggested by the committee members. This research was supported in part by USDA-NIFA Hatch project No. IDA01584, and Idaho Water Resources Research Institute and the DOI USGS grant number G16AP00050. Lastly, I would like to thank the Department of Biological Engineering for guidance throughout my time and the supportive atmosphere conducive to successful completion of this degree.

Dedication

I could not have completed this degree without the continued love and support of my parents Roger and Dawna, brothers Scott and Douglas, and partner Kayla. The ups and downs of this most difficult task have been made smoother by each one of you. I would like to dedicate my work to my grandparents Don and Cleo Lenz. I have tried to approach my research with the pragmatic approach they instilled in me. You will always live on.

Table of Contents

List of Tables

List of Figures

List of Equations

Chapter 1: Introduction

Literature Review

The Current State of Snow Monitoring

Snow is a vital source of water storage with metered delivery through the melting period. 75% of the annual runoff in the Western United States comes from snowmelt (Balk & Elder, 2000). Worldwide, well over half of the potable water supply is extracted from rivers, and with a changing climate, there will be a shift in the timing and availability of water in snowmelt driven watersheds (Barnett et al., 2005). Managing this finite resource requires accurate modeling of snowmelt runoff, which relies on the availability and quality of data. Snow monitoring through snow course and snow pillow (SNOTEL) sites has been foundational to understanding snowmelt. These monitoring practices capture snow water equivalent (SWE), snow depth, and sometimes atmospheric conditions. The setback to this highly accurate method is spatial coverage. Spatial availability often limits the whole picture of snowmelt. Satellite based remote sensing has complete spatial coverage, but it lacks the finer accuracy. Both ground-based and remotely sensed data can collect SWE, but both are hindered by spatial and temporal availability. Remote sensing captures snow covered area (SCA) as well, and in this research that is what we use remotely sensed SCA. This is data is valuable and chosen because snow location helps to accurately model the energy fluxes that drive snowmelt.

The most relevant question to ask about this research is why are we focusing on SCA instead of SWE? SWE measurements are recorded in two ways. As stated above, remote sensing and ground-based methods are available, but both methods have limitations. SWE measured by satellite remote sensing is hindered by the spatial resolution. AMSR-E is the best spatial resolution at 25 km (Gao et al., 2010). The value retrieved at this spatial resolution is not meaningful in complex terrain. To fill in the spatial gaps between ground-based measurements researchers interpolate. Interpolation can only represent the measured variability. SNOTEL sites are located where snow persists to maximize the period of data acquisition. A SNOTEL station on a north facing slope may not be a good indicator of the snow on the adjacent south facing slope. In an interpolation scheme this is a problem that can lead to significant errors in spatial representation. In a hierarchal linear spatial mixing model Kasurak et al. (2011) found only about 50% of the spatial variability of snow depth, and consequently SWE, was explained. This was found using two years of SWE measurements and a total of 215 sites and 3924 measurements. The spatial variability of SWE makes any acquisition of this data difficult. My work uses SCA because it captures the spatial variability and extracts a far more important characteristic of the snow: a repeatable pattern.

The use of SCA from remote sensing has proved valuable in models such as the snowmelt runoff model (SRM) developed by Martinec & Rango (1986). Martinec (1982) stated simply snowmelt runoff is a function of SCA and melt rate, which highlights the importance of this data. SCA data from remote sensing describes snow extent and many sensors collect this data on a daily time-step. The Moderate Resolution Imaging Spectroradiometer (MODIS) is a sensor which records daily SCA worldwide at a spatial resolution of 500 meters. This temporal resolution is ideal for monitoring snow extent because snow changes rapidly during the melting season. Other sensors, such as Landsat, may have a finer spatial resolution (60 meters), but images are only captured once every 16 days. To get a clear picture of snow melt through remote sensing the temporal and spatial resolution are equally important. Even though the spatial resolution of MODIS is a compromise, we can gain significant information about snow in complex terrain because daily images are recorded. MODIS has setbacks and this will be discussed in depth.

The year-to-year variability of snow makes modeling snowmelt runoff difficult. The monitoring methods discussed above all can help to clarify the drivers of snowmelt. The more we know about snowmelt now the better we can manage and prepare for a changing climate. Climate simulations highlight the difficulty of snowmelt runoff modeling. Many simulations state there is higher confidence in modeling snow accumulation than snowmelt (Poulin et al., 2011; Thrasher et al., 2012; Poyck et al., 2011). Many reasons for this difficulty exist, but one step we can take towards addressing this is finding repeatable spatial information about snow. A variable that does not change would help stabilize the otherwise highly variable system. My proposed work identifies and tests a repeatable spatial variable that has the potential to change the way we approach snowmelt runoff modeling.

Remote Sensing of Snow Setbacks: Cloud Removal

There are two MODIS sensors onboard the Terra and Aqua satellites. They have daily worldwide coverage from 2000 to present, and both collect snow covered area data. The more recently available Visible Infrared Imaging Radiometer Suite (VIIRS) sensor produces the same snow cover dataset as MODIS at a finer 375-meter spatial resolution. The VIIRS data is available from 2012 to present. We use MODIS because it has a longer data record. Snow cover is calculated by the Normalized Difference Snow Index (NDSI). NDSI combines bands four and six from the MODIS sensor to detect snow (wavelengths of 0.545-0.565 and 1.628-1.652 μm respectively). Band four is within the visible wavelengths and cloud cover disrupts the collection of snow extent and location. The NDSI calculation is necessary to decipher the difference between cloud and snow. On clear

(cloud free) days, the MODIS sensor has a spatial accuracy of 93% (Hall & Riggs 2007). Cloud cover is detrimental to this data because it reduces the amount of usable data. Many methods have been developed to remove cloud cover, and they can be separated into three categories: temporal, spatial, and spatio-temporal interpolations. The spatio-temporal methods are often complex multi-step methods.

Temporal interpolation, sometimes referred to as temporal filtering, has reduced cloud cover in many studies. These methods use time as the basis for interpolation. The simplest temporal interpolation combines the imagery from the Terra and Aqua satellites, which have different overpass times. Combining these two images has achieved a cloud cover reduction of 39.9% over Europe (Dietz et al., 2012). A more complex method uses a temporal window (range of days prior to and after the day of a cloudy image) to remove cloud cover. Parajka & Blöschl (2008) pioneered this approach and reduced the average cloud cover over Austria from 63% to 4% using a window of 7 days prior to the cloudy image date. These methods are effective at removing cloud cover, but they assume pixels do not change from snow to land during the temporal window. This may only be applicable in regions where minor change occurs for the snowpack; however, where spatial changes occur rapidly this assumption is problematic.

Spatial interpolation relies on visible pixels and their proximity to interpolate cloud covered pixels. Gafurov & Bardossy (2009) used visible nearby pixels within a single image to interpolate cloud covered pixels. Another method, which has been widely used, is the regional snow line elevation (RSLE) developed by Parajka et al. (2010). The elevation of a pixel is used to interpolate its cloud removed pixel value. Elevations of the visible, or non-cloud covered, pixels are used to define three elevation zones. In one zone all cloud covered pixels are assigned as snow, in another snow-free, and in the final zone partially snow covered. The partially snow-covered zone is most likely the region of active snowmelt and contains the snow-land interface. This partially covered zone records the lowest certainty (Krajki et al., 2014; Parajka et al., 2012). This zone may be the most critical area to correctly represent snow location for snowmelt runoff modeling.

Spatio-temporal methods are often multi-step methods for cloud removal. The MODSNOW-tool developed by Gafurov et al. (2016) removes daily cloud cover with spatial accuracy ranging from 77.3-99.8% with the lowest accuracy recorded during the melting period. The MODSNOW-tool can remove cloud cover on days where cloud coverage is 100%. The Adaptive Weighted Spatio-Temporal Model (AWSTM) also removes 100% cloud cover using a multi-step approach, including a 5-day temporal window, with accuracies of 93.11-98.92% (Li et al., 2017). The AWSTM accuracy

was calculated for a watershed which only records a maximum of 25% SCA. Recalculation of this error based only on the snow-covered portion of the watershed reduces the accuracy. Dong & Menzel (2016) improved on the MODSNOW-tool to decrease misclassification errors and found accuracies of 87-92%. They used ground-based stations to calculate their accuracy instead of the MODIS imagery. Li et al., (2017) noted that using the in-situ measurements for accuracy assessment is unreasonable because there is a spatial resolution mismatch of 4 square meters (SNOTEL measurement) to 250,000 square meters (MODIS pixel). The innovative methods use the conditional probability of snow cover to remove cloud cover. The probability of a pixel being snow covered is calculated based on the average time period in which each pixel is covered and/or the snow coverage of other pixels or ground-based stations. Probabilities functions capture averages well but do not describe the extremes. In snowmelt runoff modeling extremes are the most important to accurately represent i.e., droughts and floods.

Effectively these spatio-temporal methods produce cloud free imagery retrospectively at their stated accuracies. For monitoring long term snow cover, this is ideal. The complex process of snowmelt can be monitored by remote sensing; however, cloud cover is detrimental to the raw data and the assumptions necessary to remove it make this data set unappealing in extreme snow years and for real-time water management. We gain only retrospective insight into snowmelt without gaining any knowledge that can be applied to help us manage water today.

A new method pioneered by Woodruff and Qualls (2019) uses the recurrent pattern of SCA to remove cloud cover. This idea has been noted in the literature for many years and over many locations (Adams, 1976; König & Sturm, 1998; Luce & Tarboton, 2004; Sturm & Wagner, 2010; Parr et al., 2020). Patterns were even note by Wang & Xie (2009) when developing a cloud removal method over the Tianshan Mountains on the Tibetan Plateau. The repeatability is derived from multiple years does can be applied to any melt period. Unlike the temporal conditional probability, the method derived by Woodruff & Qualls (2019) uses only the spatial information allowing for the shift in melt timing. This ability to shift in time is essential for modeling extreme snow years. A cloudy day is made clear by identifying when in the melting process the watershed is based on the visible pixels. Each daily image cloud removal is an independent measurement from the previous or subsequent days. The method is operational on a daily time-step with minimal processing.

Applications of Remote Sensing in Snowmelt Runoff Modeling

The repeatable pattern of SCA has numerous applications. The pattern is independent of year-to-year snow variability and provides a usable dataset for snowmelt runoff modeling. We first must

discuss where SCA is already applied in snowmelt runoff modeling, where and why it is not applied elsewhere, and finally the potential impact of my proposed work.

Remotely sensed SCA is a valuable input to the Snowmelt Runoff Model (SRM) Martinec & Rango (1986). Snow depletion curves, which describe the increment of spatial change in snow cover for an increment change in time over a given area, are found using SCA data from remote sensing. The watershed is divided into elevation bands and a depletion curve is derived for each band to describe how SCA changes with time. Often, only days with less than 10% cloud cover are used to develop the depletion curves and the rest of the days are filled in using cloud removal interpolations (Steele et al., 2017). MODIS has been used as input for SRM and has demonstrated increased accuracy of snowmelt runoff modeling over ungauged watersheds (Qiu et al., 2014; Safari Shad et al., 2014; Steele et al., 2017).

Many research groups have adapted SRM to incorporate physical characteristics of the watershed to better represent the landscape. One research group added slope and aspect to SRM and found an increase in the runoff coefficient of determination from 0.73, 0.69, and 0.79 to 0.76, 0.76, and 0.81 for three respective years over a mountainous watershed in the Urumqi River Basin in Northern China (Abudu et al., 2016). Nagler et al. (2007) used the SRM model and a data assimilation approach to produce short term runoff predictions for the years 2005 and 2006 over the Austrian Alps. They found a coefficient of determination of 0.88 for every forecasting step for the snowmelt runoff modeling portion of the exercise. SRM accuracy is increased when spatial characteristics such as slope and aspect are incorporated and has demonstrated the ability to forecast snowmelt runoff.

The SRM model makes use of SCA, but it is rarely used as a consistent input in other models. Cloud cover, misclassification of pixels, and the difficulty of snow detection under vegetation are cited as reasons to exclude remotely sensed SCA from models (Andreadis & Lettenmaier, 2005). The Variable Infiltration Capacity (VIC) model is a widely used physically based and fully spatially distributed model developed by Cherkauer & Lettenmaier (2003). There has been resistance to incorporating remotely sensed SCA into the VIC model. Andreadis & Lettenmaier (2005) found when they compared MODIS with ground-based data, the two data sources only agreed between 75.2 and 84.8% of the time over the entire Snake Basin. Based on this result, they indicated VIC more accurately represented SCA than MODIS when compared to the ground-based stations. Two issues are present in their findings. One, the spatial disparity between a SNOTEL station and a MODIS pixel introduces a large amount of uncertainty in snow representation. Two, they fit the VIC model over a

20-year period to the same SNOTEL sites that were used to verify accuracy. If we are to calibrate models with ground-based data and use the disagreement of remote sensing as a reason to not use remote sensing, we should also calibrate to remote sensing data. As demonstrated with SRM, spatial information has the potential to increase accuracy.

Remotely sensed SCA has existed as a source of data that many models do not incorporate. Snow location is vital information in SRM as well as physically based models like VIC. Schlogl et al., (2018) found the advection from snow free surfaces adjacent to snow increased ablation by rates of 25-30% in the Dischma valley in the Swiss Alps. Without accurate representation of snow location this melting process may be underrepresented in physically based models.

Derivation of the Spatio-Temporal Recurrent Pattern of Snowmelt

The work in presented in this dissertation builds off the work by Woodruff & Qualls (2019). An overview of their methods is presented. The spatio-temporal recurrent pattern of snowmelt can be extracted with multiple years of remote sensing and a statistical combination of the data known as a Principal Component Analysis (PCA). We use the MODIS daily snow cover data which is contaminated by cloud cover. If cloud cover were not present, the repeatable pattern could be found using a single year. Using multiple years allows us to discard the contamination of cloud and find the true repeatable pattern. This model derivation can be split into two steps: data preparation and application of a PCA.

In the data preparation step, we condense the immense amount of imagery into two images per year. These images describe the melt timing of each pixel. Condensing this down allow us to utilize all the available imagery with the redundance removed. For example, if we are using 17 years to develop our PCA model we would take all the available imagery for each year and condense that information down into two images per year. Effectively we describe melt with 34 images instead of 6205 images (365 per year). For a given year, we iterate through all the available imagery and record two days of year (DOY) for each pixel. For a given pixel we record the DOY it was last recorded as snow (LDS image) and the first DOY it is recorded as land (FDL image). If cloud did not exist, the difference between the FDL and LDS would be 1 day. Because cloud exists the difference between these images is often greater than 1 day. These images are equal in size and geolocation to the original MODIS imagery. The MODIS product gives a range of NDSI snow cover values. The LDS and FDL both are a function of what we consider to be snow free. Woodruff & Qualls (2019) selected a cutoff of 40 where values below 40 are considered snow free.

Once the LDS and FDL are found for each year, we place the information into a matrix. One matrix contains the FDL values and one the LDS. The matrix is shown in *equation 1.1*, where **D** is a place holder for either FDL or LDS. The matrix is of size *N* by *M*. The number of columns (*M*) is equivalent to the number of years. The length of *N* is equivalent to the number of pixels in the watershed. All the values in row N_i are for the same pixel. The matrix is therefore organized by pixel and year. Two additional columns exist containing each pixel's centroid x and y coordinates; however, this is excluded from the PCA. To calculate the PCA model we can use either the LDS matrix or the FDL matrix.

Equation 1.1

$$*D* = \begin{bmatrix} 1,1 & \cdots & 1,M \\ \vdots & \ddots & \vdots \\ N,1 & \cdots & N,M \end{bmatrix}$$

The output of a principal component analysis is Eigen vectors and Eigen values. There are *M* Eigen vectors and *M* Eigen values equivalent to the *M* columns in the **D** matrix. Eigen Vectors, often referred to as principal components (PC), are calculated for the **D** matrix and each one describes a portion of the total dataset variance. Cumulatively, the total dataset variance is described by all the Eigen Vectors. An important definition of Eigen Vectors is each one is orthogonal and independent from all others. PC1, the first Eigen vector, describes the most variance of the dataset, PC2 the second most, and PC(*M*) the least. Where PC(*M*) is the last PC of a *N* by *M* matrix. We found PC1 captures the recurrent pattern of snowmelt and nearly all (>80%) of the total variance. In comparison, PC2 describes less than 3%. Mathematically this means the values of all the pixels in a single year vary more than a single pixel does across multiple years. The variance of this data is contained in the repeatable pattern not in the year-to-year variability.

To find the model of the recurrent pattern of melt, we multiply the input matrix (**D**) by the Eigen Vector or PC1. The result is a vector of length *N*. We attach the vector to the x, y coordinates. The values of the vector can then be re-projected into a raster (grid of values), equal in size and location to the MODIS daily data. This is the final PCA model. A mathematical representation of the transformation is shown in *equation 1.2*. The contents of the final PCA model describe each pixel's *relative* melt timing. *Relative* means the pixel's value represents when it melts in relationship to all other pixels in the watershed.

Equation 1.2

$$\begin{bmatrix} 1,1 & \cdots & 1,M \\ \vdots & \ddots & \vdots \\ N,1 & \cdots & N,M \end{bmatrix} * \begin{bmatrix} 1 \\ \vdots \\ M \end{bmatrix} = \begin{bmatrix} 1 \\ \vdots \\ N \end{bmatrix}$$

The PCA model is continuous but can be changed to a binary snow or no snow image by selecting a threshold value which we refer to as *t**. The *t** value splits the unique pixel values of the model into either snow free (less than the threshold) or snow (greater than the threshold). The values contained in the PCA model describe each pixel's *relative timing of melt*. The unique values are ordered from first to last to melt.

The existence of cloud cover between the LDS and FDL introduces potential uncertainty to the melt pattern. PCA is often difficult to interpret because the output is not always related specifically to *one* physical process. In remote sensing, metrics such as the Tasseled Cap Analysis have been developed to deal with the interpretability of PCA. The Tasseled Cap Analysis is a standardized transformation of the data (Jensen, 2016). Woodruff & Qualls (2019) provided a comparison of the PCA model developed using the FDL and the PCA model developed using the LDS and found the two models were 99.8% correlated. The difference between the LDS and FDL is cloud persistence or uncertainty. The correlation of the resulting PCA demonstrates that the pattern found is nearly equal. The influence of cloud is therefor discarded in the remaining principal components. While the cloud influence has been discarded, we might wonder if individual years are more heavily weighted in the first principal component. Woodruff & Qualls (2019) demonstrated the weights in the first principal component are all nearly equal at between 0.194 to 0.310. They also calculated the factor loadings for the FDL versus the resulting principal component for the first two principal components. Factor loadings for the first principal component ranged from 0.88 to 0.94 or highly correlated while the second principal component, which only described 2% of the total variance, ranged from -0.33 to 0.27. The recurrent pattern is the signal we want to use which is captured in the first principal component.

References

Abudu, S., Sheng, Z.-P., Cui, C.-L., Saydi, M., Sabzi, H.-Z., & King, J. P. (2016). Integration of aspect and slope in snowmelt runoff modeling in a mountain watershed. Water Science and Engineering, 9(4), 265–273. https://doi.org/10.1016/j.wse.2016.07.002

Adams, W. P. (1976). Areal differentiation of snow cover in east central Ontario, Water Resources Research, 12(6), 1226– 1234, doi:10.1029/WR012i006p01226.

Andreadis, K. M., & Lettenmaier, D. P. (2006). Assimilating remotely sensed snow observations into a macroscale hydrology model. Advances In Water Resources, 29(6), 872–886. https://doi.org/10.1016/j.advwatres.2005.08.004

Balk, B., & Elder, K. (2000). Combining binary decision tree and geostatistical methods to estimate snow distribution in a mountain watershed. Water Resources Research, 36(1), 13–26.

Barnett, T.P., Adams, J.C., & Lettenmaier, D.P. (2005). Potential impacts of a warming climate on water availability in snow-dominated regions. Nature, 438, 303–309.

Cherkauer, K. A., & Lettenmaier, D. P. (2003). Simulation of spatial variability in snow and frozen soil. Journal of Geophysical Research: Atmospheres, 108(D22).

Dickerson-Lange, S.E. & Mitchell, R., (2014). Modeling the effects of climate change projections on streamflow in the Nooksack River basin, Northwest Washington. Hydrological Processes, 28(20), pp.5236–5250.

Dietz, A., Wohner, C., & Kuenzer, C. (2012). European Snow Cover Characteristics between 2000 and 2011 Derived from Improved MODIS Daily Snow Cover Products. Remote Sensing, 4(8), 2432-2454. doi:10.3390/rs4082432.

Dong, C., & Menzel, L. (2016). Producing cloud-free MODIS snow cover products with conditional probability interpolation and meteorological data. Remote Sensing of Environment, 186, 439.

Gafurov, A., & Bárdossy, A. (2009). Cloud removal methodology from MODIS snow cover product. Hydrology and Earth System Sciences, 13(7), 1361-1373.

Gafurov, A., Lüdtke, S., Unger-Shayesteh, K., Vorogushyn, S., Schöne, T., Schmidt, S., Kalashnikova, O., & Merz, B. (2016). MODSNOW-Tool: An operational tool for daily snow cover monitoring using MODIS data. Environmental Earth Sciences, 75(14), 1-15. doi:10.1007/s12665-016-5869-x.

Gao, Y., Xie, H., Lu, N., Yao, T., & Liang, T. (2010). Toward advanced daily cloud-free snow cover and snow water equivalent products from Terra–Aqua MODIS and Aqua AMSR-E measurements. Journal of Hydrology, 385(1-4), 23–35. https://doi.org/10.1016/j.jhydrol.2010.01.022

Hall, D. K., & Riggs, G. A. (2007). Accuracy assessment of the MODIS snow products. Hydrological Processes, 21(12), 1534-1547. doi:10.1002/hyp.6715.

Jensen, J. (2016). *Introductory Digital Image Processing: A Remote Sensing Perspective* (4th ed.).

Kasurak, A., Kelly, R., Brenning, A., & Pelto, Mauri S. (2011). Linear mixed modelling of snow distribution in the central Yukon. Hydrological Processes, 25(21), 3332–3346. https://doi.org/10.1002/hyp.8168

König, M. & Sturm, M. (1998). Mapping snow distribution in the Alaskan Arctic using aerial photography and topographic relationships, Water Resour. Res., 34(12), 3471–3483, doi:10.1029/98WR02514.

Krajčí, P., Holko, L., Perdigão, R. A. P., & Parajka, J. (2014). Estimation of regional snowline elevation (RSLE) from MODIS images for seasonally snow covered mountain basins. Journal of Hydrology, 519(PB), 1769-1778. doi:10.1016/j.jhydrol.2014.08.064.

Li, X., Fu, W., Shen, H., Huang, C., & Zhang, L. (2017). Monitoring snow cover variability (2000–2014) in the Hengduan Mountains based on cloud-removed MODIS products with an adaptive spatio-temporal weighted method. Journal of Hydrology, 551, 314-327. doi:10.1016/j.jhydrol.2017.05.049.

Luce, C. H., & Tarboton, D. G. (2004). The application of depletion curves for parameterization of subgrid variability of snow. Hydrological Processes, 18(8), 1409-1422. doi:10.1002/hyp.1420.

Martinec, J. (1982). Runoff Modeling from Snow Covered Area. Geoscience and Remote Sensing, IEEE Transactions on, GE-20(3), 259-262. doi: 10.1109/TGRS.1982.350440

Martinec J. & Rango, A. (1986). Parameter values for snowmelt runoff modelling. Journal of Hydrology, 84(3), pp.197–219.

Maurer, E., Hidalgo, H. G., Das, T., Dettinger, M. D., & Cayan, D. R. (2010). The utility of daily large-scale climate data in the assessment of climate change impacts on daily streamflow in

California. *Hydrology and Earth System Sciences*, *14*(6), 1125–1138. https://doi.org/10.5194/hess-14-1125-2010

Nagler, T., Rott, H., Malcher, P., & Müller, F. (2008). Assimilation of meteorological and remote sensing data for snowmelt runoff forecasting. Remote Sensing of Environment, 112(4), 1408–1420. https://doi.org/10.1016/j.rse.2007.07.006

Parajka, J., & Blöschl, G. (2008). Spatio-temporal combination of MODIS images – potential for snow cover mapping. Water Resources Research, 44(3), N/a. doi:10.1029/2007WR006204.

Parajka, J., Pepe, M., Rampini, A., Rossi, S., & Blöschl, G. (2010). A regional snow-line method for estimating snow cover from MODIS during cloud cover. Journal of Hydrology, 381(3), 203-212. doi:10.1016/j.jhydrol.2009.11.042.

Parajka, J., & Bloschl, G. (2012). MODIS-based snow cover products. validation and hydrologic applications. In: Chang, Y., Ni-Bin, H. (Eds.), Multiscale Hydrologic Remote Sensing Perspectives and Applications. Springer, 185–212.

Parr, C., Sturm, M., & Larsen, C. (2020). Snowdrift landscape patterns: An Arctic investigation. Water Resources Research, 56, e2020WR027823. https://doi.org/10.1029/2020WR027823

Poulin, A., Brissette, F., Leconte, R., Arsenault, R., & Malo, J.-S. (2011). Uncertainty of hydrological modelling in climate change impact studies in a Canadian, snow-dominated river basin. *Journal of Hydrology (Amsterdam)*, *409*(3), 626–636. https://doi.org/10.1016/j.jhydrol.2011.08.057

Poyck, S., Hendrikx, J., McMillan, H., Hreinsson, E. O., & Woods, R. (2011). Combined snow and streamflow modelling to estimate impacts of climate change on water resources in the Clutha River, New Zealand. *Journal of Hydrology, New Zealand*, *50*(2), 293–311.

Qiu, L., You, J., Qiao, F., & Peng, D. (2014). Simulation of snowmelt runoff in ungauged basins based on MODIS: A case study in the Lhasa River basin. Stochastic Environmental Research and Risk Assessment, 28(6), 1577–1585. https://doi.org/10.1007/s00477-013-0837-4

Safari Shad, M., Habibnejad Roshan, M., & Ildoromi, A. (2014). Integration of the MODIS snow cover produced into snowmelt runoff modeling. Journal of the Indian Society of Remote Sensing, 42(1), 107–117. https://doi.org/10.1007/s12524-013-0279-y

Schlogl, S., Lehning, M., Fierz, C., & Mott, R. (2018). Representation of Horizontal Transport Processes in Snowmelt Modeling by Applying a Footprint Approach. Frontiers in Earth Science, 6, Frontiers in Earth Science, Oct 8, 2018. doi: 10.3389/feart.2018.00120.

Steele, C., Dialesandro, J., James, D., Elias, E., Rango, A., & Bleiweiss, M. (2017). Evaluating MODIS snow products for modelling snowmelt runoff: Case study of the Rio Grande headwaters. International Journal of Applied Earth Observations and Geoinformation, 63, 234–243. https://doi.org/10.1016/j.jag.2017.08.007

Sturm, M., & Wagner, A. (2010). Using repeated patterns in snow distribution modeling: An Arctic example. Water Resources Research, 46(12), N/a. doi:10.1029/2010WR009434.

Thrasher, B., Maurer, E. P., McKellar, C., & Duffy, P. B. (2012). Technical Note: Bias correcting climate model simulated daily temperature extremes with quantile mapping. *Hydrology and Earth System Sciences*, *16*(9), 3309–3314. https://doi.org/10.5194/hess-16-3309-2012

Wang, X., & Xie, H. (2009). New methods for studying the spatiotemporal variation of snow cover based on combination products of MODIS Terra and Aqua. Journal of Hydrology, 371(1), 192-200. doi:10.1016/j.jhydrol.2009.03.028.

Woodruff, C. D., & Qualls, R. J. (2019). Recurrent snowmelt pattern synthesis using principal component analysis of multiyear remotely sensed snow cover. Water Resources Research, 55. https://doi.org/10.1029/2018WR024546

Chapter 2: Time Repeatability of the Spatio-Temporal Recurrent Pattern of Snowmelt Over the Upper Snake River Basin

Introduction

Snow is a vital source of the world's freshwater supply. It has been estimated that 50% of the world's potable supply and 75% Western United States' supply comes from snowmelt (Barnett et al., 2005; Balk & Elder, 2000). With a changing climate the already variable timing of maximum instream flow rates is projected to move earlier (Barnett et al., 2005). Water management relies on correctly simulating snowmelt runoff timing. Preparing for floods, droughts, and the impacts of climate change are all benefitted through identifying the drivers of snowmelt. Modeling efforts have developed over the years, but two widely used methods identify a divide in what data is used.

Currently, spatially distributed models are regarded as the most accurate method to simulate snowmelt. Many models use point-based ground measurements as data input to simulate snowmelt runoff in retrospect, real-time, and climate scenarios. The Variable Infiltration Capacity (VIC) model is one such model, which is a widely used spatially distributed energy balance approach to modeling snowmelt. Cherkauer & Lettenmaier (2003) adapted the VIC model to add in a distributed snow algorithm. Spatial grids of snow cover were produced from point measurements of snow, and the distributed grid is then melted by the energy budget. In their adaptation Cherkauer & Lettenmaier (2003) found the modeled snow showed divergence from the snow observations. The observed snow depth was found to be larger than the simulated depth during the melting period. This corresponded with overestimation of temperature. They also found flow estimation accuracy was increased when the model was calibrated.

An alternative approach in snowmelt runoff modeling is to use remote sensing rather than point based measurements. The Snowmelt Runoff Model (SRM) uses remotely sensed snow-covered area (SCA) as a model input Martinec & Rango (1986). SRM employs a temperature index approach which relies on snow location. Remotely sensed SCA often has missing data due to cloud coverage, so a set of snow depletion curves (SDC) are developed to mitigate this issue and model SCA with time. The watershed is divided into elevation bands and each band has its own SDC. This approach simulates runoff as a function of snow location and melt rate (Martinec, 1982).

Both methods, VIC and SRM, require spatial data whether it is a direct measurement or an interpolated grid. The ideal variable for modeling snowmelt is spatially distributed snow water equivalent (SWE) at a fine spatial resolution. Ground based point measurements of SWE are available

through a network of SNOw TELemetry (SNOTEL) sites. SWE can also be obtained through remote sensing. Techniques for retrieving SWE from remote sensing include gravity-based methods (GRACE satellite), gamma radiation retrieved through low flying aircraft, passive microwave (AMSR-E), and combinations of active (QuickSCAT) and passive microwave (Tedesco et al., 2015). These methods range in spatial resolution (25m-10s of km) and in temporal resolution (infrequent by aircraft to daily). The higher resolution methods have infrequent collection making continuous monitoring difficult. The high spatial variability of SWE over complex terrain limits the ability of any of these data sources to provide spatially gridded SWE. (Dingman, 2008). In a hierarchal linear spatial mixing model Kasurak et al. (2011) found only about 50% of the spatial variability of snow depth, and consequently SWE, was explained. This study used two years of SWE measurements collected at 215 sites, for a total of 3924 measurements. This large measurement and modeling exercise by Kasurak et al. (2011) communicates the difficulty spatial modeling and interpolation of SWE presents. Remote sensing of SWE offers spatially distributed data but suffers significant interpretation issues. The large spatial resolution of 25 kilometers is far too great for representing complex terrain (Gao et al., 2010). For example, a watershed with complex topography may have no snow at the valley floor and significant snow depth at elevation, but the large spatial resolution of remotely sensed SWE would assign a single value. This value is not representative of the snow distribution. Worldwide remotely sensed SWE at fine spatial and temporal resolutions presently has significant limitations especially for mountainous terrain. Considering this, there are strong advantages to using remotely sensed SCA.

Remotely sensed SCA is available daily at spatial resolutions between 375 and 500 meters. Over the years SCA records have been collected at increasingly finer spatial resolutions. The Advanced Very High-Resolution Radiometer (AVHRR) recorded SCA at a spatial resolution of 1.1 kilometer at nadir beginning in the 1970's (Jensen, 2016). At the 500-meter spatial resolution, imagery from the Moderate Resolution Imaging Spectroradiometer (MODIS) sensor flown aboard the Terra and Aqua satellites have been available since 2000 and 2002, respectively (Hall & Riggs, 2015). Most recently the Visible Infrared Imaging Radiometer Suite (VIIRS) instrument has collected SCA at 375-meter spatial resolution beginning in 2012 (Riggs et al., 2019). Snow is detected using the Normalized Difference Snow Index (NDSI) algorithm. The NDSI combines a portion of the visible and mid infrared wavelengths. Since visible wavelengths are used, cloud obstruction poses a significant challenge for snow observation. Terra's MODIS sensor has shown 93% agreement with ground-based observations under clear sky conditions (Hall & Riggs, 2007). Other factors impact the MODIS NDSI detection algorithm such as scan angle, topography, illumination, and vegetation

(Riggs et al., 2017). Cloud cover presents the most consistent and detrimental loss of data for these sensors.

Extensive research has gone into development of methods to remove clouds from SCA imagery. Methods developed include temporal interpolation, spatial interpolation, and a combination of the two referred to as spatio-temporal interpolation. Temporal interpolation uses imagery collected at separate times. Terra and Aqua fly over a given location at separate times. Parajka & Blöschl (2008) and Dietz et al., (2012) combined the imagery from the two satellite overpass times to remove cloud cover. Parajka & Blöschl (2008) further reduced cloud obstruction to 4% over Austria by extending the temporal interpolation window to include images observed within the 7-day period preceding the cloudy day.

Spatial interpolation uses the proximity of cloud free pixels to remove cloud cover. Garfurov & Bardossy (2009) implemented a cloud removal protocol to use adjacent cloud free pixels to assign values to cloud covered pixels. The Regional Snow Line Elevation (RSLE) procedure developed by Parajka et al. (2010) uses elevation bands to remove cloud cover. The RSLE splits a watershed into three zones: snow, partial snow cover, and snow free. The two elevation lines demarcating the three zones are determined by the elevation of the lowest observed snow pixel and the highest snow-free pixel. A cloud obscured pixel is assigned a value in accordance with the elevation band it lies within.

Spatio-temporal methods combine both interpolation methods in multiple steps to remove cloud cover. Gafurov et al. (2016) developed the MODSNOW-tool to infill all the cloud covered pixels in an image with a multi-step approach, which can salvage even 100% cloud covered images. A conditional probability of snow cover has been used in many of the spatio-temporal methods with exceptional results (Gafurov et al., 2016; Li et al., 2017; Dong & Menzel 2016). These complex methods all produce cloud free images even for images with 100% cloud cover; however, all suffer their lowest spatial accuracies of snow location during melt period.

The scientific value and demand for cloud free imagery has led to the publication of multiple cloud free datasets (Mauti et al., 2019; Tran et al., 2019). NASA's daily cloud-free MODIS dataset is produced by infilling each cloud covered pixel with its value the last time it was visible (Hall et al., 2019). The day each pixel's cloud free value was observed is also documented. This infill method induces a time-lag in the appearance of snow-free conditions for many pixels and reduces real-time accuracy. Published cloud free data are extremely useful for retrospective analysis of snow cover, but water managers need greater accuracy for real-time analysis.

A SDC represents a time series of spatially aggregated SCA for a watershed or elevation zone within a basin, reported as a percent of watershed or zone area. An advantage of a SDC is that it simplifies temporal interpolation since this only requires propagating a single curve forward in time, without concern for specific details of which pixels are changing; it infills missing pixels in aggregate incurring a loss of spatial information. The sacrifice is made to achieve a complete time series (Nagler et al., 2006). Routine availability of remotely sensed SCA images in near-real time would maintain the spatial nature of the data and allow a major shift in the way we model snowmelt runoff. The interannually recurring pattern of snowmelt may provide the key to integrating the spatial information of remote sensing and the temporal information of an SDC, without a tradeoff. Patterns in snow covered area have been noted in the literature for many years (Adams, 1976; König & Sturm, 1998; Luce & Tarboton, 2004; Sturm & Wagner, 2010; Wang & Xei, 2009). Capitalizing on these observations, Woodruff & Qualls (2019) developed a spatial model of the recurrent pattern of SCA depletion using a multi-year remote sensing approach. This model could open the door to a spatial model with a temporal application.

Our hypothesis is that in addition to a spatially recurrent pattern, a recurring temporal trend exists that allows linking the spatial and temporal patterns together. The temporal trend can be synthesized into a dimensionless time series of SCA. In this paper we use the Principal Component Analysis (PCA) spatial model developed by Woodruff & Qualls (2019) to develop and analyze a dimensionless SDC, which we term the "PCA SDC". We also propose a linear representation of snow depletion. Both methods are a direct output from the spatial SCA model. Our method provides a spatial representation of SCA at every time step because we use a dedicated spatial model and a related SDC. The linear relationship simplifies the complexity of normalizing snowmelt timing and allows simple adjustments for secondary snowfall. We approach the problem of spatially describing melt in time from the perspective of space driving time.

The spatial pattern can be used to describe and scale any melt period. If we can normalize the time component of SCA depletion with a single curve or a line, meaning it represents an interannually recurring temporal pattern, then forecasting of SCA depletion may be achievable. Real-time and climate simulations of snowmelt runoff both could benefit from this information because the spatial pattern is unchanging. The way in which snowmelt runoff modeling is approached, and the usefulness of remote sensing could potentially change if space offers a repeatable relationship with time.

Study Area and Data

Study Area

The Upper Snake Basin located in Wyoming, United States, serves as an important source of usable freshwater for downstream users. The watershed (Figure 2.1) drains an area of 8,894 square kilometers with elevation ranging from 1,737 to 4,194 meters. The climactic regime is consistent with that of the inland northwest, where in-stream flows are dependent on snowmelt. The snowmelt from this study area provides freshwater for many downstream uses including agriculture, municipal uses, and in-stream fish requirements. Snow seasonally covers the watershed. Snow coverage ranges from 100 to 0% percent in most years. The enormous size, importance of water to downstream users, and annual snow coverage makes this watershed ideal for remote sensing applications. Land cover, as calculated by the National Land Cover Database (Homer et al., 2015), ranges from sagebrush steppe (45.4% coverage by area) to evergreen and mixed forest (47.9% total forest coverage).

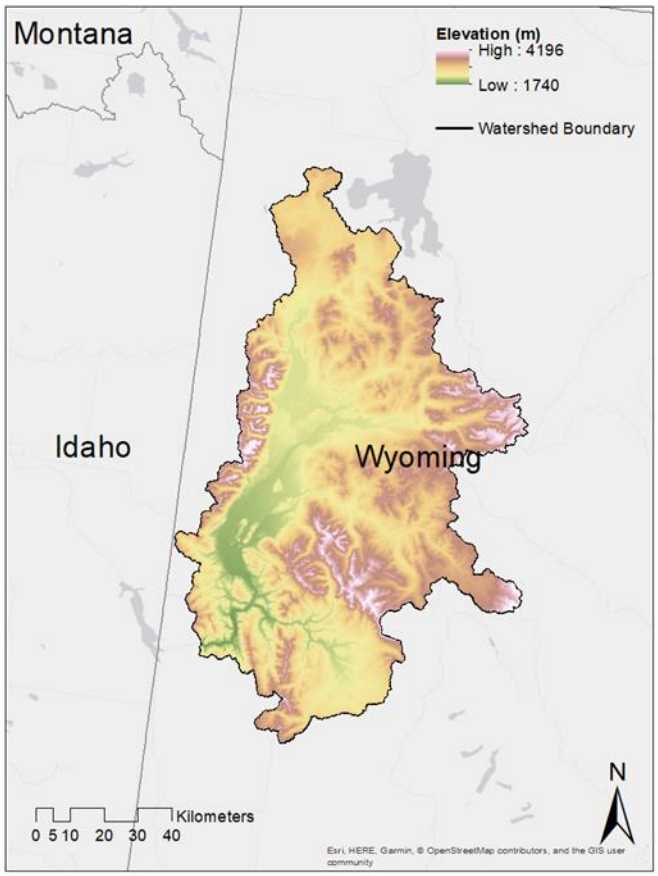

Figure 2.1: Location and topography of the Upper Snake Basin Study Site.

Data Sources

The SCA data was acquired from the National Snow and Ice Data Center (NSIDC). The MODIS daily imagery from the Terra satellite which has a morning equatorial pass over time was downloaded for the years 2000 – 2017. The Aqua satellite MODIS sensor had a failure in band 6, which is used in the NDSI calculation for snow detection. The NDSI calculation has been restored for the Aqua satellite by substituting in band 7 into the calculation, but the data product often produces more snow commission errors than the Terra satellite MODIS sensor (Hall et al., 2019). Therefore, we have excluded the Aqua data from our research. Two tiles h09v04 and h10v04 were necessary to capture the full watershed extent. The version 6 MODIS data product includes several data layers including a NDSI snow cover, QA/QC layer, NDSI basic, albedo and others. NDSI snow cover data was used in this analysis.

SNOw TELemetery (SNOTEL) sites were minimally used in the study. The watershed contains eleven of these ground-based sites, which record SWE. One site (Base Camp) was used to calculate a starting day of year, a step in the PCA spatial model. See Woodruff & Qualls (2019) for an in-depth discussion.

Methods

The overall purpose of this article is to assess the repeatability of the time component of a spatial pattern of snow-covered area. To analyze this, we present the following steps. First, we use the PCA spatial model to remove cloud cover from daily MODIS imagery. The PCA SDC curve is developed by transforming the PCA spatial model. Next, a metric of cloud removal confidence is derived to identify high confidence cloud removed images. With these established, the PCA SDC is fit to the cloud removed data by fitting the curve in time with a single year. We then account for secondary snowfall by shifting the PCA values plotted against time. This approach allows us to implement a simple linear regression rather than dealing with the more complex PCA SDC. The data is shifted one day at a time until a maximum R-squared value is recorded. We also calculate the AIC for model fits before and after shifting. Finally, we normalize all the cloud free data with the PCA SDC values. The normalized data is plotted together to analyze temporal repeatability.

The PCA Spatial Model

The PCA spatial model presented in Figure 2.2 was developed and discussed in depth in Woodruff & Qualls (2019). For clarity we present a brief description here. The PCA model is a static image of the study watershed in which the pixel values represent the relative melt timing of pixels throughout a melt season. Selection of a threshold melt timing value bifurcates the PCA image into a

snow-covered region whose pixel values exceed the threshold, and a snow-free area whose pixel values are smaller than the threshold. The snowline lying along the interface of the two regions corresponds to the selected threshold, as illustrated by the red, blue, and green example snowlines in Figure 2.2.

The spatial model was created using daily imagery over the study site from 17 years. The daily imagery is condensed into two images per year. The two condensed images record the last day snow is seen (one image) and the first day land is seen (one image) for each pixel. PCA is applied to one of the sets of images (last day of snow or first day of land) from all the years. The first principal component results are plotted with x, y coordinate information to create the spatial PCA model. Woodruff & Qualls (2019) argue the PCA extracts 92% of the recurrent pattern of snowmelt while also discarding any cloud contamination.

Once the PCA spatial model is generated, we can use it to remove daily cloud cover, producing cloud-free images. Cloud cover is removed through a simple fitting procedure in which the PCA threshold value is identified that minimizes the Visible Pixel Error (*VPE* in equation 2.1). To calculate the *VPE*, a trial threshold value is selected to convert the continuous PCA spatial model into a binary snow/no-snow representation. The *VPE* for the trial threshold is then calculated by comparing the visible pixels of the cloudy image with the corresponding pixels of the binary PCA model. In equation 2.1, I_L and I_S are the number of pixels where the model and the image disagree, where the subscripts refer to the pixels wrongly represented by the model as snow or land, and T_P is the total number of visible pixels in the cloudy image.

Equation 2.1

$$VPE = \sqrt{\frac{{I_L}^2 + {I_S}^2}{{T_P}^2}}$$

A range of trial thresholds are evaluated and the value which minimizes *VPE* is selected to generate the cloud-free image for that day. If only snow or land pixels are visible in an image, this algorithm identifies the snowline as corresponding to the lowest or highest threshold value associated with the visible area, respectively. This represents the upper/lower limit of the snowline for the two respective cases rather than the actual location of the snowline. Daily MODIS imagery was downloaded, and cloud cover was removed for 2001-2017 using equation 2.1.

For every cloud removed image another metric was recorded to quantify daily cloud removal confidence. Cloud removal confidence is related to the length (I_i) of snow/land interface visible in the

ith cloud-obscured image compared to the corresponding length (M_i) of the interface in the cloud-free PCA spatial model image. An interface exists if a pixel is adjacent to a pixel of a different value, e.g., snow adjacent to land. Adjacency is defined using a queen's case neighborhood (Brunsdon & Comber, 2019). I_i and M_i are calculated by summing the number of interfaces in their respective images for a given day. The ratio of these two, the visible interface fraction (V_i, Eqn. 2.2), quantifies the fraction of the modeled snowline that was visible in the cloud-obscured image.

Equation 2.2

$$V_i = \frac{I_i}{M_i}$$

Two considerations exist for the visible interface calculation. The first is that an edge effect exists. Secondly, if only one pixel type is visible the V_i calculation may be falsely high. Given a day where only snow or only land is visible, we calculate I_i and M_i based on the watershed perimeter. Without this perimeter-based approach the I_i and M_i values would be zero at the beginning and end of the melt period, even if the entire watershed is visible. This results in an issue during the melt period where only one pixel type is visible. Given the case where only snow is visible during the middle of the melt period, the V_i is calculated based on the perimeter which may result in a large V_i. This large V_i indicates a high confidence in cloud removal even though this is extremely unlikely. We are certain the SCA is not as large as what was selected by the PCA model. During the middle of the melting period, a falsely high confidence value occurs for cloud removal results of either 100% snow or 100% land coverage. We handle this false high issue by excluding these images from our analysis according to a rule. The rule is cloud removal values are excluded if the previous and subsequent days are within 80-20% SCA.

PCA Snow Depletion Curve

The PCA spatial model can be converted to a temporal PCA SDC. The temporal component is normalized by equation 2.3. Where N_t is the normalized time, P_t is a given PCA model pixel value at time t, and P is simply a PCA model pixel value. This normalization creates a pseudo time component ranging from 0 to 1. SCA depletion in the SDC is represented by the conversion of pixels from snow to land. At a given N_t, there exist several pixels greater than the value of P_t. This quantity of pixels can be described as a percentage of the total pixels in the watershed, and this percentage represents the SCA at time N_t.

Equation 2.3

$$N_t = \frac{P_t - MIN(P)}{MAX(P) - MIN(P)}$$

We can then scale N_t values to fit any given year by altering two parameters. This scalable aspect can transform the normalized SDC to represent SCA in time. The parameters and formulation are shown in equation 2.4. The slope, or duration of melt (D_m), and the initiation of melt (I_m) are altered to transform the SDC. The normalized N_t is scaled by these parameters to represent the DOY an SCA is measured (T_{SCA}). It is important to note, each T_{SCA} has a distinct, fixed SCA related to it within a given year. Therefore, we alter the timing of the melt period to fit the measured timing of SCA depletion in a given year.

Equation 2.4

$$T_{SCA} = N_t * D_m + I_m$$

Accuracy Assessment

We numerically solve for the best fit of D_m and I_m for a given year, which minimizes the sum of squared error given by Eqn. 2.5. The error for each point is calculated by the difference SCA_t - SCA_a, where SCA_t is the SCA at time T_{SCA} and SCA_a is the actual measured SCA at time t derived from remote sensing. Accuracy of the PCA SDC is quantified using the root mean squared error (RMSE).

Equation 2.5

$$SSE = \sum_{i=1}^{t} (SCA_t - SCA_a)^2$$

Secondary Snowfall

PCA is a linear transformation of a higher dimension dataset into a lower dimension. This characteristic of PCA linearizes the average of the 17 years used to develop the model. A given year (PCA values) when plotted with time that follows a linear trajectory would suggest that the PCA not only on average is linear but in individuals years is linear. PCA produces a linear transformation independent of whether each individual year is linear with time. We would expect the average to be linear. A year may not be linear with time if melt began rapidly and slowed as the season progressed. A combination of many of these years would still produce a linear output, but individual years would systematically deviate from the line. We will first establish whether individual years are linear with time.

With an individual year linear relationship established, a secondary snowfall event still presents a problem. If secondary snowfall events disrupt the timing of the progression of melt this can be identified by a step change in the linearity of the snowmelt season. We normalize the time component of the snowmelt season to a scale of 0 to 1. The beginning of melt, or zero, is determined as the first day of the melt period that the PCA values are continuously greater than 400, and the end is set as the first day a value of 750 is recorded. This normalization and range allow us to focus our analysis on the melting period. We fit a linear regression to the PCA values versus time and calculate the R-squared as well as the AIC.

Our hypothesis is that a secondary snowfall event postpones melt, as reflected by a lateral translation of the PCA t^* melt curve, but when melt resumes it continues along the same linear trajectory as before the secondary snowfall event. To test this hypothesis, we first use observations from the eleven ground-based SNOTEL stations within the watershed to identify the occurrence of secondary snowfall events. We define a secondary snowfall event as any increase in SWE at a SNOTEL station which occurs after the date of maximum SWE. Of the 17 years of data used in this analysis we identified and recorded secondary snowfall events in every year. We also recorded the date ranges for any delay in timing of melt from the PCA values. If these two time periods, secondary snowfall from SNOTEL and delays in PCA values versus time, coincide then we shift the data. Adjusting a single year is done by simply shifting the day of year associated with the PCA values forward one day at a time and fitting a new linear regression model for each shift. Only data after a verified secondary snowfall event was shifted. The R-squared value is calculated for each model and the optimal number of days to shift the data was selected by the largest R-squared. We then calculate the AIC for the linear regression fit to the optimal shifted data for comparison with the original un-shifted data.

Normalization of Snow Seasons

The final component of the analysis is the normalization of all the melt periods. We normalize each cloud removed SCA measurement for a given year according to the fitted parameters (D_m and I_m). Equation 2.6 describes how this is accomplished for a single image. In equation 2.6, N_i is the normalized time of an image, and T_{SCA} is the DOY associated with SCA value of the cloud removed image. This transformation assigns a normalized (0 to 1) value to each cloud removed image, which allows us to plot all cloud removed data points on a single plot.

Equation 2.6

$$N_i = \frac{T_{SCA} - I_m}{D_m}$$

Results

The results are presented in the following order. The PCA spatial model and PCA SDC are presented first, followed by the visible interface cloud removal confidence metric and optimization of this value. We then fit the PCA SDC to the daily cloud removed data. The systematic deviation analysis follows, and finally the culmination of this work is presented. The year-to-year temporal repeatability of snow depletion is shown.

PCA Spatial Model and Depletion Curve

The spatial PCA model describes the repeatable pattern of SCA depletion across multiple years and is a demonstrated cloud removal method (Woodruff & Qualls, 2019). Figure 2.2 is the PCA spatial model. Pixel values in the spatial PCA model represent the *relative timing* of melt of each pixel in relation to all other pixels in the watershed. In figure 2.2 the lower values (darker areas) melt earlier, and higher values (lighter areas) melt later.

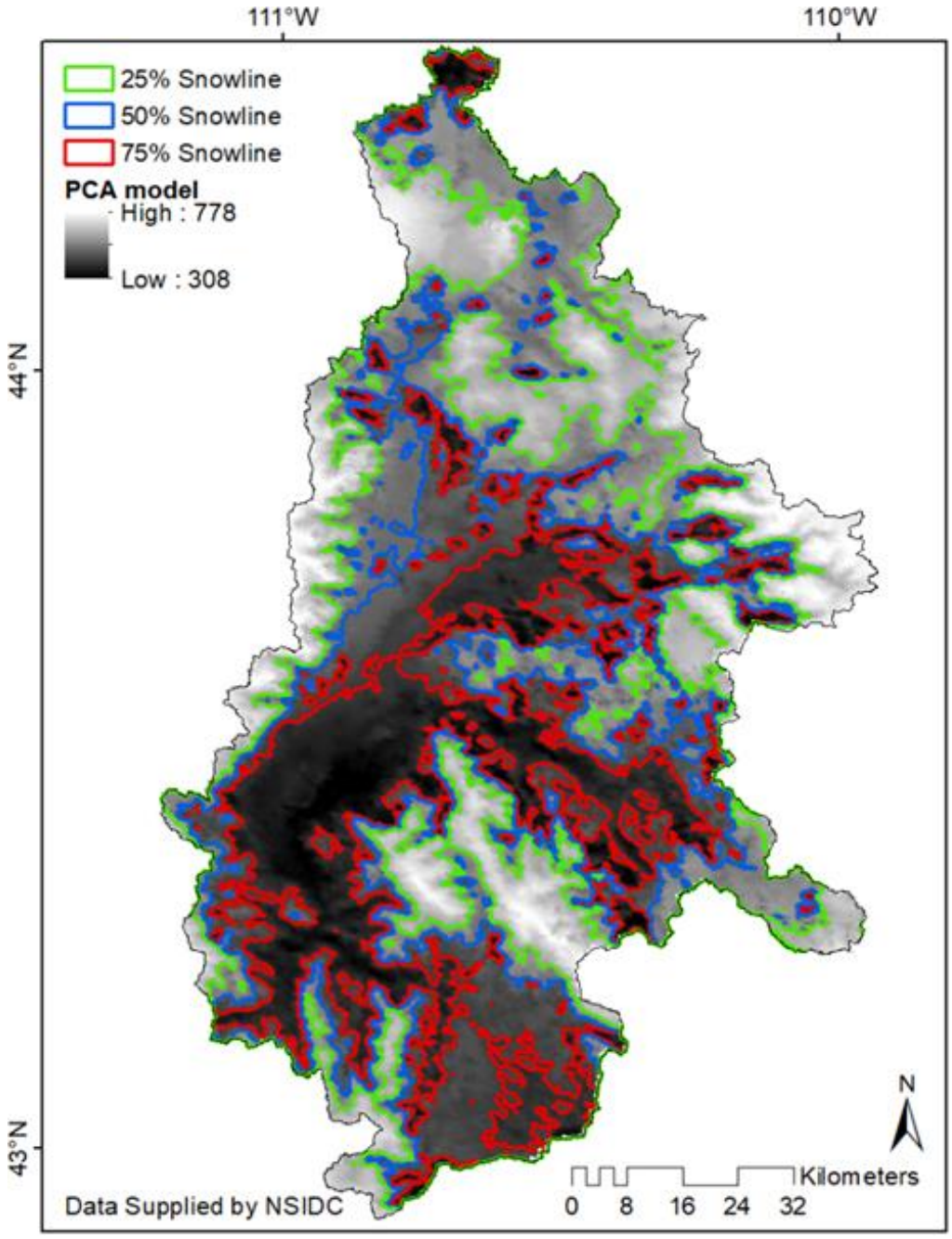

Figure 2.2: PCA spatial model where each pixel value represents the relative melt timing. Darker (lower) pixel values melt earlier, and lighter (higher) values melt later. Three snow-land interface lines are shown in red, blue, and green to depict the snow coverage at 75, 50, and 25% SCA, respectively.

The PCA SDC, shown as the non-linear solid black curve in Figure 2.3 is the transformed PCA spatial model. At a given N_t, shown on the x axis, there is a distinct corresponding SCA value. The red, blue, and green circles along the curve represent values of corresponding 75, 50, and 25%

SCA snowlines in Figure 2.2. All the area contained within a given snowline in Figure 2.2 would be deemed as snow free and all the area between the watershed boundary and the snowline would be snow covered. The relationship between these two figures is the advantage of this method for representing SCA depletion with time. Unlike any other depletion curve, the spatial data is easily represented using the PCA SDC (Figure 2.3). Also shown in Figure 2.3 is the PCA values (range of 308-778) normalized to a 0-1 scale along the secondary y-axis. The relationship between N_t and normalized PCA values is linear shown as the dashed black line. The corresponding 75, 50, and 25% SCA points are shown as squares along the line and the colored arrows indicate the relationship between the PCA SDC and the linear PCA values. The non-linear description of snow depletion given by the PCA SDC can also be described linearly if we use the PCA values rather than SCA to describe snowmelt. As discussed in the methods PCA is a linear transformation of higher dimension data into lower dimensions. It captures the non-linear description of the *relative timing of melt* and describes it linearly. We present the PCA SDC because it is a familiar curve, but the linear description is a novel and powerful approach to analyzing the temporal repeatability of snowmelt.

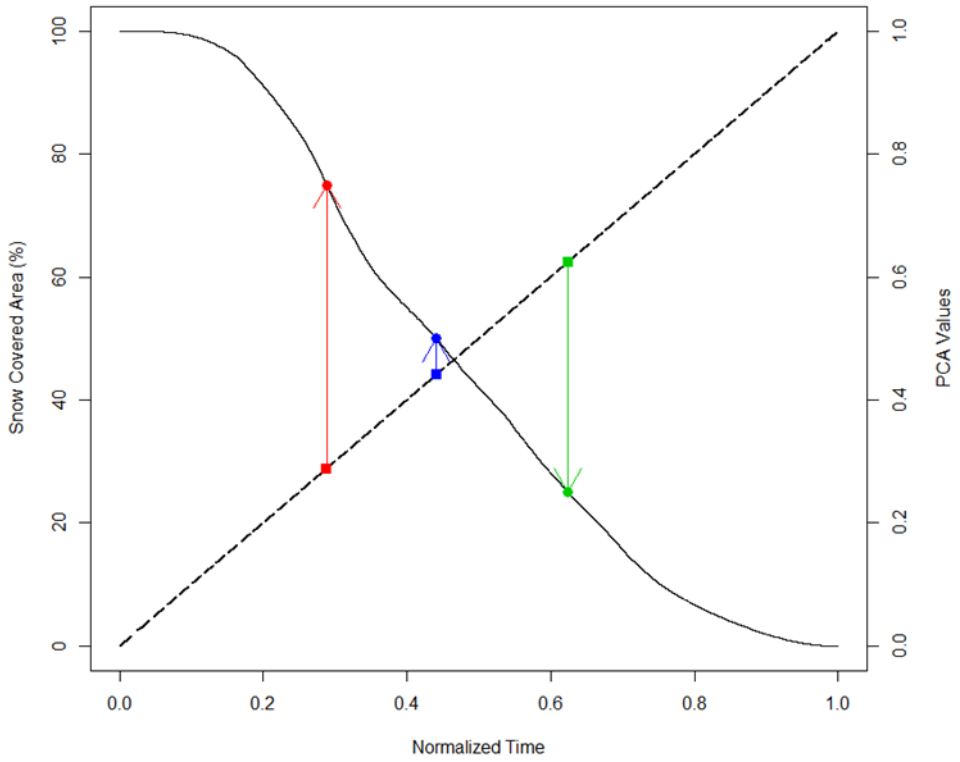

Figure 2.3: Normalized PCA SDC. The curve describes how SCA percentage changes with normalized time (N_t). Three points along the curve identify SCA values of 75, 50, and 25% corresponding to like-colored spatial snowlines shown in Figure 2.2. Normalized PCA values are plotted along the secondary y-axis against normalized time. Colored arrows indicate the relationship between SCA and PCA values along a normalized time axis.

Cloud Removal and Deriving Confidence Metrics

Cloud removal was completed for all the available daily imagery from 2001-2017 excluding the days with 100% cloud cover. The visible interface fraction (equation 2.2) is calculated for each cloud removed image. The cloud removal process does not use information from prior or subsequent days. The cloud removal only makes use of the visible pixels in a single image; therefore, the daily cloud removal is independent data. Independent measurements are necessary for the creation and fitting of the PCA SDC. If temporal interpolation of any kind were used during the cloud removal process model inbreeding would exist.

For each cloud removed image we record the *VPE* (equation 2.1) as well as the V_i (equation 2.2). The *Vi* metric was designed to put higher confidence in imagery where a greater fraction of the interface between snow and land is visible. The V_i helps to avoid- over and underestimation of snow cover, especially in cases where only one pixel type is visible, such as at the beginning and end of the

melt period. If only one pixel type is visible, the *VPE* does not offer any information. A large V_i puts high confidence in images where cloud cover may be significant, but the length of interface is also large. An important consideration in developing this metric is defining the lower limit of the V_i value which represent high cloud removal confidence.

We optimized the V_i lower limit by fitting the PCA SDC to cloud removed imagery and calculating the Sum of Squares Error (SSE). The parameters I_m and D_m (eqn. 2.4) were calculated for V_i values ranging from 0-0.1 with a step of 0.01 for each year. To select the optimal V_i value, we analyzed the product of the change in number of images retained and the change in SSE calculated for a given V_i. This multiplication produces a local maximum at the V_i where error is lowest, and the number of images retained is highest. Figure 2.4 plots the results of this analysis for 2009. The black line represents the product of the step changes in the SSE and the number of images retained at each V_i. The increase of V_i from 0 to 0.01 is the largest, which is driven by the high error rate and substantial change in images retained. We do not select this maximum because the error is still large. The black line has a local maximum of 6.10 at a V_i of 0.05. The red line shows the decline in images retained ranging from 237 to 136. The number of images retained declines at a relatively stable slope after a sharp decline between the V_i range of 0 and 0.02. The steady slope in the number of images retained communicates the error SSE dropped significantly at a V_i of 0.05. A similar local maximum was found for each year. The optimal value of V_i selected by each year varied between 0.02 to 0.08 with only four of the years selecting a V_i. of greater than 0.05. An average of the selected V_i is 0.046, which we round up to 0.05. This value was used for the remaining analyses.

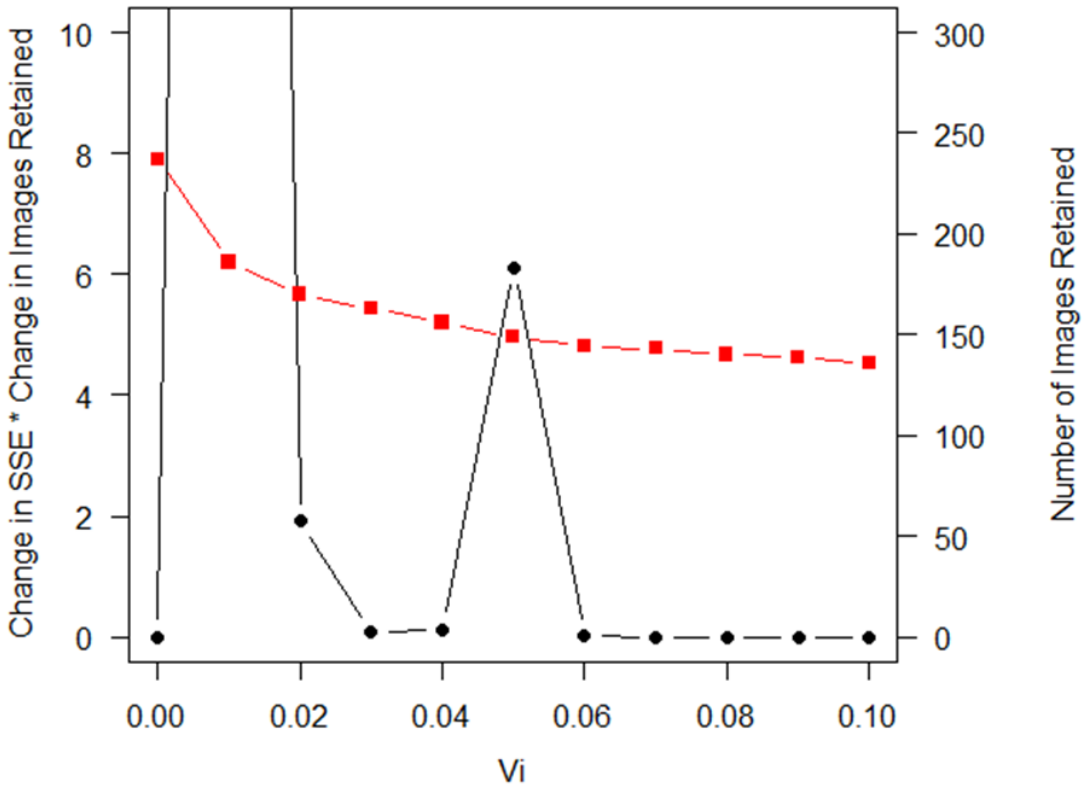

Figure 2.4: Optimization of V_i for 2009. V_i is shown along the x-axis. The product of the step change for a give V_i in the SSE and the number of images retained is plotted along the primary y-axis (black with circles). Shown in red with squares is the count of images retained plotted with respect to the secondary y-axis.

A comparison of the number of available images using a cloud coverage cutoff and the V_i 5% cutoff are shown in Table 2.1. Across all the years, daily available images range between 226 and 246. Discarding all the imagery with greater than 10% cloud coverage leaves 42 to 64 images. Applying our V_i 5% threshold a significant increase is seen with 134 to 160 images available.

Table 2.1: The comparison of availability of images from MODIS for each year is shown. The total number of images available starting at January 1 of each year is shown; followed by the count of images with <10% cloud coverage, and the number of images available using the visible interface of 5%.

Year	*Available Images*	*Images with < 10 % Cloud Coverage*	*Images with > 5 % Visible Interface*
2001	226	57	**146**
2002	235	46	**151**
2003	237	55	**143**
2004	239	51	**151**
2005	243	63	**156**
2006	244	55	**160**
2007	245	63	**157**
2008	239	56	**154**
2009	237	43	**148**
2010	246	47	**134**
2011	243	42	**138**
2012	241	64	**153**
2013	244	59	**158**
2014	238	57	**139**
2015	244	57	**152**
2016	223	52	**156**
2017	236	64	**146**

Fitting the SDC Curve

The PCA SDC is fit to the daily cloud removed data with greater than 5% visible interface. The curve is fit by optimizing the sum of squares error (equation 2.5). Two parameters are optimized to fit the curve. The PCA SDC fit for 2006 is shown in Figure 2.5. Initially, we can note the PCA SDC (black line) has a varied slope throughout the melt period that accurately tracks the daily cloud removed data From Table 2.2, discussed below, the RMSE for the PCA SDC is 0.018. The cloud removed data suggests there was early melt around DOY 75 that is not described by the curve. Based on the prior and subsequent days, it is clear to see that if this melt was occurring it was not the main trajectory of melt. We may attribute this to errors in the data, although even if it is correct this potential error is acceptable because it is a false start to the melt period. The PCA SDC accurately describes the beginning of melt following the decline in SCA extremely well. The non-linear PCA SDC accurately describes melt with time. This plot demonstrates for 2006 that the recurrent pattern which captures average behavior also describes time repeatability in individual years.

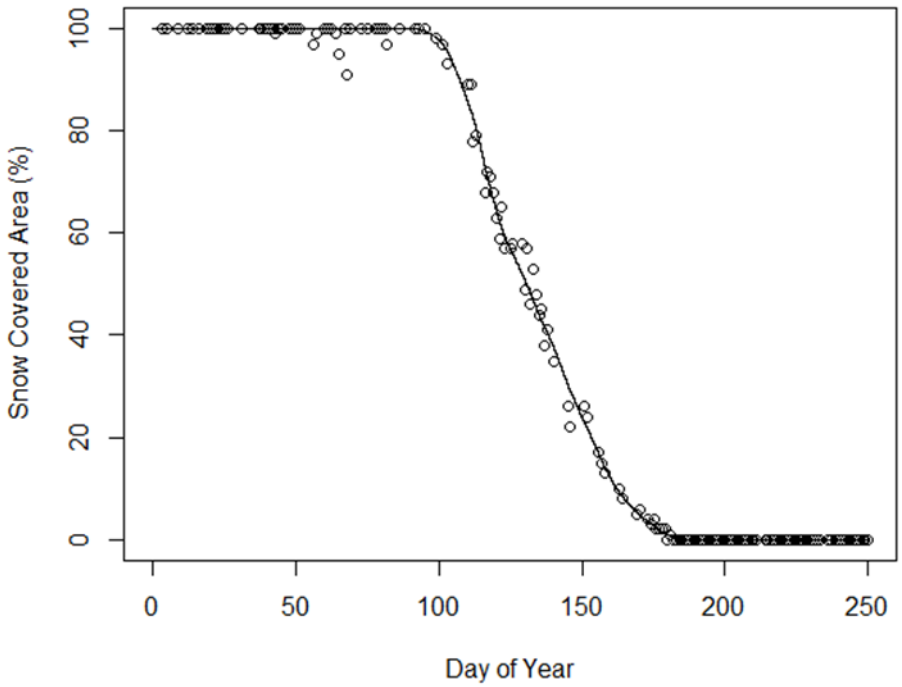

Figure 2.5: PCA SDC curve (black line) and daily cloud removed data with V_i values of > 5% (black points) are plotted for the melt period of 2006. The SCA percentage is plotted against day of year.

The RMSE is calculated to determine the accuracy of the PCA SDC fit for each year. The number of images varies each year because we use the 5% visible interface condition as seen in Table 2.1. The RMSE standardizes the error. Error for the PCA SDC for all 17 years is shown in Table 2.2. The PCA SDC accurately follows the progression of melt for all 17 years. The average RMSE is 0.030 and the maximum and minimum values of 0.043 and 0.017 were recorded. The maximum RMSE was recorded in 2010 and the minimum in 2008. Discussed later the variation in RMSE may be due to secondary snowfall events; however, the fit is exceptional in all 17 years which includes 2017, an independent year.

Table 2.2: Fitted parameters of I_m and D_m are shown for each melt period as well as the RMSE using the PCA SDC.

Year	*Melt Initiation in Days (I_m)*	*Melt Duration in Days (D_m)*	*PCA SDC RMSE*
2001	85.6	76.7	0.036
2002	75.2	118.1	0.025
2003	67.8	128.4	0.034
2004	52.2	146.9	0.031
2005	66.7	130.7	0.034
2006	86.3	100.7	0.018
2007	56.4	125.1	0.036
2008	96.2	113.9	0.017
2009	87.7	109.0	0.022
2010	67.2	141.7	0.043
2011	108.1	112.8	0.022
2012	58.5	136.7	0.033
2013	87.2	90.6	0.036
2014	91.7	101.8	0.029
2015	57.6	127.2	0.032
2016	72.8	112.4	0.026
2017	79.7	129.4	0.032

Large variations in the PCA SDC fitted values (I_m and D_m) are shown in Table 2.2. The I_m varied from 52.2 to 108.1 in 2004 and 2011, respectively. This is a 56-day (nearly two month) difference in when melt began in those years. The D_m value recorded a range of 70.3 days, with shortest and longest melt durations of 76.7 days and 146.9 days for 2001 and 2004, respectively. The average I_m value was 76.3 and average D_m was 117.8. One might suggest this is due to more or less snow. This is not what we observed. For instance, the year 2004 was a low snowpack year; however, it recorded the longest duration. On the other hand, 2011 was the largest snowpack and recorded late snow accumulation. In 2011 there was a late initiation of melt (large I_m), but a short duration (D_m). Another large snowpack year, 2017, recorded above average initiation and duration. Variations in these fitted parameters describe the highly variable snow conditions in the study site.

Secondary Snowfall

In every year besides 2006, we recorded a delay in the timing of melt which was attributed to a secondary snowfall event. The impact of these events is illustrated in Figure 2.6. SNOTEL SWE

data for Two Oceans Plateau (solid line), Togwotee Pass (dot-dashed line), and Thumb Divide (dotted line) are all plotted against normalized time. We can see three distinct secondary snowfall events occurring at normalized time values of 0.4 (Thumb Divide), 0.55 (Togwotee Pass and Two Oceans Plateau), and 0.75 (Togwotee Pass and Two Oceans Plateau). The PCA t* Threshold Values (circles plotted on secondary y-axis) reflect the first two events. One can see a distinct change in the slope from point to point at normalized time values of 0.4-0.45 and 0.55 to 0.67. The final secondary snowfall event occurring at normalized time 0.75 may have had a slight effect on the slope of the PCA values, but it is hard to distinguish with the naked eye.

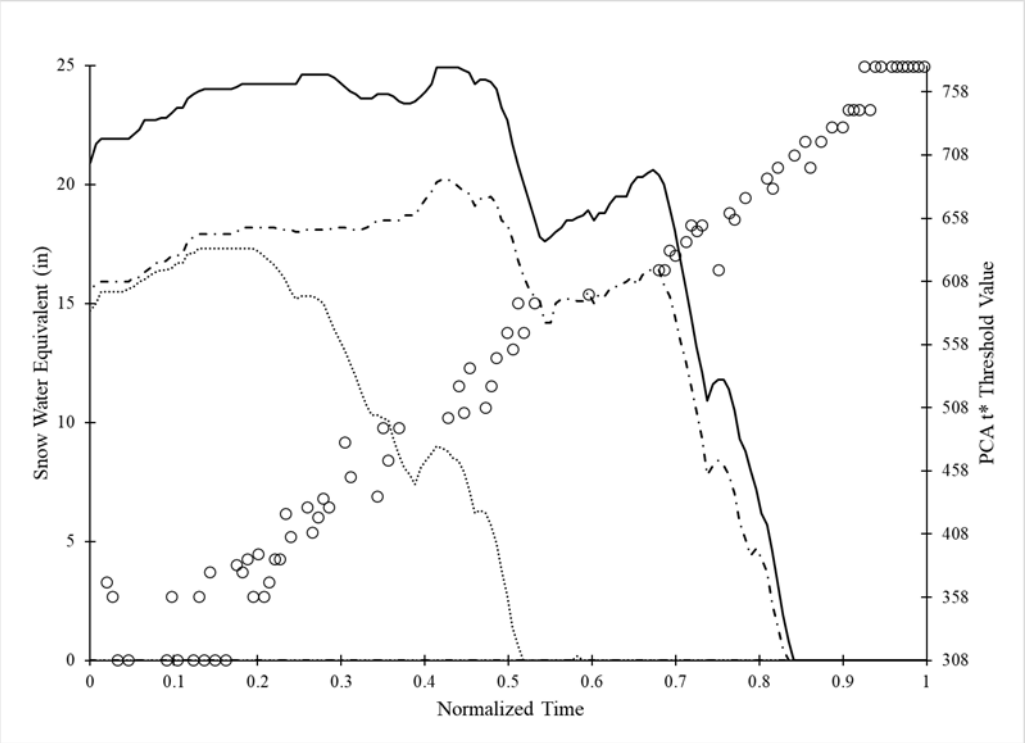

Figure 2.6: The 2004 melt period SNOTEL SWE for Two Oceans Plateau (solid line), Togwotee Pass (dot dash line), and Thumb Divide (dotted line) are plotted on the primary y-axis against normalized time. Also shown is the PCA t* Threshold Values on plotted on the secondary y-axis against normalized time.

We adjust the PCA t* Threshold Values for the secondary snowfall events to determine if these events had an impact on the progression of melt after the event occurred. To accomplish this, we fit a linear regression to the PCA t* Values versus DOY for each year. Adjusting a single year is done by simply shifting the day of year associated with the PCA t* Values forward one day at a time and fitting a new linear regression model for each shift. Only data that was recorded after the secondary snowfall event was shifted. The R-squared value is calculated for each model and the optimal number of days to shift the data was selected by the largest R-squared. We also employ the

Akaike Information Criterion (AIC) for shifted and un-shifted model fits. The AIC is used to determine model fit and a smaller value indicates a better fit based on the maximum log likelihood (Akaike, 1974). The optimal number of days selected to shift the data, the R-squared values, and the difference in AIC (shifted minus un-shifted) are given in Table 2.3.

The R-squared values calculated for the un-shifted data are exceptional with an average of 0.977, a maximum of 0.992, and minimum of 0.946 (column 2). This demonstrates the individual year linear relationship with time. By adjusting the data for secondary snowfall, we found increases in the R-squared values for every year. We recorded an average R-squared of 0.983, a maximum of 0.996, and a minimum of 0.961 (column 3). We also see the AIC for the shifted data was lower than all the un-shifted models. AIC is generally used to compare models fit to the same data. We are fitting the same model structure to the data and a decrease in the AIC means the data is getting closer to perfectly linear. We see exceptional improvements by shifting the data in 2008, 2010, 2011 and 2014 which all recorded decreases in the AIC of greater than 20. Any decrease in AIC of 2 or more indicates a significantly better fit. All the shifted models recorded a decrease in AIC of more than two. Given these high R-squared values and the results of the AIC, the PCA t* Threshold Values do move linearly with time even if a secondary snowfall event occurs; however, adjusting for the secondary snowfall events shows improvement in all cases. The watershed characteristics captured by the recurrent pattern of melt allows us to linearize snowmelt timing, a powerful tool for water management.

Table 2.3: Optimal days selected to shift the data, R-squared values, and difference in AIC for 2001-2017 are shown. The optimal days of shift for 2007 and 2013 are given as the first shift/second shift to distinguish between the first secondary snowfall adjustment and the second.

Year	*Optimal Days Shifted*	*R-Squared Un-shifted*	*R-Squared Shifted*	*Difference in AIC (Shifted – Un-shifted)*
2001	16	0.946	0.961	-11.60
2002	10	0.976	0.983	-12.08
2003	9	0.973	0.980	-16.69
2004	9	0.978	0.982	-9.05
2005	9	0.979	0.985	-13.87
2006	No Shift	0.989	No Shift	N/A
2007	7/5	0.977	0.980	-5.99
2008	7	0.992	0.996	-29.37
2009	6	0.983	0.986	-7.25
2010	15	0.965	0.984	-24.82
2011	8	0.987	0.993	-28.50
2012	4	0.972	0.973	-2.14
2013	10/7	0.973	0.985	-19.25
2014	9	0.970	0.984	-27.00
2015	5	0.983	0.984	-2.27
2016	6	0.987	0.991	-12.73
2017	8	0.980	0.984	-13.55

In two of the years there were two secondary snowfall events large enough to impact the progression of melt. These years, 2007 and 2013, required two shifts. In many cases such as 2004, 2009, and 2014 there were two secondary snowfall events; however, shifting the later event increased the R-squared and no further steps were taken. In 2007 and 2013 shifting the later secondary snowfall event alone had a negative effect on the R-squared, therefore we applied a shift to the first secondary snowfall event. The R-squared was optimized excluding the data which occurred after the second snowfall event. After this fit was complete, a second shift was applied which included all the data. The process is depicted for 2007 in Figure 2.7. The blue circles are the original, unshifted data points. The red dotted line marks the starting date of the first shift, and the red diamonds are the shifted points (7 days). The second shift, marked by the black dashed line, is shown as the black triangles (5 days). With each shift we can note the points appear to follow a more linear progression. Shifting these data provides a description of the duration of melt as it would have occurred had there been no secondary snowfall, a normalization of melt. The shifts also demonstrate that in all seventeen years

the progression of melt is linear, and the presence of a secondary snowfall events acts as a piecewise shift in the data. This is demonstrated by the increase in R-squared and decrease in the AIC for all shifted data.

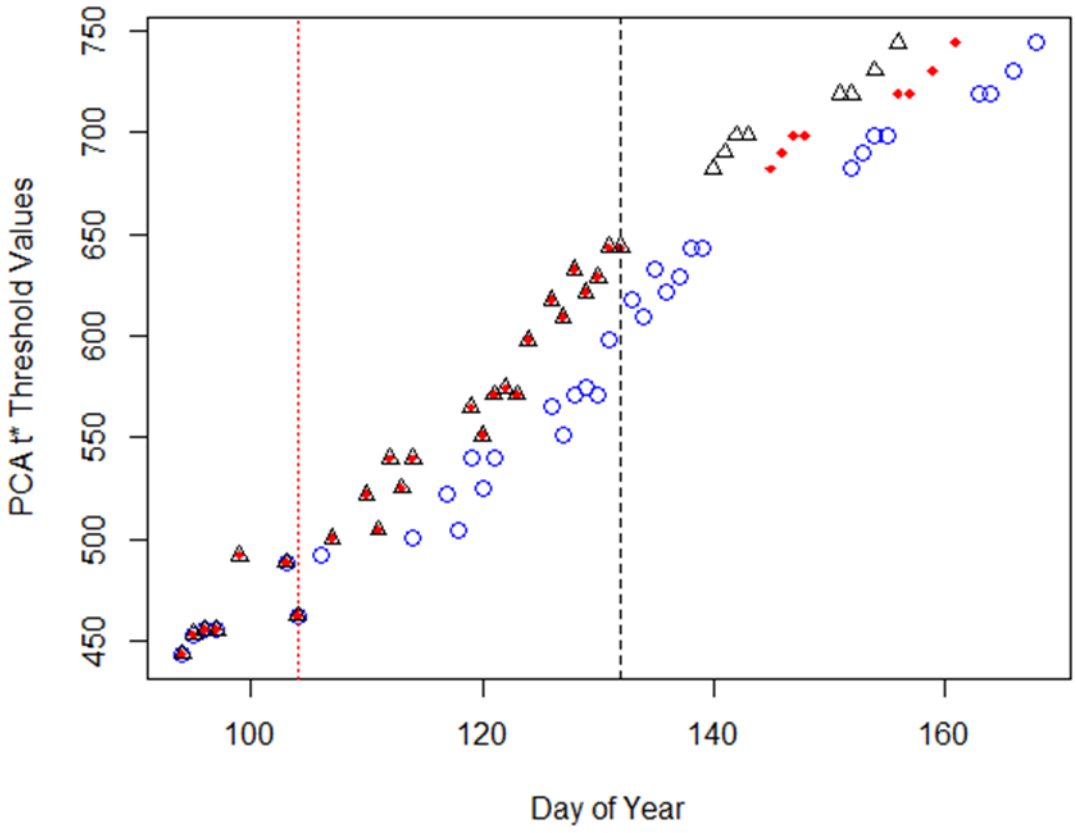

Figure 2.7: Shifted PCA t* Threshold Values are shown against the day of year for the melt period of 2007. The original un-shifted data is depicted as blue circles. The DOY of the first shift is identified by the red dotted line. Shifted data is given by the red diamonds (7 days). The start of the second shift marked by the black dashed line and is given by the black triangles (5 days).

Normalization of Melt Seasons

The PCA SDC accurately depicts each melt period individually. To verify whether the melt period follows the same curve year after year we can normalize all the cloud removed data on a single plot. We normalize all the cloud removed data used to fit the PCA SDC using equation 2.6. The DOY associated with an SCA measurement is scaled by the fitted parameters I_m and D_m. The DOY values

transformed into N_t values. Figure 2.8 shows all the normalized cloud removed data plotted together from all 17 years. The PCA SDC is plotted as the red line.

Across all 17 years, there appears to be higher variability during the beginning of the melt period compared to the end. This was noted in the systematic deviation analysis as well. The cloud removed data plot behaves similarly to an envelope, or a fuzzy line, about the PCA SDC. As the melt progresses, the envelope becomes tighter. Nearly all the points fall within a close perpendicular distance from the PCA SDC and are equally represented about the curve. From this comparison, we can see this normalization method accurately captures any melt period. If temporal repeatability did not exist, we would expect a far less organized plot. Much like the spatial repeatability of snow-covered area the time component can also be normalized simply and represented by a single curve.

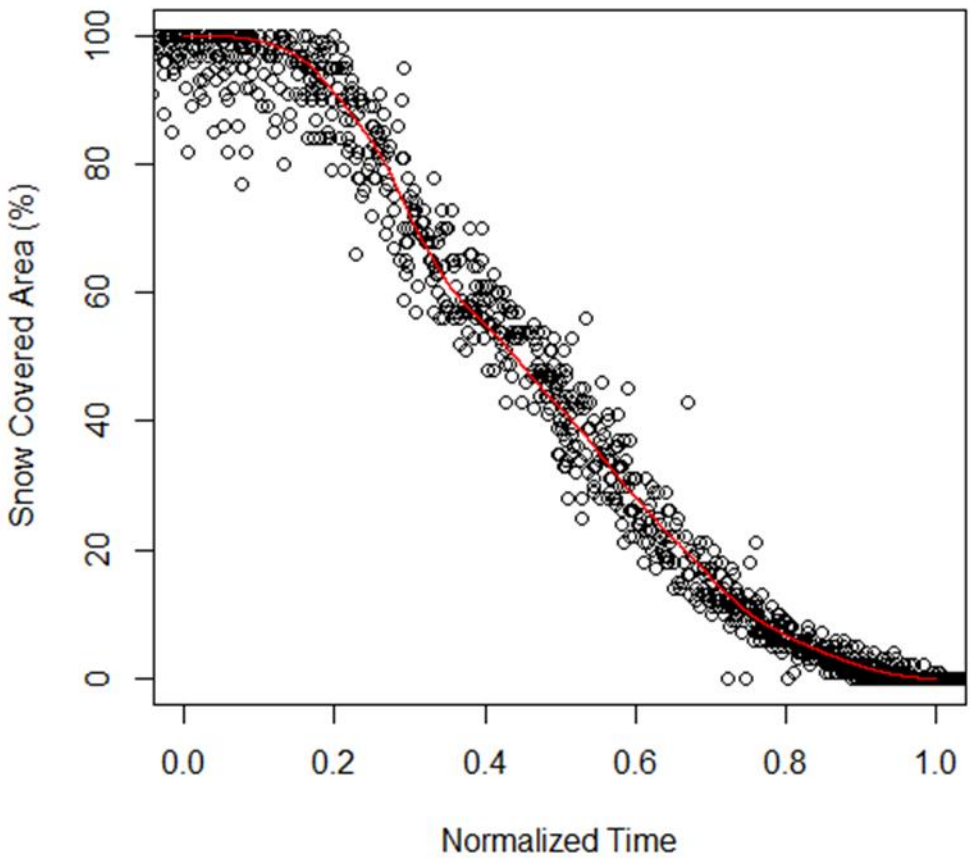

Figure 2.8: Normalization of melt initiation and duration for all 17 years on a single plot. Points refer to actual cloud removed measurements (with > 5% visible interface). The PCA SDC is shown in red.

Discussion

We have presented a simple two parameter transformation of a SDC to describe the melt period of 17 years. The idea of a depletion curve, and even a single curve to represent SCA depletion, is not new; however, a spatial model to a linear description of melt and a SDC relationship is novel. This spatial to temporal method for describing melt provides daily snow location data whether imagery is available or not. The implication of the temporal repeatability of any given melt period is a significant advancement. Snow melt is highly variable, and a difficult phenomenon to represent. Repeatable information may help understand and prepare for the water demands of a changing world.

As stated in the methods, the PCA is linear transformation of data. The importance of each individual year progressing linearly with time is a powerful statement. We addressed the impact

secondary snowfall events had on the linear progression, demonstrating each individual year is described well before and after secondary snowfall adjustment. If a year was not linear with time, we would expect to produce a different plot. If snowmelt began slow and sped up, we would expect the plot to follow a concave upward trajectory departing from the line early in melt and returning to it at the end. If the melt began quickly and slowed, we would expect a concave downward trajectory. The simple translation and stretching of the normalized time value produces a linear plot in every year. This suggests the spatial description of snow is intrinsically tied to the temporal trajectory and it is captured by the PCA model of the recurrent pattern of snowmelt.

An area of particular interest for the findings is retrospective snowmelt runoff modeling. Two impacts of the spatial model to SDC relationship are easily identified. First, temperature lapse rate can be more accurately represented with snow location data. Secondly, the advection of sensible heat from a warming land surface over snow adjacent to the snow to land interface can also be modeled with more certainty. Both areas of interest rely on daily cloud free imagery with temporal independence. While the SDC provides a temporal description the spatial PCA fluctuates daily with the snow coverage. Understanding the applications of our finding in retrospective analysis may help modeling in real-time.

Temperature lapse rate is an important variable in snowmelt runoff modeling. The widely used VIC model assumes a linear temperature lapse rate. Lower elevation temperature data are used to extrapolate temperature to higher elevations using a linear multiplier. An example of the importance of the temperature lapse rate is shown by Wang et al. (2016). They demonstrated near surface air temperature lapse rate influences streamflow, finding a 24% range in streamflow by calculating lapse rate under different assumptions. In their study, a linear lapse rate had the lowest yearly simulated discharge accuracy (Nash coefficient of 0.414), and the MODIS derived lapse rate had the highest (Nash coefficient of 0.696). The linear lapse rate assumption disregards the impact snow has on the surface temperature. This is physically wrong, because the surface of a melting snowpack is 0 degrees Celsius during the phase change from solid to liquid (Dingman, 2008). Temperature lapse rate has lacked a simple solution to a complex representation and has relied on the linear method due to its simplicity. Snow location has a substantial impact on surface temperature, and the PCA spatial model to PCA SDC provides this information.

The energy exchange at the snow to land interface also requires accurate snow location data. Advection from a snow free area adjacent to a snow-covered area has been demonstrated to increase the melt rate from 25-30% Schlogl et al. (2018). This enhanced energy exchange near the snow to

land interface not only increases the melt rate, but our results suggest the temporal progression of snowmelt is related to the spatial distribution of snow. This pattern may be influenced significantly by the snow to land interface. By misrepresenting snow location or simply modeling it, two extremely important variables could be influenced leading to significant accuracy reductions. This may be handled through calibration in average years; however, those are not the years that impact water management. Floods and droughts represent extremes, and calibrated models may not simulate these years well, whereas a physical spatial approach might.

The benefits of accurately representing snow location are known, but integration of remote sensing into models like VIC is not standard practice. Cloud removal has made snow cover data far more accessible for retrospective analysis; however, many times these cloud removal methods create highly temporally and/or spatially dependent data. The PCA spatial model to PCA SDC produces independent daily cloud removal data easily describing SCA with time. Another significant hurdle to overcome is MODIS data has often been deemed less reliable than the point-based SNOTEL data (Andreadis & Lettenmaeir, 2006). While this may or may not be true, a large advantage of remote sensing is overlooked. The spatial pattern, derived from remote sensing data, provides a standardized model for comparing the highly variable process of snowmelt.

This simple approach to representing snow depletion addresses a long-standing question about the repeatable pattern of snow melt, how do we use it? Modeling snowmelt ranges in complexity and at each level of model complexity the approach presented here is applicable. In the snowmelt runoff model (SRM) an issue with forecasting melt is the SDC is not known *a priori* (Martinec et al., 1983). We showed the SDC is a function of the recurrent spatial pattern and is scalable to any snow melt season. In complex models such as the VIC model, representation of snow-covered area could help model temperature lapse rate and sensible heat flux. The two components of our approach address both model issues by combining a simple spatial based approach with a time representation. The repeatability of the spatial and time components together illustrates the robust nature of this approach.

Conclusions

The time repeatability of snowmelt has significant implications for managing water in real-time and under climate change. We have demonstrated the recurrent pattern of melt, which offers a snapshot of how melt occurs spatially, also describes temporal repeatability. Not only does snowmelt on average follow the PCA SDC as well as the linear PCA values versus time, but individual years follow the curve. We have applied the PCA spatial model to remove cloud cover, developed a

dimensionless PCA SDC, a dimensionless linear relationship of PCA values versus normalized time, adjusted for secondary snowfall events, and normalized 17 melt periods. We applied a cloud removal confidence metric prior to SDC fitting and found the SDC fit with an average RMSE of 0.030. Through these steps we have demonstrated the PCA model of the recurrent pattern of melt accurately describes the spatial component of snowmelt but equally important it also describes the temporal repeatability of snowmelt. This novel approach and finding provide the framework for normalizing and comparing melt periods.

Throughout the study period a broad range in melt timing occurred and was easily accommodated by the PCA SDC. The parameters used to fit the PCA SDC to a melt period, I_m and D_m, ranged from 52.2-108.1 and 76.7-146.9 days, respectively. The model handled the observed variable snowpack conditions and demonstrated that a single normalized curve can be used to represent melt in any year. The PCA SDC is also a simple transformation of the linear relationship of PCA values against normalized time. We also demonstrated individual years follow the linear description with R-squared values ranging from 0.946 to 0.992. The linear relationship also allowed us to address secondary snowfall events. By shifting the PCA values one day at a time we recorded increases in R-squared (0.961-0.996) as well as a better model fit as described by the AIC. This is a systematic and simple method for adjusting snow covered area depletion for secondary snowfall events. The spatial and temporal repeatability captured by the PCA model has the potential to change the way snowmelt runoff modeling is approached in retrospective, real-time, and climate simulations.

The PCA method extracts a linear transformation of average behavior; however, the novelty of our work is every individual year is linear with time. The recurrent pattern of snow is spatially recurrent and when paired with time it is temporally recurrent. Simply put this method allows us to normalize the often-erratic behavior of snowmelt making every year comparable. Extreme variability in snow accumulation and timing has been difficult to model. For real-time modeling, the spatial and temporal information captured in the PCA SDC collectively provide guiding stationary variables, or boundary conditions. The prospect of forecasting melt, given the repeatable spatial data and ability to normalize the temporal component along with the simple linear relationship, has significant potential and important implications for water management.

Water management relies on information about the rate, timing, and amount of melt occurring daily. This requires significant data acquisition and ground-based networks to interpolate spatial data. The method presented in this article only requires remote sensing to describe the rate and timing of snow depletion. Ungauged watersheds are of great interest because remotely sensed data is available

and the repeatable spatial and temporal pattern of SCA depletion exists and can be implemented to model snowmelt. Applications of the repeatable pattern of snowmelt may be an emerging field of research. Woodruff & Qualls (2019) applied the pattern for cloud removal, and we demonstrated the novelty of this method beyond simple cloud removal. Normalizing snowmelt with the recurrent pattern could be the initial step towards a paradigm shift in our understanding of snowmelt. The highly variable system of snowmelt modeling is simplified using a simple watershed characteristic: spatial patterns.

References

Adams, W. P. (1976). Areal differentiation of snow cover in east central Ontario, *Water Resources Research, 12*(6), 1226– 1234, doi:10.1029/WR012i006p01226.

Akaike, H. (1974). A new look at the statistical model identification. *IEEE Transactions on Automatic Control, 19*(6), 716–723. https://doi.org/10.1109/TAC.1974.1100705

Andreadis, K. M., & Lettenmaier, D. P. (2006). Assimilating remotely sensed snow observations into a macroscale hydrology model. *Advances In Water Resources*, *29*(6), 872–886.

Balk, B., & Elder, K. (2000). Combining binary decision tree and geostatistical methods to estimate snow distribution in a mountain watershed. *Water Resources Research, 36*(1), 13–26.

Barnett, T. P., Adams, J. C. & Lettenmaier, D. P. (2005). Potential impacts of a warming climate on water availability in snow-dominated regions. *Nature*, 438, pp.303–309.

Brubaker, K. L., Pinker, R. T., & Deviatova, E. (2005). Evaluation and Comparison of MODIS and IMS Snow-Cover Estimates for the Continental United States Using Station Data. *Journal of Hydrometeorology*, *6*(6), 1002–1017. https://doi.org/10.1175/JHM447.1

Brunsdon, C., & Comber, L. (2019). *An introduction to R for spatial analysis & mapping* (Second edition.). SAGE Publications.

Cherkauer, K. A., & Lettenmaier, D. P. (2003). Simulation of spatial variability in snow and frozen soil. *Journal of Geophysical Research: Atmospheres, 108*(D22).

Dietz, A., Wohner, C., & Kuenzer, C. (2012). European Snow Cover Characteristics between 2000 and 2011 Derived from Improved MODIS Daily Snow Cover Products. *Remote Sensing, 4*(8), 2432-2454. doi:10.3390/rs4082432.

Dingman, S. L. (2008). *Physical hydrology* (2nd ed.). Long Grove, Ill.: Waveland Press Inc.

Dong, C., & Menzel, L. (2016). Producing cloud-free MODIS snow cover products with conditional probability interpolation and meteorological data. *Remote Sensing of Environment, 186*, 439

Gafurov, A., & Bárdossy, A. (2009). Cloud removal methodology from MODIS snow cover product. *Hydrology and Earth System Sciences, 13*(7), 1361-1373.

Gafurov, A., Lüdtke, S., Unger-Shayesteh, K., Vorogushyn, S., Schöne, T., Schmidt, S., Kalashnikova, O., & Merz, B. (2016). MODSNOW-Tool: An operational tool for daily snow

cover monitoring using MODIS data. *Environmental Earth Sciences, 75*(14), 1-15. doi:10.1007/s12665-016-5869-x.

Gao, Y., Xie, H., Lu, N., Yao, T., & Liang, T. (2010). Toward advanced daily cloud-free snow cover and snow water equivalent products from Terra–Aqua MODIS and Aqua AMSR-E measurements. *Journal of Hydrology, 385*(1), 23-35. doi:10.1016/j.jhydrol.2010.01.022.

Hall, D. K., & Riggs, G. A. (2007). Accuracy assessment of the MODIS snow products. *Hydrological Processes, 21*(12), 1534-1547. doi:10.1002/hyp.6715.

Hall, D.K. & Riggs, G. A. (2015). *MODIS Snow Products Collection 6 User Guide*. doi: http://nsidc.org/sites/nsidc.org/files/files/MODIS-snow-user-guide-C6.pdf. [July 12, 2018].

Hall, D. K. & Riggs, G. A. (2016). *MODIS/Terra Snow Cover Daily L3 Global 500m Grid, Version 6*. [NDSI snow cover]. Boulder, Colorado USA. NASA National Snow and Ice Data Center Distributed Active Archive Center. doi: https://doi.org/10.5067/MODIS/MOD10A1.006. [January 2017 - March 2018].

Hall, D. K., Riggs, G. A., Digirolamo, N. E., & Roman, M. O. (2019). Evaluation of MODIS and VIIRS cloud-gap-filled snow-cover products for production of an Earth science data record. *Hydrology And Earth System Sciences*, *23*(12), 5227–5241. https://doi.org/10.5194/hess-23-5227-2019.

Homer, C.G., Dewitz, J.A., Yang, L., Jin, S., Danielson, P., Xian, G., Coulston, J., Herold, N.D., Wickham, J.D., & Megown, K., (2015). Completion of the 2011 National Land Cover Database for the conterminous United States-Representing a decade of land cover change information. *Photogrammetric Engineering and Remote Sensing*, v. 81, no. 5, p. 345-354

Jensen, J. (2016). *Introductory Digital Image Processing: A Remote Sensing Perspective* (4th ed.).

Kasurak, A., Kelly, R., Brenning, A., & Pelto, Mauri S. (2011). Linear mixed modelling of snow distribution in the central Yukon. *Hydrological Processes, 25*(21), 3332–3346.

König, M. & Sturm, M. (1998). Mapping snow distribution in the Alaskan Arctic using aerial photography and topographic relationships, *Water Resour. Res., 34*(12), 3471–3483, doi:10.1029/98WR02514.

Li, X., Fu, W., Shen, H., Huang, C., & Zhang, L. (2017). Monitoring snow cover variability (2000–2014) in the Hengduan Mountains based on cloud-removed MODIS products with an

adaptive spatio-temporal weighted method. *Journal of Hydrology, 551*, 314-327. doi:10.1016/j.jhydrol.2017.05.049.

Luce, C. H., & Tarboton, D. G. (2004). The application of depletion curves for parameterization of subgrid variability of snow. *Hydrological Processes, 18*(8), 1409-1422. doi:10.1002/hyp.1420.

Martinec, J. (1982). Runoff Modeling from Snow Covered Area. *Geoscience and Remote Sensing, IEEE Transactions on, GE-20*(3), 259-262. doi: 10.1109/TGRS.1982.350440.

Martinec, J., Rango, Albert, Major, E, & United States. National Aeronautics Space Administration. Scientific Technical Information Branch. (1983). *The snowmelt-runoff model (SRM) user's manual*. National Aeronautics and Space Administration, Scientific and Technical Information Branch.

Martinec, J. & Rango, A. (1986). Parameter values for snowmelt runoff modelling. *Journal of Hydrology*, 84(3), pp.197–219.

Matiu, M., Jacob, A., & Notarnicola, C. (2019). Daily MODIS Snow Cover Maps for the European Alps from 2002 onwards at 250 m Horizontal Resolution Along with a Nearly Cloud-Free Version. *Data*. doi: http://doi.org/10.5281/zenodo.3566703.

Nagler, T., Rott, H., Malcher, P., & Müller, F. (2008). Assimilation of meteorological and remote sensing data for snowmelt runoff forecasting. *Remote Sensing of Environment, 112*(4), 1408–1420. https://doi.org/10.1016/j.rse.2007.07.006

Parajka, J., & Blöschl, G. (2008). Spatio-temporal combination of MODIS images – potential for snow cover mapping. *Water Resources Research, 44*(3), N/a. doi:10.1029/2007WR006204.

Parajka, J., Pepe, M., Rampini, A., Rossi, S., & Blöschl, G. (2010). A regional snow-line method for estimating snow cover from MODIS during cloud cover. *Journal of Hydrology, 381*(3), 203-212. doi:10.1016/j.jhydrol.2009.11.042.

Riggs, G.A., Hall, D. K., & Roman, M. O. (2017). Overview of NASA's MODIS and Visible Infrared Imaging Radiometer Suite (VIIRS) snow-cover Earth System Data Records. *Earth System Science Data, 9*(2), pp.765–777. doi:10.5194/essd-9-765-2017.

Riggs, G.A., Hall, D.K. & Román, M.O. (2019). *NASA S-NPP VIIRS Snow Cover Products Collection 1 (C1) User Guide*. doi: https://nsidc.org/sites/nsidc.org/files/technical-references/VIIRS_snow_products_user_guide_version_8.pdf. [April 30, 2020].

Schlogl, S., Lehning, M., Fierz, C., & Mott, R. (2018). Representation of Horizontal Transport Processes in Snowmelt Modeling by Applying a Footprint Approach. Frontiers in Earth Science, 6, Frontiers in Earth Science, Oct 8, 2018. doi: 10.3389/feart.2018.00120.

Sturm, M., & Wagner, A. (2010). Using repeated patterns in snow distribution modeling: An Arctic example. *Water Resources Research, 46*(12), N/a. doi:10.1029/2010WR009434.

Tedesco, M., Derksen, C., Deems, J. S., & Foster, J. L. (2015). Remote sensing of snow depth and snow water equivalent. In Remote Sensing of the Cryosphere (pp. 73–98). John Wiley & Sons, Ltd. https://doi.org/10.1002/9781118368909.ch5

Tran, M., Nguyen, K.-L., Ombadi, S., Hsu, X., Sorooshian, H., & Qing, P. (2019). A cloud-free MODIS snow cover dataset for the contiguous United States from 2000 to 2017. *Scientific Data, 6*(1), 180300. https://doi.org/10.1038/sdata.2018.300

Wang, L., Sun, L., Shrestha, M., Li, X., Liu, W., Zhou, J. Yang, K., Lu, H., & Chen, D. (2016). Improving snow process modeling with satellite-based estimation of near-surface-air-temperature lapse rate. Journal of Geophysical Research: Atmospheres, 121(20), 12,00512,030. doi: 10.1002/2016JD025506

Wang, X., & Xie, H. (2009). New methods for studying the spatiotemporal variation of snow cover based on combination products of MODIS Terra and Aqua. *Journal of Hydrology, 371*(1), 192-200. doi:10.1016/j.jhydrol.2009.03.028

Woodruff, C. D., & Qualls, R. J. (2019). Recurrent snowmelt pattern synthesis using principal component analysis of multiyear remotely sensed snow cover. *Water Resources Research, 55*. https://doi.org/10.1029/2018WR024546

Chapter 3: K-Means Cluster Derivation of Multi-Year Recurrent Snow Cover Pattern over a Mountainous Watershed

Introduction

The importance of water cannot be overstated. One underexploited variable to monitor, model, and manage the finite resource of water is spatial patterns of snowmelt. The existence of interannually recurring spatial patterns of snowmelt has long been acknowledged in the literature across multiple climactic and topographic regions (Adams, 1976; König & Sturm, 1998; Luce & Tarboton, 2004; Sturm & Wagner, 2010; Wang & Xei, 2009; Parr et al., 2020; Woodruff & Qualls, 2019). The difficulty in using this variable is no one has been able to extract it until Woodruff & Qualls (2019). They developed a way to extract the recurrent pattern of snowmelt through remotely sensed snow-covered area (SCA) data. The inaugural application of this type of model was cloud cover removal; however, applications extend beyond simple cloud removal. We propose and test another method for extracting the recurrent pattern of snowmelt from remotely sensed imagery. Remotely sensed imagery offers worldwide coverage, and these patterns may exist across many landscapes.

Spatial patterns of snowmelt are a function of the landscape and the climate. Parr et al. (2020) demonstrated that redistribution of snow due to wind in the arctic tundra is a function of the topography. The depth of a snow deposit was defined by the topography and the prevailing winds. These snow deposits led to repeatable spatial patterns in snowmelt even if the timing of when they melted changed. This demonstration of repeatable patterns in the arctic, a flat rolling landscape further expresses the widespread existence of patterns. In complex and non-complex terrain, it has been shown snowmelt is driven by elevation, aspect, slope, vegetation, and many other environmental factors (Hock, 2003). Many of these drivers are stable or unchanging from year to year. For example, extraterrestrial shortwave radiation at a given location and time of year does not change and the aspect of a slope is also fixed. North of the Tropic of Cancer, for example, the combination of watershed characteristics and the diurnal/seasonal cycle of the earth-sun orientation leads to increased shortwave radiation loading on southern facing slopes compared with northern aspects (Dingman, 2008). These characteristics define the spatial pattern of snowmelt across multiple landscapes.

Spatial patterns have inherent properties useful to snowmelt runoff modeling. Spatial information at the right scale is a critical tool for monitoring and modeling snowmelt. Spatial patterns offer a framework for investigating many important questions about snowmelt. The location of the

snow to land interface, that is, the snowline, plays a vital role in modeling energy fluxes. Schlogl et al. (2018) demonstrated snowmelt rate near the snowline increased by 25-30% due to advection from the snow free surface in the Dischma Valley in the Swiss Alps. The near surface temperature lapse rate has also been shown to influence streamflow. Wang et al. (2016) demonstrated that different temperature lapse rate scenarios produced streamflow differences as large as 24%. The linear lapse rate which is often applied produced the lowest yearly simulated discharge accuracy (Nash coefficient of 0.414) while remotely sensed data acquired by the Moderate Resolution Imaging Spectroradiometer (MODIS) produced the highest streamflow accuracy with a Nash coefficient of 0.696. The lapse rate is dependent on snow location. The spatial pattern may also be helpful in determining snow water equivalent (SWE). Luce et al. (2004) observed spatial patterns in a study where modified depletion curves (MDC) were developed relating Snow Water Equivalent (SWE) to SCA. A main issue they noted is these curves could not be found "*a priori*". Determination of the spatial melt pattern would supply half the information needed to quantify SWE by providing a repeatable description of SCA over space and time.

Woodruff & Qualls (2019) processed multiple years of remotely sensed MODIS SCA data using Principal Component Analysis (PCA) to develop the recurrent spatial snowmelt pattern "PCA model". They achieved spatial accuracies of 84.9-97.5% when comparing the modeled SCA versus actual measured SCA. MODIS collects daily worldwide imagery at a spatial resolution of 500 meters by 500 meters (Hall & Riggs, 2015). The sensor is flown aboard two NASA satellites, Terra and Aqua, which collect SCA data at separate times each day. The Terra Satellite MODIS was used in their study. An average spatial accuracy of 93% has been demonstrated for MODIS with ground-based data on cloud free days (Hall & Riggs, 2007). No uncertainty has been more detrimental to widespread adoption of the MODIS dataset for snowmelt modeling than cloud cover. A significant amount of research has been dedicated to removing cloud cover. In 2020 NASA began producing their own daily cloud free snow cover image dataset (Hall et al., 2019), however pixel values during cloudy periods in this dataset simply propagate the previous non-cloud obscured pixel value throughout the duration of the cloudy period.

It is particularly enticing to perform cloud removal on MODIS imagery because it has a daily temporal resolution, which is extremely useful for snowmelt modeling. Methods for cloud removal can be categorized as either spatial or temporal interpolation, or some combination of the two. Spatial interpolation takes advantage of nearby pixels. For example, a simplified version might say if a pixel is cloud covered, but adjacent to a snow-covered pixel the cloud-covered pixel would be interpolated

as a snow-covered pixel. More advanced methodologies use a regional snow line approach, proposed first by Parajka et al. (2010). This approach calculates the mean elevation of all snow pixels and the mean elevation of all land pixels. The elevation of a cloud covered pixel is compared to the mean snow and land elevations and if the elevation is greater than the mean snow elevation it is classified as snow. Conversely, if it is less than the mean land elevation it is classified as land. A cloud covered pixel between these mean elevations is considered to lie in a transition zone and is classified as partially snow covered. They obtained annual accuracies ranging between 48.7 and 81.5%. This method was extended by Krajčí et al. (2014) who obtained accuracies of 73-92%. Both methods experience higher uncertainty in the elevation transition zone, during the melting time-period, and when cloud cover is extensive.

Temporal interpolation aims to classify a cloud covered pixel based on imagery at separate times. Many research groups have used a combination of the MODIS sensors on the Terra and Aqua satellites because they have different pass over times. This combination has been shown to reduce cloud cover from an average cloud coverage of 63% to 52% (Parajka & Blöschl, 2008). Other methods use imagery from either preceding or succeeding days. Parajka & Blöschl (2008) achieved reductions from 63% average cloud cover to 34% using one previous day to infill. They further reduced average cloud coverage to 4% by using the seven previous days. While annually averaged accuracies were high (92.1 - 94.4%) using this method, the largest errors persisted during the accumulation and ablation periods. This large uncertainty occurs during the most valuable time because cloud coverage is high and spatial changes in SCA occur rapidly. The main issue with these methods is a multiple day window for infilling cloud covered pixels assumes the pixel does not change from snow to snow free during the period. This may not be true and could explain the uncertainty during accumulation and melt.

Several cloud removal models combine spatial and temporal interpolation. The MODSNOW-tool uses an eight-step method to remove all cloud cover for even 100% cloud covered imagery (Gafurov et al., 2016). The first step is the combination of Terra and Aqua satellites, followed by application of a conditional probability, a monthly snow probability, a virtual station to pixel relationship, a temporal combination, maximum and minimum snow lines, adjacent pixel combination, and finally multiple snow onset and melt dates (Gafurov et al., 2016). The conditional probability through the virtual station to pixel relationship steps are of particular interest. This step represents the probability of a pixel being snow covered based on the presence of snow at a ground station. The monthly probability states certain pixels are snow covered with high probability within

certain months. The virtual station to pixel relationship is like the conditional probability except that it uses an observed image pixel value as a virtual station in place of a ground measurement station observation. The probability of a pixel being snow covered is related to whether snow is observed at a different pixel, or the virtual station. It is important to note these probabilities are derived on an annual basis. During snow free months there will be a high conditional probability that some pixel will be snow free given snow free conditions at a virtual station, however during transitional months a reduction in accuracy should be expected. This is reflected in the accuracy range of 77.3-99.8% where 77.3% is measured during the melting season (Gafurov et al., 2016). The last step of the MODSNOW-tool uses snow onset and melt dates from multiple years of data to derive a threshold date for a pixel to be snow covered.

The conditional probability has gained traction as an attractive method for removing cloud cover. Dong & Menzel (2016) expanded the MODSNOW-tool to include meteorological data, achieving an accuracy of 92% during the snow season. The Adaptive Spatio-Temporal Weighted Model (ASTWM) developed by Li et al. (2017) obtained 93.11% to 98.92% accuracy employing a two-step method which uses a conditional probability of the spatial and temporal coverage of snow. The ASTWM model uses a 15-day window for temporal interpolation, which includes previous and future images for a cloudy pixel on a given day. The 15-day window is too large to capture the rapidly changing SCA (Dong & Menzel, 2016).

Spatial patterns of snowmelt offer predictive power that all other cloud removal methods lack. Models of spatial patterns rely on the repeatable nature of snowmelt across a landscape to remove cloud cover (Woodruff & Qualls, 2019). They simply determine *when* in the melt cycle the watershed is. Each pixel in the watershed has a *relative timing of melt* that describes when it melts in relation to all other pixels in the watershed. A collection of pixels whose relative melt timing values all fall within a narrow range would all melt concurrently, and the locations of those pixels throughout a watershed would define the snowline at the time of occurrence of that relative melt timing. Therefore, given a partially cloud-obscured image if even a small segment of the snowline is visible in the image, the spatial pattern model provides the information necessary to infill the remainder of the snowline and the value of all other pixels across the watershed with high spatial accuracy. The model indicates which pixels must melt next as well. If for example a clear day is followed by seven cloudy days, the model would indicate which pixels are likely melting beneath the cloud cover. This predictive power is unlike any other cloud removal method.

The purpose of this work is to derive the recurrent pattern of snowmelt using a K-means clustering analysis for the Upper Snake River Basin. This is a different statistical approach from that employed by Woodruff & Qualls (2019) who used the PCA. We will quantify the accuracy of this approach when compared against cloud-free independent data, directly compare the model with the model derived by Woodruff & Qualls (2019) and compare the cloud removal accuracies of both approaches. K-means clustering and PCA are mathematically different in how they approach and produce the spatial model. This direct comparison will highlight the implications of two different methods arriving at a similar, or different, spatial model of the recurrent pattern of snowmelt. There is significant scientific merit and potential for this new class of models in spatially modeling snowmelt.

Study Site and Data

Study Site

The study area for this research covers 3,465 mi^2 (8,894 km^2) and elevations range between 5,799 - 13,760 feet (1,737 – 4,194 meters). It is formally known as the Upper Snake Basin (Figure 3.1) bordered to the West by the Teton Mountains and includes the hydrologic units of Snake Headwaters, Gros Ventre, and Greys-Hobock. The watershed experiences complete seasonal snow coverage. It serves as an important basin for Idaho agriculture, power generation, in-stream fish requirements, municipal and industrial applications (Qualls et al., 2013). This watershed is representative of the many watersheds around the world which serve as important locations of snow water storage. Land cover in the watershed is variable with 46.6% evergreen forest, 1.3% deciduous and mixed forest, 45.4% shrub and grass land, and the remaining 6.7% agriculture, developed land, and wetlands according the 2011 National Land Cover Database (Homer et al., 2015).

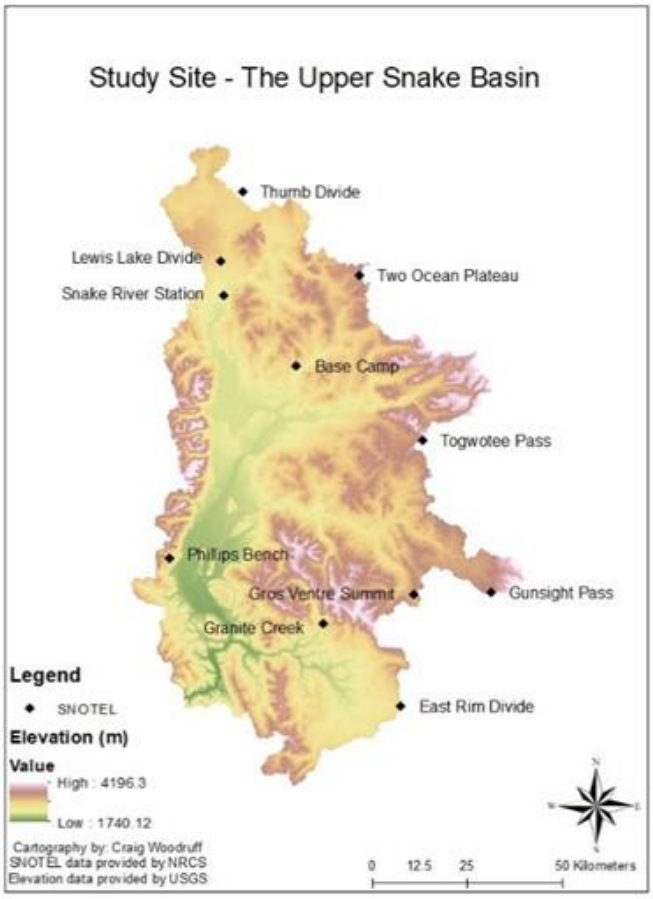

Figure 3.1: Upper Snake Basin with associated SNOTEL stations.

The catchment also has 11 SNOw TELemetry sites (SNOTEL) operated and maintained by the Natural Resource Conservation Service (NRCS). Each site measures a 2 by 2 meter snow pillow which gives hourly Snow Water Equivalent (SWE) measurements. The 19-year study period recorded a wide range in snow conditions. Table 3.1 summarizes the snow seasons for 2000-2018. We see in the years 2000-2016 the maximum SWE recorded at each station is nearly three times larger in the biggest snowpack year compared to the smallest. The years 2017 and 2018 also represent a variety of snow conditions and were used as a validation dataset, discussed later. The melt duration in days varied greatly between 2017 and 2018. The bolded SNOTEL stations recorded a difference in melt duration (the time period from maximum SWE to zero SWE in days) from 23 days to 49 days at Base

Camp even though the difference in SWE is minimal 1-11 inches. The study region recorded a wide range in SWE and melt duration during the study period.

Table 3.1: Variation in SWE and melt timing for study period and verification period of 2000-2016 and 2017-2018 respectively.

SNOTEL Station ID	*Elevation (ft)*	*Largest Max SWE 2000-2016 (in)*	*Smallest Max SWE 2000-2016 (in)*	*Melt Period 2017 (days)*	*Melt Period 2018 (days)*	*Melt Period Difference 2017-2018 (days)*	*Max SWE Difference 2017 - 2018 (in)*
Base Camp	**7060**	27.1	8.7	81	32	**49**	**7.3**
Thumb Divide	**7980**	29.5	8.9	56	33	**23**	**1.2**
Lewis Lake Divide	7850	56.9	19.1	48	51	-3	3.1
Snake River Station	**6920**	23.2	9.3	64	37	**27**	**2.4**
Two Ocean Plateau	9240	55.1	22.8	66	62	4	11.5
Togwotee Pass	9580	42.7	19.2	58	67	-9	0.9
Phillips Bench	8200	44	18.8	48	50	-2	8.8
Gros Ventre Summit	8750	21.7	9.1	38	45	-7	4.2
Gunsight Pass	9820	27.3	10.5	49	52	-3	7
Granite Creek	**6770**	30.1	10	75	40	**35**	**11.3**
East Rim Divide	**7930**	18.8	6.7	58	28	**30**	**5.8**

Data Sources

The model was developed using remotely sensed data. The MODerate Resolution Imaging Spectoradiometer (MODIS) sensor on board the Terra satellite was selected. Daily imagery from the version six data product, MOD10A1, distributed by the National Snow and Ice Data Center (NSIDC) was downloaded for processing. The NDSI snow cover product was selected for this study. The NDSI or normalized difference snow index is a combination of bands four and six. Band four (0.545-0.565 µm) is within the visible spectrum and band six (1.628-1.652 µm) is in the mid infrared. The equation subtracts band six from four and divides this value by their sum. To convert the NDSI snow cover to fractional SCA a threshold of 0.4 was applied, as documented in the version six user guide (Hall & Riggs, 2015). No temporal interpolation with sensor combinations was used and therefore the Terra satellite was selected. Although the band seven of the Aqua Satellite has been restored, Hall et al., (2019) demonstrated the Aqua sensor produces more commission errors than the Terra sensor. The Upper Snake Basin is captured by the MODIS swaths h09v04 and h10v04. Images from 2000 through 2016 were used to develop the model and accuracy was calculated with data from 2017 and 2018.

SNOTEL data distributed by the Natural Resource Conservation Service (NRCS) was used during the initial steps of the model derivation. There are eleven sites in the watershed. Base Camp station ID 314 daily SWE measurements were downloaded for 2000-2016. This station is located at an elevation of 7060 feet, and over the 19-year study period often was the first station to melt completely, as identified by the first date SWE equals 0.0 inches after the date of peak SWE.

Methods

Data Preparation

Remote sensing was used to capture the recurrent pattern of melt. We capture the single year melt information by identifying when each pixel melts. The last day snow (LDS) is seen and the first day land (FDL) is seen on a pixel-by-pixel basis describes the timing of melt. LDS and FDL dates are intentionally chosen to correspond to the first date of melt-out for each pixel and ignore subsequent or secondary snowfall events. We extract the FDL and LDS one year at a time by iterating through all the available imagery. The values of FDL and LDS are saved to two output files containing the day of year (DOY) values for each pixel. The two output files are identical in spatial resolution and geolocation to MODIS imagery. The timing of peak SWE based on SNOTEL records was used to guide when during the snow season to begin the image search process to capture a pixel's initial melt out date rather than those of secondary snowfall events. Although it was expedient to use SNOTEL for this purpose, the starting DOY to initiate the search could also be determined by inspection of a given year's MODIS imagery. In the data preparation stage only images from the years 2000 through 2016 were used, a total of 34 output files (17 FDL and 17 LDS). The difference between the FDL and LDS images for each year is the number of days each pixel was cloud covered during the period melt occurred for each pixel in each year. This initial step was first proposed by Woodruff & Qualls (2019) and should be referred to for an in-depth explanation.

Cluster Model

Each FDL describes the day of year a pixel melts, or changes from snow to snow free, and we hypothesize a single model developed using multiple years (FDLs) will describe the recurrent melt pattern. The FDLs are aggregated into a matrix where a given column contains all the FDL values recorded for all the pixels in the watershed for a single year, and a given row contains all the FDL values for every year for a single pixel. For example, in row n the FDL value for column m is contained, and the FDL value for column m+1 in row n describes the DOY the same pixel melted in a different year. The matrix dimensions are therefore N by M, where N is 41,503 (the number of pixels occupying the watershed in an image), and M is 17 (the number of years for which FDL was

calculated). Once organized a K-means clustering analysis was applied to the dataset. K-means clustering analysis partitions a dataset into groups where each group is made up of values of similar nature.

A K-means clustering analysis partitions a dataset into K_c clusters, where K_c is a user defined parameter. Each cluster is defined by a mean vector referred to as a centroid (R). K-means clustering is an iterative process which assigns all the points in a dataset to a cluster defined by R. The number of centroids is equal to the number of clusters. These clusters are chosen by minimizing the Within Group Sum of Squares Error (WGSS). In the first iteration the centroids for each cluster are guessed, and each data point is assigned to a cluster based on its Euclidean distance from the cluster centroid, R. All the points assigned to a cluster can be used to calculate the sum of squares error for each cluster, and WGSS is the cumulative sum of all the error terms for each cluster. In the second iteration the centroids are moved, the data points are reassigned to clusters, and the WGSS is calculated. The partitioning which produces the minimum WGSS is selected as the optimal grouping of the data. The number of iterations in theory should be as many as are required to achieve the minimum WGSS, however it is impossible to check all possibilities with the current computing capabilities. The user therefore must specify the number of iterations.

The WGSS can be described by equation 3.1. This is true for K clusters, with centroids R, applied to a matrix of size N by M where a matrix element is identified by n, m. The Euclidean distance error term is defined by d(). At each iteration, equation 3.1 is applied and the WGSS is saved. The best fit of the cluster model is found by the partitioning that minimizes the WGSS (Everitt & Hothorn, 2011).

Equation 3.1

$$WGSS = \sum_{k=1}^{K} \sum_{i \in R_k} \sum_{m=1}^{M} d(x_{nm} - R_{km})^2$$

We hypothesize the K-means clustering analysis will group pixels together based on their *relative* melt timing. Our hypothesis suggests the relative melt timing of a cluster is described by its centroid, R_t. In the FDL matrix each pixel (row) has 17 values which describe actual melt timing for that pixel for each year. A row within this matrix describes the *pixel's* overall relative melt timing, r_t. The r_t of each pixel does not assume the pixel melts on the same day each year, but melts at the same time in relation to all other pixels. The K-means clustering analysis uses the r_t to partition the data into clusters with centroids R_t. Each cluster R_t should group pixels of similar r_t. The WGSS is

therefore calculated based on the Euclidean distance of the r_t which only describes a time value. Spatial information is not used to partition the data, only each pixel's melt timing.

We applied the K-means clustering analysis to the FDL dataset with K_c equal to 20 and 25 optimization iterations. The R_t is used to order the clusters for the final model. The cluster with the smallest R_t will melt first, the next larger R_t melts second, and so on. We can spatially model SCA selecting r* to group the clusters by R_t. Let us assume R_{t1} which is the smallest R_t contains 5% of the total pixels, and R_{t2} is the second smallest R_t and it contains 2% of the total pixels. To produce a representation of 95% snow covered area we select r* as one. By this selection R_{t1} is considered snow free (5% area) and any R_t greater than r* is snow covered or the remain 95% of the pixels. If we select r* as two, then R_{t1} and R_{t2} are snow free (7% area) and R_{t3} through R_{t20} are snow covered (93% area). Because the number of clusters is finite, the percentage of area changes in finite increments rather than continuously with this model.

The ordering of R_t provides the temporal component which governs how the snow cover changes spatially across the watershed from 100% coverage to 0% coverage. If this is true and our hypothesis is correct, then the cluster model will extract the multi-year recurrent pattern. The K-means clustering analysis is only run one time to produce the final model. After it is developed the spatial accuracy can be quantified.

Accuracy Assessment

The final model is validated for accuracy using cloud free days (≤5% cloud cover by area) in 2017 and 2018. Using the same methods as Woodruff and Qualls (2019) the VPE, or visible pixel error, is used to choose the model best fit to a clear day image. VPE is shown in equation 3.2, where T_P is the total visible pixels, I_L is the number of pixels incorrectly modeled as land but measured as snow and I_S is the number of pixels incorrectly modeled as snow but measured as land.

Equation 3.2

$$VPE = \sqrt{\frac{{I_l}^2 + {I_s}^2}{{T_p}^2}}$$

The VPE is calculated for the model possibilities, or each combination of R_t. The R_t combination which produces the smallest VPE is chosen. Spatial accuracy is calculated after the R_t combination is chosen. The spatial accuracy is calculated by equation 3.3.

Equation 3.3

$$Accuracy = \left(1 - \frac{I_l + I_s}{T_p}\right) * 100\%$$

For cloud removal purposes the VPE is applied to choose the best model fit based only on the visible pixels. The comparison between the PCA and Cluster models discussed later also uses equation 3.2 to choose the best fit and equation 3.3 to calculate accuracy.

Results

In this research we sought to develop a single model which describes the spatial and temporal pattern of snow-covered area. Imagery data from 17 years was processed and statistically combined using K-means clustering, which we will refer to as the "Cluster model". The Cluster model results are presented in the following order. The model descriptive results, an assessment of the model's spatial accuracy when compared with two independent years (2017 and 2018), and a direct comparison between the Cluster model and the PCA model developed by Woodruff and Qualls (2019) including a cloud removal comparison.

Cluster Model

The FDL imagery was used as input for the model derivation as it represents the first day there is confidence a pixel has melted (Figure 3.2). Figure 3.2 presents the FDL images for 2001 through 2010. The spatio-temporal patterns of melt are quite similar, even though the actual melt dates by area and total duration of melt vary widely among the years. For example, 2005 recorded the earliest FDL value as DOY 22 and the latest as DOY 197, while 2008 recorded a range of DOY 93 to DOY 212. Melt timing varies significantly across the years.

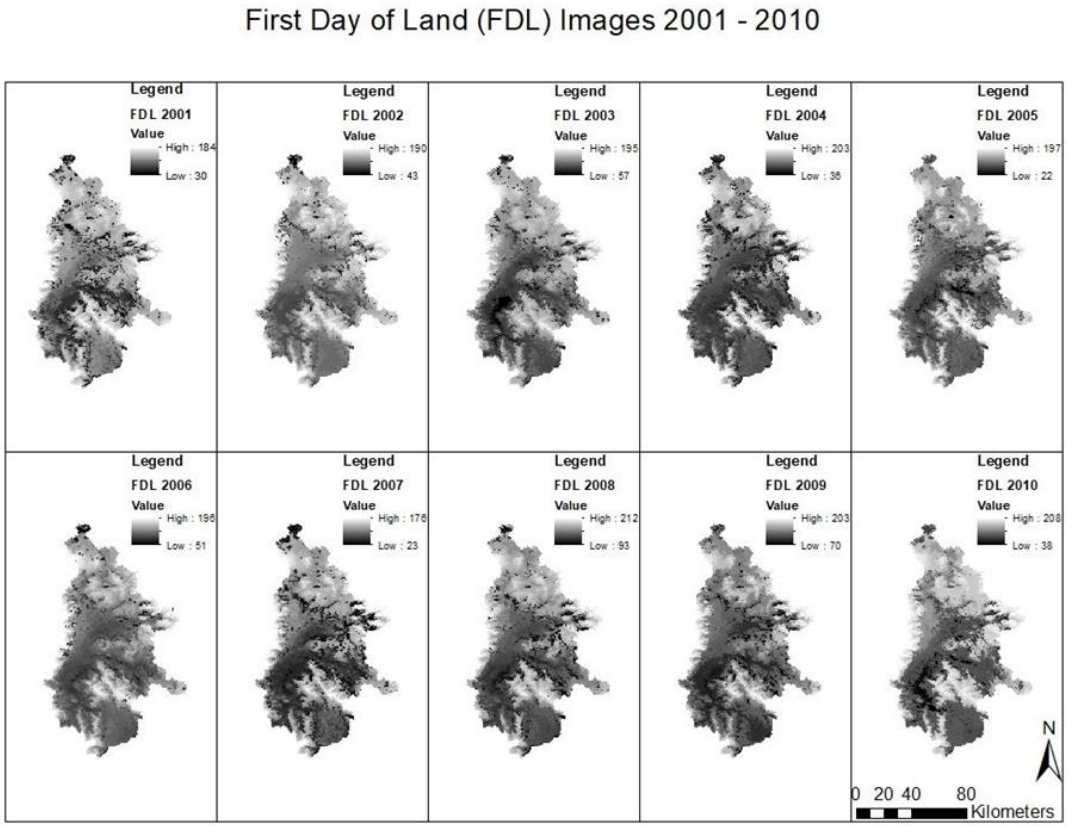

Figure 3.2: Comparison of the First Day of Land images for 2001-2010.

These FDL images, along with the seven not pictured, were processed using a K-means clustering analysis. The distribution of each cluster is shown in Figure 3.2. Each bar's height shows how much of the total area is assigned to each cluster, and the "X" shows the R_t value for each cluster. The amount of area described by each cluster varies from 0.66% (cluster 5) to 10.57% (cluster 6). Each R_t represents the centroid of melt timing for the cluster. As shown in Figure 3.3, the values of R_t are ordered from first to melt to last. In some cases, the delta between R_t is large meaning the melt timing is further apart for the clusters, while in others it is small meaning the clusters melt closer together in time.

Each cluster's melt timing is identified by R_t which is sequential. This sequence describes SCA from 100% to 0% through the aggregation of clusters. Once one cluster has melted it represents a percentage of snow free area. The values of R_t can be used to convert the Cluster model to a binary snow and snow free image. Once a threshold, r*, has been selected all clusters with R_t less than r* can be converted to snow free and all above r* as snow covered.

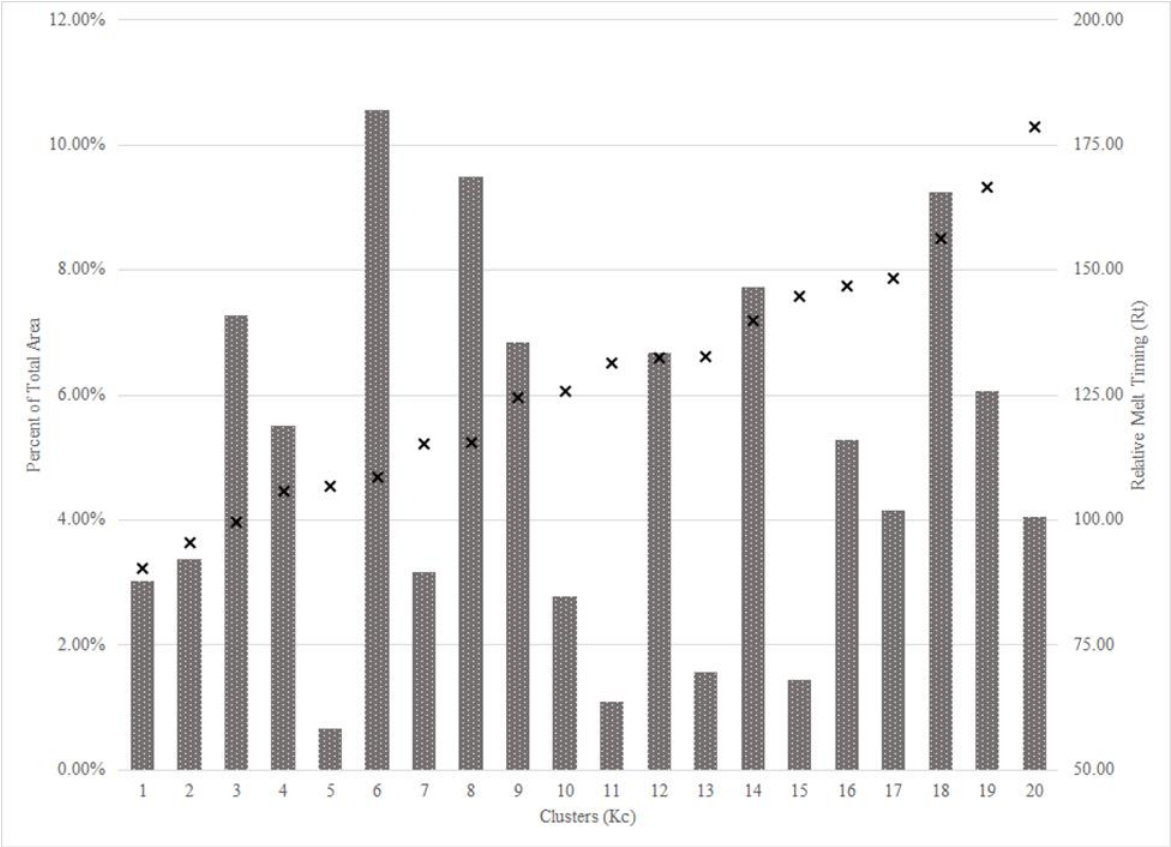

Figure 3.3: Cluster order by R_t (shown as "X"), and percentage of area each cluster describes shown by bars.

The Cluster model is shown in Figure 3.4. The light blue melts first given as $R_{t1,}$ and the dark melts last given as R_{t20}. If we compare the spatial model to Figure 3.3, the lightest blue in Figure 3.4 is associated with the first bar or smallest Rt in Figure 3.3. R_{t1} represents 3% of the total area. Our r* value for representing 97% SCA is therefore equal to 1, or R_{t1} is snow free and R_{t2}-R_{t20} is snow covered. To represent the next step in SCA depletion we set r* to two. Referring to Figure 3.3 we see that R_{t1} plus R_{t2} equals 6.4%. At this r* our SCA is 93.6%. In Figure 3.4 the complementary areas are the lightest blue and the second lightest blue or 6.4% snow free and 93.6% SCA. Simply by selecting r* we represent a stepwise addition of cumulative SCA.

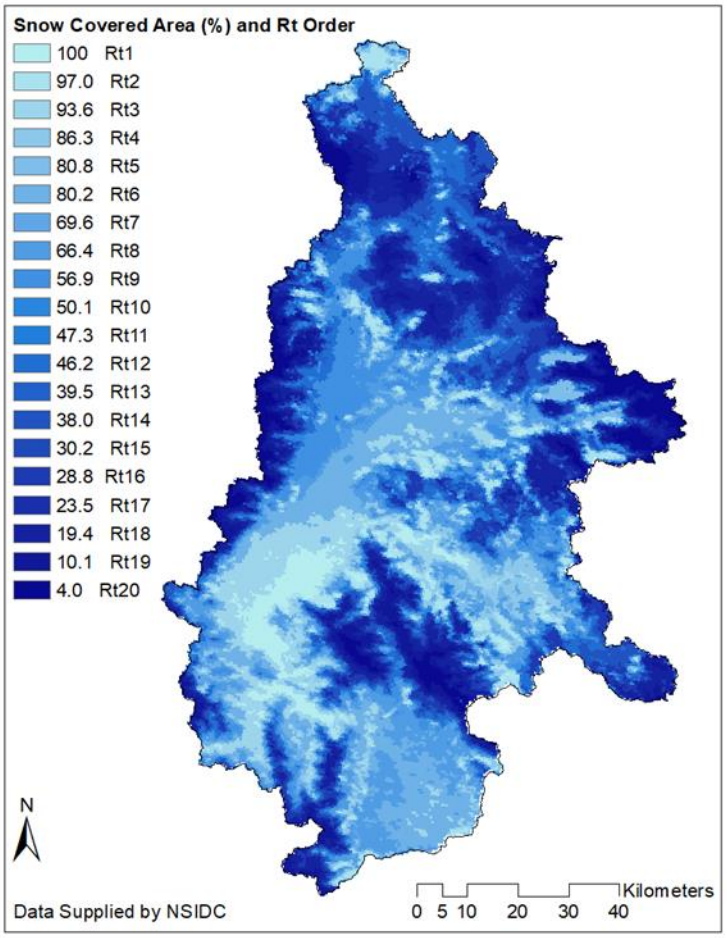

Figure 3.4: Cluster model of snow-covered area. Cluster melt timing is given by R_t ranging from 1-20. R_{t1} melts first and is given as the lightest blue, and R_{t20} melts last given as the darkest blue. To represent SCA r* is applied to categorize the R_t values into the binary snow or snow free. For an r* of 2 R_{t1} and R_{t2} both would be considered snow free and R_{t3} through R_{t20} would be considered snow covered.

Accuracy Assessment

Woodruff & Qualls (2019) demonstrated the recurrent pattern accurately models SCA independent of the timing of melt. We hypothesize the K-means clustering method can also capture the recurrent pattern and accurately describe SCA, and that the K-means clustering model will closely approximate the Woodruff & Qualls (2019) PCA model. To validate this hypothesis, we used clear day imagery (≤ 5% by area cloud cover) from 2017 and 2018 to calculate the spatial accuracy. Equation 3.2 is used to calculate the VPE for each selection of r* against the clear day image. The r* which produces the minimum VPE is the best fit SCA. With r* optimized we calculate the spatial accuracy with respect to the observed image by equation 3.3. Because the cluster model is a discrete representation of SCA we also directly compare the numerical values of the cluster model SCA and the observed SCA.

Table 3.2 describes the model performance for all the cloud free images during the melt seasons of 2017 and 2018. Throughout the melting seasons we see an average spatial accuracy of 92.5 and 92.2% for 2017 and 2018, respectively. Spatial accuracy in 2017 ranged from 84.5-97.1%. In 2018 the range was 85.6-96.6%. Overall, spatial accuracy of greater than 90% was recorded for SCA ranges from 0-50% SCA and 79-100%. The SCA range of 51-78% SCA recorded accuracies between 84.5-90%. The lowest VPE was not always found at the closest discrete cluster model SCA when compared with the observed SCA. For example, on day 103 in 2017 (Table 3.2 bold) the cluster model chose 86.3% SCA, but the actual SCA was 79.3% SCA. The closest cluster model representation is 80.2% SCA. The minimum VPE did not select the closest SCA representation as the best fit r*. The cluster model only chose the closest SCA 66.6% of the time. This mismatch occurred more regularly at higher SCA. This is an important distinction between the Cluster model and the PCA model produced by Woodruff & Qualls (2019). The spatial accuracy of the cluster model (92.2% and 92.5%) is like the PCA model (91.3% and 92.5%) for 2017 and 2018, respectively. The PCA model produces these high accuracies while also choosing the correct SCA (within +/- 2%) 89% of the time.

Table 3.2: Cluster Model clear day spatial accuracy 2017-2018. Day of year of the image, observed SCA, Cluster model SCA chosen, and spatial accuracy are given.

2017				2018			
DOY	SCA	Cluster model SCA	Spatial accuracy	DOY	SCA	Cluster model SCA	Spatial accuracy
83	96	93.6	94.9%	111	85.9	86.3	90.6%
103	**79.3**	**86.3**	**92.2%**	116	78	86.3	85.6%
124	73.1	69.6	86.1%	117	66.8	69.6	88.0%
125	70.9	69.6	86.6%	145	28.3	30.2	93.4%
130	55.6	56.9	88.8%	153	23	19.4	93.2%
131	60.8	56.9	84.5%	154	18	19.4	94.3%
151	34.9	38	91.0%	163	9.2	10.1	96.6%
156	28.9	30.2	92.0%	164	10.9	10.1	96.2%
158	24.4	23.5	91.9%				
170	14.5	19.4	93.1%				
173	12.5	10.1	95.7%				
174	10.1	10.1	96.6%				
176	8.8	10.1	96.5%				
177	10.2	10.1	96.3%				
181	5.7	4	97.1%				
182	6.5	4	96.3%				
Average			92.5%				92.2%

The spatial accuracy of the Cluster model varies with SCA but maintains high accuracy when applied to independent data. The model was not compared with any data from 2000-2016 as it was used to calculate the model. The high clear day spatial accuracy shows a recurrent pattern can be extracted using K-means clustering and is robust when compared to independent data.

Comparison of Cluster and PCA Models

The Cluster model can be used to model snow covered area as it changes throughout any snow year. The PCA method proposed by Woodruff & Qualls (2019) also achieves this. A significant difference between the Cluster and PCA approaches warrants comparison. The PCA approach discards PC2-17, about 15% of the total variance which was argued to contain cloud influence. Even with the discarded information the PCA model was accurate against independent data. The Cluster approach does not discard information. If our hypothesis that the Cluster model extracts the recurrent pattern is correct, then the PCA and Cluster models should be identical even though the PCA discards information. We compare the models by treating each Cluster model SCA as a clear day image and

using equation 3.2 to fit the PCA model to it. The grouping of R_t in the cluster model and selection of r* should coincide with the t* threshold, or the relative timing of melt, used in the PCA model discussed in Woodruff & Qualls (2019).

We calculate two measures of similarity between the models. The spatial accuracy of the comparison of the PCA and Cluster models, and the accuracy of the SCA chosen by the PCA model when it is fit to the Cluster model. Table 3.3 presents the Cluster model SCA, the fitted PCA model SCA, the calculated VPE, and the spatial accuracy of the fit. The PCA model chose a nearly perfect SCA representation every time apart from one which differed by more than 1% SCA (Cluster model SCA of 80.79%). The PCA model and Cluster model therefore represent similar spatial coverages of snow throughout the melting season.

Table 3.3: Comparison of the Cluster and PCA models. Spatial accuracy, VPE, and SCA chosen are all shown.

Cluster model SCA percent	*PCA model SCA percent chosen*	*VPE*	*Spatial accuracy*
96.96	97	0.012	98.27
93.60	94	0.019	97.37
86.30	86	0.022	96.92
80.79	82	0.037	94.91
80.13	81	0.038	94.65
69.54	70	0.026	96.37
66.38	67	0.038	94.65
56.90	57	0.019	97.34
50.06	49	0.033	95.39
47.28	47	0.022	96.90
46.19	47	0.025	96.51
39.51	39	0.025	96.51
37.95	38	0.021	97.00
30.23	30	0.026	96.38
28.80	29	0.025	96.50
23.52	23	0.034	95.28
19.39	19	0.016	97.78
10.18	10	0.008	98.88
4.21	4	0.005	99.30

The VPE of the PCA model fitted to the Cluster model at all SCA values is exceptionally low. The lowest VPE, or best fit, is achieved at the Cluster model's 4.21 SCA with a value of 0.005.

None of the VPE values exceed 0.038. This is also reflected in the spatial accuracy which is uniformly high. The highest spatial accuracy of 99.3% is achieved at the Cluster SCA of 4.21. Average spatial accuracy is 96.7% across all SCA values. The lowest reported accuracy is 94.6% at the Cluster model's SCA of 69.54%. The recurrent pattern is captured by both methods even though the PCA discards 15% of the variance in the dataset. The same dataset was used however the methods for calculating the models are mathematically different, as discussed later.

The spatial distribution of the disagreement between the PCA and Cluster models is shown. If the areas of disagreement are constrained to a single area there may be a significant difference between the two models. The ideal distribution of errors would be randomly dispersed about the snow to no snow line. Figure 3.5 presents where the models differed between the PCA 70% SCA representation and the Cluster model 69.54% SCA. The left image shows all the pixels that were not equal. The blue indicates where the Cluster model indicated snow, but the PCA model indicated land, and red shows the opposite scenario. On the left these errors look randomly distributed throughout the watershed, however when we impose the PCA 70% SCA snowline the errors follow the snowline. The difference between the two models is a slight shift in the snow to no snow interface. This distribution of errors was noted at other SCA comparisons as well, which are not shown. The differences between the models are minimal and are distributed in close proximity to the snow to no snow interface demonstrating the robust nature of the recurrent pattern of snowmelt.

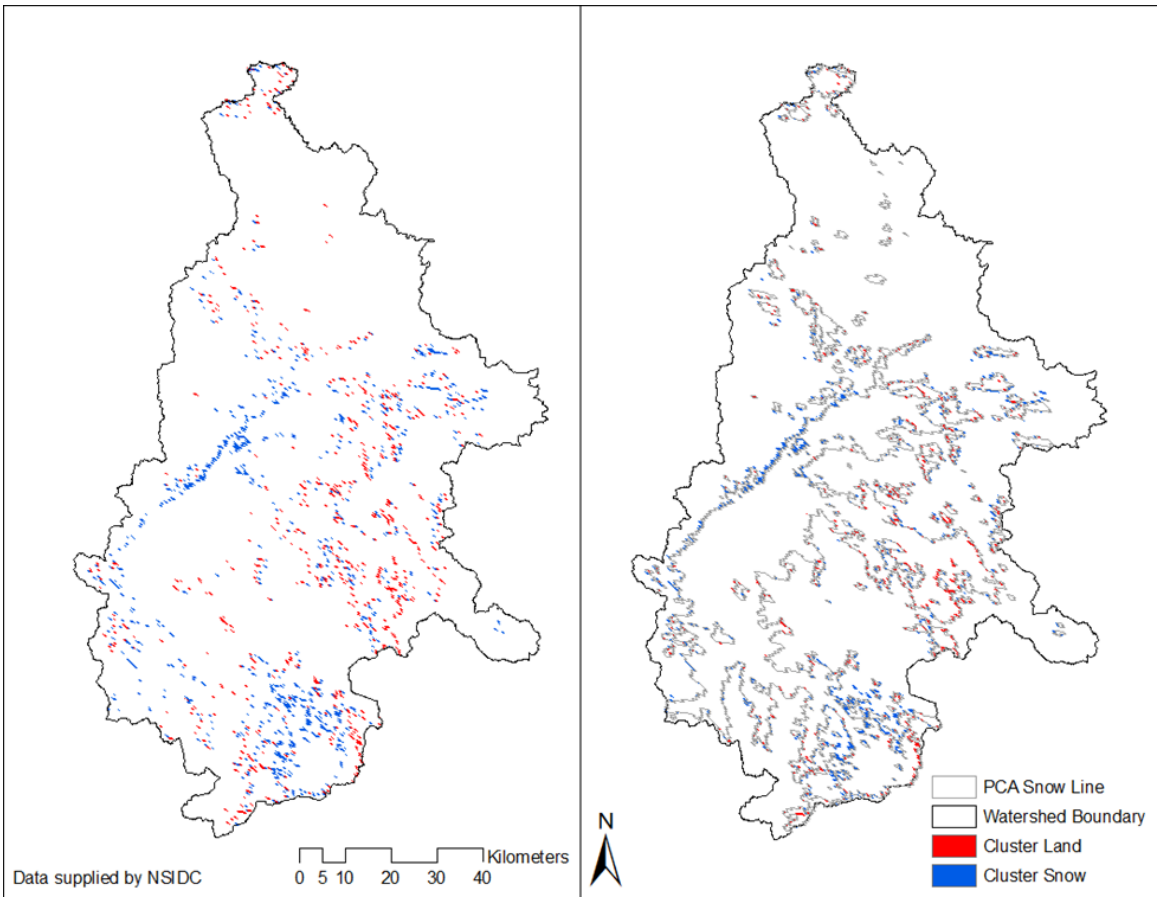

Figure 3.5: Spatial differences between PCA and Cluster model at 70% SCA. Blue indicates locations the Cluster model models snow but the PCA modeled land. Red shows where the Cluster model models land but the PCA modeled snow. For reference the PCA snowline is imposed over the right image.

Cloud Removal Comparison of the Cluster and PCA Models

Cloud removal was completed for the melt period of 2018 to compare the PCA and Cluster models. The VPE (equation 3.2) is calculated based on the visible pixels which allows us to select the cloud removed SCA for both models. This method replicates the cloud removal completed in Woodruff & Qualls (2019) for the PCA model. Clouds were removed from all the 2018 imagery between DOY 100-165. This is the period where bulk of melt occurs. Cloud cover was removed for any day where at least some portion of the watershed was visible. Figure 3.6 presents the results from the cloud removal.

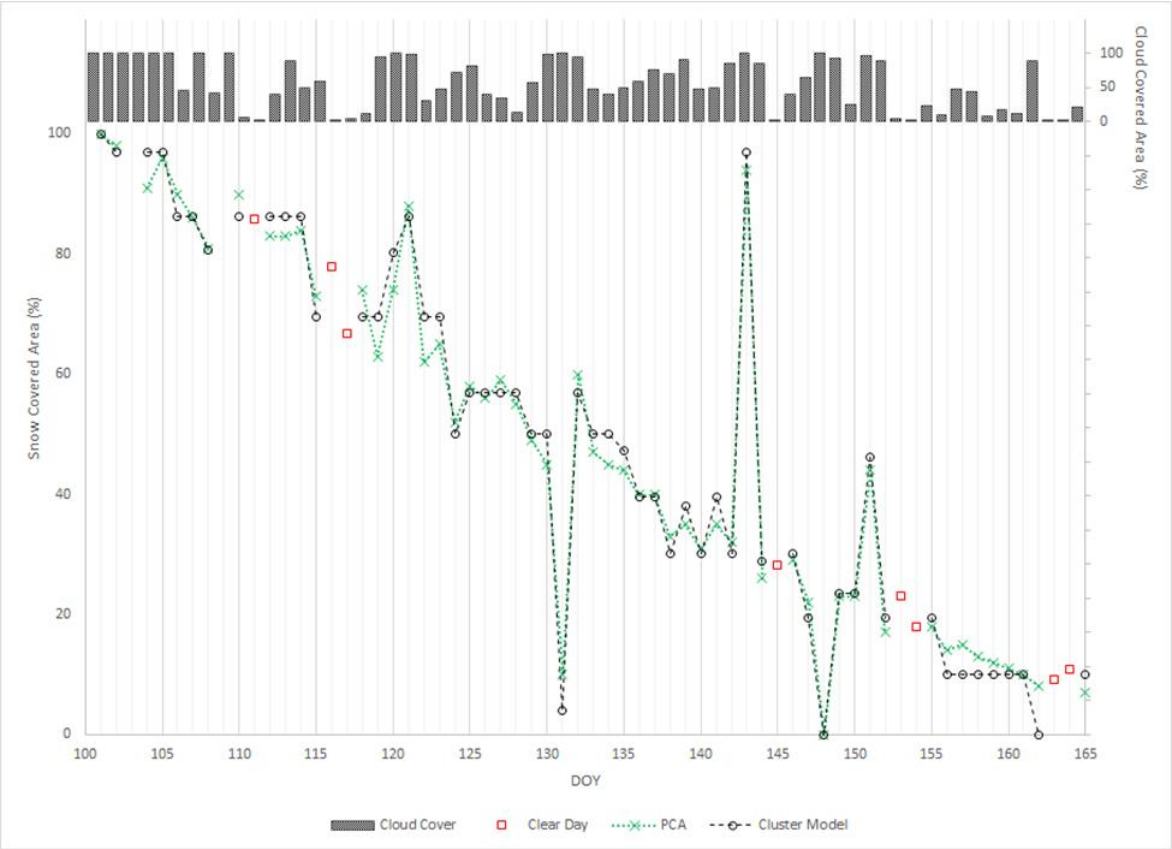

Figure 3.6: Cloud removal of daily imagery through 2018 melt period. 100% cloud cover days were omitted, and cloud free days were used as verification. Cloud cover is shown as a bar graph on the secondary y axis and SCA on the primary y axis. PCA cloud removal results (green "X" with dotted line) and Cluster cloud removal (hollow circle with dashed line) and cloud free days are indicated by the hollow red squares.

For this direct model comparison cloud cover was removed one day at a time. No information about snow coverage from either the previous or subsequent days was used to inform the cloud removal process. SCA was selected purely by the minimization of equation 3.2. In Figure 3.6, two sets of points and lines are shown. The PCA model cloud removed values are shown by the dotted line and "X", while the Cluster model cloud removed values are shown by the dashed line and hollow circles. The cloud free days where no cloud removal was necessary (red squares) are also shown. In both cases the models accurately represent the reduction in SCA with time and closely follow the time series of cloud free days. Both models chose the same or nearly the same SCA. Since the PCA model can represent SCA changes at 1% intervals we see a more linear decline especially between DOY 133-137 and 156-162. Some of the cloud removed days estimated unrealistic SCAs by both models, such as DOY 131 and 143. If we refer to the cloud cover percentage in Figure 3.6, both days had cloud coverage of nearly 100%. Despite the few erroneous SCA estimates, both models produced cloud removed image time series that resemble a cumulative snow depletion curve. This type of curve

is often used as input for snowmelt models such as the Snowmelt Runoff Model (SRM) developed by Martinec & Rango (1986).

In the 65-day period of melt only six days stand out as potential errors, days 120, 121, 131, 143, 148, and 151. Cloud coverage on these days was 99.9, 97.6, 99.9, 99.8, 99.5, and 97.2, respectively. A quick look at the SNOTEL site Base Camp also shows an increase in SWE between DOY 120 to 121. Due to this, we can say the measurement on DOY 121 may be correct. This shows that the models performed well except when cloud cover exceeded 99% of the image. In the cases of DOY 131 and 148 only land pixels were visible and for DOY 143 only snow pixels. No portion of the interface between land and snow was visible. Both models perform best when some portion of the interface is visible.

The recurrent pattern of melt produces a signal strong enough that multiple methods can extract it. A multi-year combination of remote sensing data is required to effectively handle the issue of cloud interference and develop the models. The single application of cloud removal is secondary to the potential of a spatial model of this kind. Both methods, PCA and Cluster, represent the spatial information of snow independent of the highly variable timing, depth, and duration of melt. Unlike other methodologies of cloud removal, which have a main purpose of infilling missing data, the recurrent pattern approach derives a characteristic variable of snowmelt that has applications in cloud removal. We are scratching the surface of potential applications of this new type of model.

Discussion

Implications of Similarity Between Cluster and PCA Models

The cluster model accurately models snow covered area when compared to independent data (2017 and 2018). Spatial accuracy when compared to cloud free imagery ranges from 84.5-97.1%. One other model exists which uses a multi-year method to create a model of the recurrent pattern of snow-covered area, the PCA method by Woodruff & Qualls (2019). When these models are compared directly, they exhibit remarkably similar representations of SCA throughout the melting season as shown by the high degree of accuracy (average 96.7%) from one model to the other. Both models also remove cloud cover by utilizing the recurrent pattern with comparable results (Figure 3.6). Two significant points about these models are, they are mathematically different methods and produce nearly equal results, and they both propose a different approach to cloud removal than current methods.

Both methods, PCA and K-means Clustering, were applied to the same dataset for the same period 2000-2016. If these methods conceptually and mathematically derived the output in the same way, there would be no need for comparison. The Cluster analysis is conceptually different than PCA as it is the only multivariate technique which does not estimate the variate (Grimm & Yarnold, 2000). A cluster analysis is exploratory in nature and lacks the statistical basis on which to draw statistical inferences. It determines the partitioning of a dataset or the natural grouping. PCA estimates the variate seeking to identify a direction that exhibits the greatest amount of variance of the dataset. These directions are orthogonal vectors known as eigenvectors. Because PCA estimates the variate, Woodruff & Qualls (2019) used a threshold method for determining SCA. In the cluster analysis only the discrete clusters were used. The natural groupings were compared against cloud free imagery.

The mathematical difference between PCA and K-means Clustering is in how variance is used and treated. Principal Component Analysis uses the covariance matrix of a dataset to derive the eigenvectors and values. Eigen values decrease in size, and one exists for each column in a matrix (17 in this case, corresponding to the number of years included in the dataset used in the analysis). Each Eigenvalue has an associated Eigenvector which describes a direction, and each pair is referred to as a principal component (PC). Each eigenvector is orthogonal to all others. The first Eigenvector direction (principal component one or PC1) describes the greatest amount of variance in the dataset, the second the second most and the last the least most. When combined all the eigenvectors describe 100% of the dataset's variance. Woodruff & Qualls (2019) use this concept on the dataset describing 85% of the variance in PC1. They then multiply the original dataset, a matrix of dimensions 41503 X 17, by the eigenvector describing PC1, a vector of dimensions 17 X 1. The result is a single vector which they then plot with x, y information to produce the final model. A matrix multiplication is used to produce the model which is linear in nature. Cluster analysis seeks only to partition the dataset into groups. Referring to equation 3.1 we see how this is done. Centroids R_t are chosen, and each point is assigned to a centroid based on their Euclidean distance. The WGSS measures which cluster grouping is best. This term is a sum of the error, or squared distance from each point to its cluster's centroid for each cluster. Variance within a cluster is the fundamental idea behind the WGSS. Unlike the PCA which estimates or tries to describe the variance with vectors and linear transformations, the cluster analysis uses the variance within a cluster to partition the data which is a nonlinear description. One method seeks to model variance while the other uses variance as a means for dividing the dataset.

How each method arrives at its result differs, but a more significant point about the methods remains. Woodruff & Qualls (2019) argue only PC1 is needed, and the subsequent PCs (2-17) contain

cloud contamination. This is shown by the correlation between the PC1 values produced using the FDL and LDS datasets, which allows them to discard 15% of the variance in the dataset. It is impossible to discard information using a K-means Cluster Analysis. If any portion of the recurrent pattern were described by the 15% of variance discarded by Woodruff & Qualls (2019) then the spatial accuracy of the Cluster model would exceed the PCA. Spatial accuracy of the Cluster model ranged from 84.5-97.1%, which is slightly lower than the 84.9-97.5% spatial accuracy for the PCA model. The PCA model selects the nearest correct SCA (within +/- 2%) 89% of the time, while the Cluster model does so only 66.6% of the time. This demonstrates the "loss of data" due to discarding PC2-PC17 with the PCA method increases the spatial accuracy of the recurrent pattern of melt. The increase is directly a result of excluding cloud contamination held in the FDL and LDS images.

Distinction Between Recurrent Pattern Cloud Removal and Current Methods

The value of these models is their ability to spatially represent snow covered area independent of snow depth, melt duration, and melt initiation. Cloud removal is a single application of the repeatable pattern. The current cloud removal technologies face three issues. One, the cloud removal methods record their lowest accuracies during the transitional melt period. Two, the current technologies which achieve 100% cloud removal rely heavily on multiple data sources including ground-based data. Three, current methods use intricate interpolation schemes which produce highly dependent cloud free images that may not be suited to extreme drought or flood years.

The Cluster and PCA model both are designed specifically to remove cloud cover during the melting period. For operational snowmelt modeling this is the period of greatest importance. The MODSNOW-tool developed by Gafurov et al. (2016) boasts cloud removal on days with 100% cloud cover. They found accuracies between 77.3-99.8% when removing imposed cloud cover over cloud free days (≤10% cloud cover) in the Karadarya basin for an 84-day period. The lowest accuracy of 77.3% was recorded during the melting season. In contrast both the PCA and Cluster model found a minimum spatial accuracy of nearly 85%. We should also note our method for calculating accuracy is far more stringent as we count incorrectly modeled "snow covered" pixel as an error rather than just infilling the cloud covered pixels. Our model is built with operational snowmelt modeling in mind while other methods are more suited to long term monitoring of snow extent.

Current cloud removal methods rely on multiple data sources while the Cluster and PCA methods require only remote sensing from one sensor to remove cloud cover. Dong & Menzel (2016) expanded on the MODSNOW-tool to increase the accuracy of rejecting misclassified pixels using meteorological data and interpolations of ground-based data, a total of three types of ground-based

measurements were required. Using ground –based data to quantify their accuracy they achieved spatial accuracies of 87-92% where 87% was recorded during the melt period. Even the Adaptive Spatio-Temporal Weighted Model (ASTWM) developed by Li et al. (2017), requires precipitation and temperature data to employ their step-by-step cloud removal protocol. Li et al. (2017) recorded remarkably high spatial accuracies of 93.11-98.92% accuracy when removing 100% imposed cloud cover. Relying on multiple data sources requires high quality data that is routinely available. It is very unlikely these approaches would record the same high accuracy in an ungauged watershed, where using the recurrent pattern approach either through the Cluster model or PCA model would not falter.

Each of these cloud removal methods uses at least one step that infills cloud covered pixels from previous or subsequent day imagery. Given a scenario where a pixel is viewed as snow covered and is covered by cloud for 15 days and seen as snow free on the 16th day the above infilling method would produce a "best guess" as to when the pixel melted. Referring to Figure 3.6, between days 120 and 135 there is a 25% reduction in snow covered area. Equally important is this data once infilled is dependent on the quality of data used to infill. Cloud cover removed using the Cluster model uses only the pixels in the cloudy image, meaning each cloud removed image is independent of influence from data on other days. This issue has been addressed in current methods with a conditional probability of snow cover. One conditional probability built into the MODSNOW-tool is the monthly probability of snow cover for a pixel. This works fine for average snow years; however, the drought and flood years which have the highest stakes for water management do not behave like average snow years. In contrast the Cluster model and PCA models shift effortlessly with varied timing in melt because they are related to the spatial progression of melt. In fact, the test period used to develop the Cluster model contained a wide variety of snow conditions. As shown in Table 3.1, the melt timing and snow depth was extremely variable for the years used to develop the model, and during the validation period of 2017 and 2018. Where other cloud removal technologies may struggle during extreme snow years, both large and small snowpacks, our method records no loss in accuracy.

While reduced accuracy during the melting season is a significant issue, the reliance of cloud removal methods on multiple data sources makes these methods error prone in ungauged watersheds. The multi-step methods such as MODSNOW-tool and the probability approach by Dong & Menzel (2016) incorporate ground-based data to remove cloud cover and increase the accuracy of the cloud removal by rejecting misclassified pixels. The quality of cloud removal is thus hindered by the availability of data. The same is true for the ASTWM model by Li et al. (2017). The ASTWM model uses spatial and temporal probability of snow. The temporal probability is based on a 15-day time

series of images so if any images are missing from the period confidence may be reduced. The fundamental difference between these methods and the Cluster and PCA models is they seek to infill a cloudy pixel based on information from temporal and spatial combinations. The Cluster and PCA methods model snow covered area and cloud removal is a product of identifying where in the spatial progression of melt the watershed is.

Limitations

The Cluster model is developed using raw MODIS imagery and cloud removal is achieved with only the visible pixels in a cloudy image. Applications of this model are limited by data quality and the user identified parameters used to derive the FDL imagery. We applied a constant threshold to classify pixels as snow versus snow free. During the FDL data preparation stage the NDSI snow cover threshold becomes important as it determines the DOY of melt to be used to combine the data. As seen in Figure 3.2 early detection of melt shows up as dark areas surrounded by light areas. It is unlikely this representation of melt is correct and is the general location of persistent errors. Viewing angle, illumination, land cover and other factors all influence the NDSI (Rittger et al., 2013). Misclassified pixels may also be a source of error during the data preparation step leading to misrepresentative information in the FDL. In cloud removal application misclassified pixels may cause the model to select an incorrect SCA. For this to happen there must be a considerable number of misclassified pixels along the interface which would shift the model to choosing an incorrect interface, however this is unlikely.

The second limitation of this model is some pixels must be visible to remove cloud cover. An image with 100% cloud cover offers no spatial information for determining the SCA. The model accuracy is also related to the interface which is visible. If no portion of the snow-to-snow free interface is visible confidence in the model's ability to select the correct SCA is decreased. This can be seen in Figure 3.6 on DOY 131, 143, 148, and 151. In these cases, little to none of the interface was visible. The Cluster model also has a non-uniform representation of SCA which can cause it to choose an incorrect SCA as shown by the comparison of the PCA and cluster method (Comparison of Cluster and PCA section).

Conclusions

Hydrologic modeling of snow can be aided by watershed characteristics such as the recurrent pattern of melt. We propose a method to derive the recurrent pattern of melt and verify it against a different statistical approach. The Cluster model accurately represents snow covered area changes throughout two melting season 2017 and 2018 acquiring spatial accuracies of 84.6-96.0% when

compared against cloud free days. The model also showed the ability to remove cloud cover for each day during the melt period of 2018 tracking closely the timing of melt, Figure 3.6. Cloud removal is a single application of this model and is used here as a method for comparing the PCA and Cluster models. The benefits of using a recurrent pattern approach to cloud removal is it does not rely on ground-based data, temporal interpolations, and it readily handles the variable timing of snowmelt. These issues are persistent setbacks to the current cloud removal methods. The recurrent pattern of snowmelt has been noted in the literature for over 40 years (Adams, 1976), but has been an elusive component of snowmelt to capture.

Comparison of the Cluster method and the PCA method has demonstrated there is ease of use with the PCA method, but the pattern is unchanged independent of how it is calculated. We also verified the discarding of data using the PCA method, which was argued to be attributed to cloud influence by Woodruff & Qualls (2019), increases the spatial accuracy of the captured recurrent pattern of melt. Further research is necessary into applications of the recurrent pattern of snowmelt; however, spatial information of snow-covered area can lead to increased accuracies in modeling streamflow, a benefit of using the model proposed here (Safari Shad et al. 2014; Qui et al. 2014). Potential applications could include boundary conditions for snow location, snowmelt timing information in ungauged watersheds, and potential relationships with snow covered area and streamflow in ungauged watersheds. The recurrent pattern of snowmelt identifies a watershed characteristic unique to each watershed which has never been captured. This information opens a new avenue for research questions.

References

Adams, W. P. (1976). Areal differentiation of snow cover in east central Ontario, Water Resources Research, 12(6), 1226– 1234, doi:10.1029/WR012i006p01226.

Barnett, T. P., Adams, J. C., & Lettenmaier, D. P. (2005). Potential impacts of a warming climate on water availability in snow-dominated regions. Nature, 438, 303-309.

Dickerson-Lange, S. E., & Mitchell, R. (2014). Modeling the effects of climate change projections on streamflow in the Nooksack River basin, Northwest Washington. Hydrological Processes, 28(20), 5236-5250. doi:10.1002/hyp.10012.

Dingman, S. L. (2008). Physical hydrology (2nd ed.). Long Grove, Ill.: Waveland Press Inc.

Dong, C., & Menzel, L. (2016). Producing cloud-free MODIS snow cover products with conditional probability interpolation and meteorological data. Remote Sensing of Environment, 186, 439.

Everitt, B. & Hothorn, T. (2011). An introduction to applied multivariate analysis with R, New York: Springer.

Gafurov, A., Lüdtke, S., Unger-Shayesteh, K., Vorogushyn, S., Schöne, T., Schmidt, S., Kalashnikova, O., & Merz, B. (2016). MODSNOW-Tool: An operational tool for daily snow cover monitoring using MODIS data. Environmental Earth Sciences, 75(14), 1-15. doi:10.1007/s12665-016-5869-x.

Grimm, L., & Yarnold, Paul R. (2000). Reading and understanding more multivariate statistics (1st ed.). Washington, DC: American Psychological Association.

Hall, D. K., & Riggs, G. A. (2007). Accuracy assessment of the MODIS snow products. Hydrological Processes, 21(12), 1534-1547. doi:10.1002/hyp.6715.

Hall, D.K. & Riggs, G. A. (2015). MODIS Snow Products Collection 6 User Guide. doi: http://nsidc.org/sites/nsidc.org/files/files/MODIS-snow-user-guide-C6.pdf. [July 12, 2018].

Hall, D. K. & Riggs, G. A. (2016). MODIS/Terra Snow Cover Daily L3 Global 500m Grid, Version 6. [NDSI snow cover]. Boulder, Colorado USA. NASA National Snow and Ice Data Center Distributed Active Archive Center. doi: https://doi.org/10.5067/MODIS/MOD10A1.006. [January 2017 - March 2018].

Hock, R. (2003). Temperature index melt modelling in mountain areas. Journal of Hydrology, 282(1), 104-115. doi:10.1016/S0022-1694(03)00257-9.

Homer, C.G., Dewitz, J.A., Yang, L., Jin, S., Danielson, P., Xian, G., Coulston, J., Herold, N.D., Wickham, J.D., & Megown, K., (2015), Completion of the 2011 National Land Cover Database for the conterminous United States-Representing a decade of land cover change information. Photogrammetric Engineering and Remote Sensing, v. 81, no. 5, p. 345-354.

König, M. & Sturm, M. (1998). Mapping snow distribution in the Alaskan Arctic using aerial photography and topographic relationships, Water Resour. Res., 34(12), 3471–3483, doi:10.1029/98WR02514.

Krajčí, P., Holko, L., Perdigão, R. A. P., & Parajka, J. (2014). Estimation of regional snowline elevation (RSLE) from MODIS images for seasonally snow covered mountain basins. Journal of Hydrology, 519(PB), 1769-1778. doi:10.1016/j.jhydrol.2014.08.064.

Li, X., Fu, W., Shen, H., Huang, C., & Zhang, L. (2017). Monitoring snow cover variability (2000–2014) in the Hengduan Mountains based on cloud-removed MODIS products with an adaptive spatio-temporal weighted method. Journal of Hydrology, 551, 314-327. doi:10.1016/j.jhydrol.2017.05.049.

Luce, C. H., & Tarboton, D. G. (2004). The application of depletion curves for parameterization of subgrid variability of snow. Hydrological Processes, 18(8), 1409-1422. doi:10.1002/hyp.1420.

Martinec, J. (1982). Runoff Modeling from Snow Covered Area. Geoscience and Remote Sensing, IEEE Transactions on, GE-20(3), 259-262. doi: 10.1109/TGRS.1982.350440

Martinec, J., & Rango, A. (1986). Parameter values for snowmelt runoff modelling. Journal of Hydrology, 84(3), pp.197–219. doi:10.1016/0022-1694(86)90123-X.

Painter, T. H., Rittger, K., Mckenzie, C., Slaughter, P., Davis, R. E., & Dozier, J. (2009). Retrieval of subpixel snow covered area, grain size, and albedo from MODIS. Remote Sensing of Environment, 113(4), 868-879. doi:10.1016/j.rse.2009.01.001.

Parajka, J., & Blöschl, G. (2008). Spatio-temporal combination of MODIS images – potential for snow cover mapping. Water Resources Research, 44(3), N/a. doi:10.1029/2007WR006204.

Parajka, J., Pepe, M., Rampini, A., Rossi, S., & Blöschl, G. (2010). A regional snow-line method for estimating snow cover from MODIS during cloud cover. Journal of Hydrology, 381(3), 203-212. doi:10.1016/j.jhydrol.2009.11.042.

Pierce, D., Cayan, D., Maurer, E., Abatzoglou, J., & Hegewisch, K. (2015). Improved Bias Correction Techniques for Hydrological Simulations of Climate Change. Journal of Hydrometeorology, 16(6), 2421-2442. doi:10.1175/JHM-D-14-0236.1.

Qiu, L., You, J., Qiao, F., & Peng, D. (2014). Simulation of snowmelt runoff in ungauged basins based on MODIS: A case study in the Lhasa River basin. Stochastic Environmental Research and Risk Assessment, 28(6), 1577-1585. doi:10.1007/s00477-013-0837-4.

Qualls, R. J., Taylor, R. G., Hamilton, J., & Arogundade, A. B. (2013). Climate change opportunities for Idaho's irrigation supply and deliveries. Journal of Natural Resources Policy Research, 5(2-3), 91-105, DOI: 10.1080/19390459.2013.811856.

Riggs, G.A., Hall, D. K., & Roman, M. O. (2017). Overview of NASA's MODIS and Visible Infrared Imaging Radiometer Suite (VIIRS) snow-cover Earth System Data Records. Earth System Science Data, 9(2), pp.765–777. doi:10.5194/essd-9-765-2017.

Rittger, K., Painter, T. H., & Dozier, J. (2013). Assessment of methods for mapping snow cover from MODIS. Advances in Water Resources, 51(C), 367-380. doi:10.1016/j.advwatres.2012.03.002.

Safari Shad, M., Habibnejad Roshan, M., & Ildoromi, A. (2014). Integration of the MODIS Snow Cover Produced Into Snowmelt Runoff Modeling. Journal of the Indian Society of Remote Sensing, 42(1), 107-117. doi:10.1007/s12524-013-0279-y.

Steele, C., Dialesandro, J., James, D., Elias, E., Rango, A., & Bleiweiss, M. (2017). Evaluating MODIS snow products for modelling snowmelt runoff: Case study of the Rio Grande headwaters. International Journal of Applied Earth Observations and Geoinformation, 63, 234-243. doi:10.1016/j.jag.2017.08.007.

Stewart, I., Cayan, T., & Dettinger, D. (2004). Changes in Snowmelt Runoff Timing in Western North America under a `Business as Usual' Climate Change Scenario. Climatic Change, 62(1), 217-232. doi:10.1023/B:CLIM.0000013702.22656.e8.

Sturm, M., & Wagner, A. (2010). Using repeated patterns in snow distribution modeling: An Arctic example. Water Resources Research, 46(12), N/a. doi:10.1029/2010WR009434.

Wood, A., Leung, L., Sridhar, V., & Lettenmaier, D. (2004). Hydrologic Implications of Dynamical and Statistical Approaches to Downscaling Climate Model Outputs. Climatic Change, 62(1), 189-216. doi:10.1023/B:CLIM.0000013685.99609.9e.

Woodruff, C. D., & Qualls, R. J. (2019). Recurrent snowmelt pattern synthesis using principal component analysis of multiyear remotely sensed snow cover. Water Resources Research, 55. https://doi.org/10.1029/2018WR024546\

Chapter 4: Sensitivity of the Pattern Based Approach to Snowmelt Modeling using the Inter-Annual Recurrent Pattern of Snowmelt to User Decisions

Introduction

Snowmelt is a vital source of fresh water in the around the world. It has been estimated that 50-80% of streamflow in the Western United States is attributed to snowmelt (Stewart et al., 2004). The changing climate affects this finite resource of snowmelt driven streamflow, which is projected to produce earlier and earlier peak streamflow (Barnett et al., 2005). Mote (2003) demonstrated the already changing snow characteristics as they relate to time across the Western United States for the period of 1950-2000. The more interpretable and data driven approaches we can develop the better we can manage water when it matters most such as in droughts. The spatio-temporal model of snow-covered area (SCA) depletion is an interpretable and data driven approach to snowmelt modelling. We investigate methods for increasing the spatial accuracy of the spatio-temporal model of SCA in this research.

The complex system of snowmelt requires accurate physical and/or empirical representation of the drivers of melt. In many model frameworks parameters are calibrated to simulate streamflow and tested against independent data. Regionalization is a method used to transfer parameters from one watershed to another based on watershed similarity (Bloschl & Sivapalan, 1995). The idea of watershed hydrologic similarity was first proposed by Wood & Hebson (1986) and has expanded into an area of significant research. Regionalization is a technique which allows us to classify watersheds based on their hydrologic similarity to better simulate streamflow in watersheds ungauged watersheds. Kanishka & Eldho (2020) used a similarity index and simulated streamflow to test a variety of regionalization or classification techniques for the transfer of fitted parameters for the SWAT model. They found that Isomaps and regionalization based on physical similarity were the best methods to classify watersheds as similar. We have gone to great lengths to find unifying characteristics that link watersheds. Effectively these techniques seek to adapt the parameters of a process so they are applicable in a new area. An important question remains about what parameters need to be fit. Newman et al. (2014) developed two approaches to represent subgrid variability in land surface models to transfer these subgrid values into the larger gridded models. The assumption here is the snowmelt model representativeness is a function of the physical characteristics which we are targeting through these models, a bottom up approach. Given this assumption we could suppose that the snowmelt should follow a spatial pattern determined by these parameters, because the model does

not have to change, a top down approach. This is a valuable point because the process of snowmelt can be represented spatially by a spatio-temporal model which captures the pattern (Woodruff & Qualls, 2019). The spatio-temporal model is an automatic parameterization of the snowmelt that is distinct and characteristic for the area in which it is developed. It is a data driven approach that is top down. These types of approaches have been implemented for other pattern analyses (example: Rice et al., 2016). This approach is cost saving because we do not have to parameterize the multitude of physical characteristics that are necessary to run these snowmelt models.

The spatio-temporal model of snowmelt does not negate the need for a snowmelt runoff model, but it does simplify accurately describing the spatial and temporal components of melt with only remote sensing. In comparison, the Snowmelt Runoff Model (Martinec & Rango, 1986) aggregates the spatial information into a snow depletion curve. This curve describes the rate of melt but not where it occurs. The Variable Infiltration Capacity model on the other hand represents the rate and location of snowmelt but verifies only against the depth of Snow Water Equivalent (SWE) as measured by point locations (Cherkauer & Lettenmaier, 2003). The data needed to run the VIC model is extensive. The spatial and temporal component captured and described by the (Principal Component Analysis) "PCA model" developed by Woodruff & Qualls (2019) are extremely valuable because it describes the 2-dimensional location and the timing of snowmelt. This information is exceptionally valuable to accurately modeling snowmelt runoff.

We live in a data rich world with the advent of Remote Sensing and interpolating data we can measure is in some cases redundant, unnecessary, and potentially biased. Shen (2018) overviewed the current state of hydrologic modelling and called for implementation of more Deep Learning and Artificial Neural Networks (ANN) for simulating streamflow because of the large amount of available data. Thapa et al., (2020) fit and tested four machine learning models to predict streamflow given hydrometeorological data and MODIS 8-day composites with less than 10% cloud cover over the Langtang Basin in the Central Himalayas. They compared a deep learning model known as the Long Short-Term Memory (LSTM) to a nonlinear autoregressive exogenous model, Gaussian process regression model, and a support vector regression model. The LSTM model outperformed all others with a Nash-Sutcliffe model efficiency of 99.5% and a RMSE of 0.201. A secondary interesting finding by Thapa et al. (2020) was that when the MODIS data was removed the model RMSE increased to 0.287 and when precipitation was not included as a predictor variable the RMSE dropped to 0.173 for the testing set of two independent years. This finding demonstrates the importance of snow location data to snowmelt runoff accuracy. It is clear machine learning, which includes ANN

and Deep Learning, is a useful model when accuracy is the only concern because they are data driven and less computationally expensive (Pham et al., 2021; Tolson & Shoemaker, 2007).

Deep Learning and ANN access patterns or characteristics that we fail to implement or accurately represent in our snowmelt runoff models. In comparison, a snowmelt runoff model requires data input interpreted and implemented according to an expert's knowledge to fit and calibrate the model. Conversely, an ANN takes the input data and develops high level learned features buried deep within weights of and hidden layers of the model (Flores, 2011) to simulate snowmelt runoff. Extracting and understanding this information is difficult. The benefit of the snowmelt runoff model is the ease of interpretation. Resistance within the hydrologic community to Deep learning and ANN methods is present because of interpretability (Shen 2018). A pattern of behavior is the most useful piece of information because it simplifies the problem, but these are difficult to identify with these higher order models. We propose the spatio-temporal PCA model of the recurrent pattern of snowmelt is a higher order pattern which Deep learning and ANN access that can be interpreted and extracted for use in a snowmelt runoff model such as VIC or SRM.

In this work we focus on the recurrent pattern of snowmelt. This pattern is robust and can be derived into a spatio-temporal model of snowmelt that is spatially recurrent (Woodruff & Qualls, 2019) as well as temporally recurrent (Woodruff & Qualls 2021?). Snow covered area (SCA) measured by the Moderate Resolution Imaging Spectroradiometer (MODIS) is used to derive the PCA model over a given watershed. As discussed above, we desire patterns because they simplify the modeling of seemingly stochastic processes. Remotely sensed SCA from MODIS is available worldwide and as stated above the PCA model is a watershed characteristic intrinsic to each watershed, a form of parameterization of the snowmelt process. Because of the wide availability of these data this can be accomplished for any snowmelt driven watershed.

Spatial patterns of snowmelt have been identified and accepted in the literature for many years across a number of landscapes (Adams, 1976; König & Sturm, 1998; Luce & Tarboton, 2004; Sturm & Wagner, 2010; Wang & Xei, 2009; Parr et al., 2020). Spatial patterns in snow depth (Pflug & Lundquist, 2020), SCA, and snow redistribution (Parr et al., 2020) have all been identified. We focus specifically on SCA in this research because it is widely available and has been demonstrated to be spatially accurate against independent data. The purpose of this work is to extract the best recurrent pattern of snowmelt using the methods outlined in Woodruff & Qualls (2019). In their work they applied the pattern for cloud gap filling, but they commented on areas within their model which were error prone. We hypothesize altering a user decision in the PCA model derivation may eliminate

these spurious errors. These errors are likely a function of scan angle, topography, illumination, and vegetation of the MODIS pixel (Riggs et al., 2017). The MODIS sensor has demonstrated 93% spatial accuracy by ground truth on clear days (Hall & Riggs, 2007); however, many of the observations of SCA occur on cloudy days. This uncertainty propagates through into the PCA model leading to decreased spatial accuracy of their model on clear days specifically at larger SCA percentages. Addressing these issues will increase the published spatial accuracies of 84.9-97.5% by producing a model that is closer to the *true recurrent pattern* of snowmelt and free of spurious errors.

The implications of an accurate and recurrent spatio-temporal model of snowmelt cannot be overstated. A model of this type provides what watershed similarity seeks to accomplish. The spatial information can be derived for any watershed because remote sensing is available, and the model is scalable with time. It contains spatial and temporal predictive qualities making it applicable in any melt period. The pattern allows us to simplify the stochastic across years and complex system of snowmelt. This model is a watershed characteristic and should be viewed in the same way we view topography. No calibration is necessary as it is a data driven approach.

Study Site and Data

Study Site

The Upper Snake River Basin is a large watershed covering 8,894 square kilometers and is the headwaters for many stakeholders downstream (Figure 4.1). It is an important water resource for agriculture, power generation, municipal water demands, and in-stream fish requirements (Qualls et al., 2013). A wide variety of land cover types are present in the watershed including sage steppe (45.4% of the total area) and forested (47.9% of the total area) according to the 2015 National Land Cover Database (Homer et al., 2015). The watershed has a large range in elevation from 1,737 to 4,194 meters above mean sea level. In every year during the study period (2000-2020) the watershed recorded seasonal coverage of snow from 100% covered to completely snow free. In-stream flow rates are dependent on snowmelt making this study site ideal for seasonal snow monitoring.

Data

The Moderate Resolution Imaging Spectroradiometer (MODIS) records a number of snow characteristics on board two satellites (terra and aqua) on a daily time-step at a spatial resolution of 500 meters. The daily acquisition and data record extending from 2000 to the present make this dataset ideal for developing spatio-temporal models of snowmelt. The product we use is the version 6 MOD10A1 NDSI snow cover product. This is the daily Normalized Difference Snow Index (NDSI) dataset. Recently, a cloud gap filled dataset has been produced by NASA and is distributed by the

NSIDC DAAC (Hall et al., 2019). Our process extracts information from the daily data so there is no need to use the cloud gap filled dataset. The recurrent pattern can be captured by a single satellite as shown by Woodruff & Qualls (2019). The Terra satellite MODIS product is preferred because the Aqua satellite sensor had a failure in band 6, a crucial band for the NDSI calculation, and even though the algorithm has been adapted, the Aqua satellite still records more snow commission errors than the Terra satellite (Hall et al., 2019). All available daily MODIS images were downloaded for the period of 2000-2020. The data record is split into a model development subset (2000-2016) and a validation subset (2017-2020).

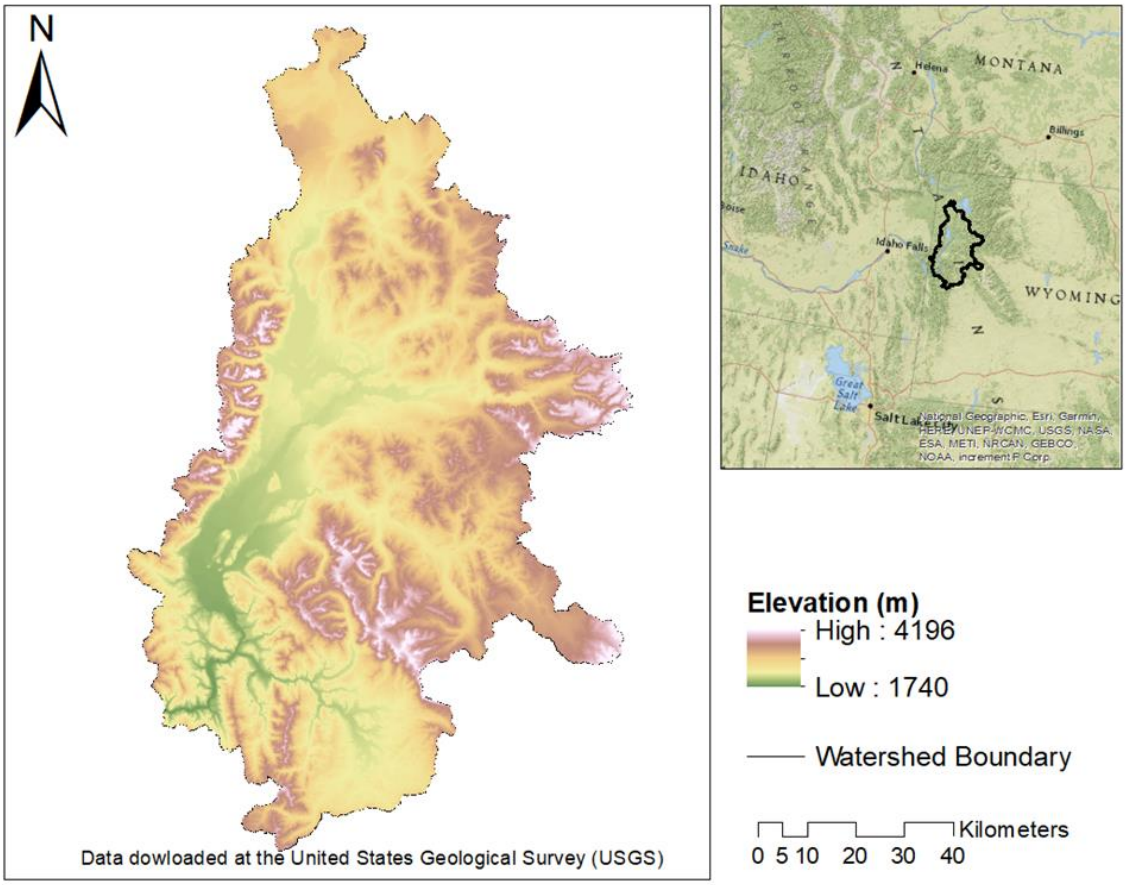

Figure 4.1: Elevation and location of the Upper Snake River Basin.

Methods

Data Preparation

Remote sensing offers spatially distributed daily data. The MODIS data is unfortunately contaminated with cloud cover. This reduces the available amount of data and makes working with it difficult. The recurrent pattern of snowmelt is contained in this dataset; however, to extract it data

preparation is required. The data preparation helps to address two problems. One, cloud contamination and two, a substantial amount of redundant information exists. A pixel that is snow covered for 100 continuous days contains 99 redundant days if we are interested only in the date it melts. To reduce the amount of redundancy, we iterate through all the available data and record two dates for each pixel. The last day snow is recorded (LDS) and the first day land is recorded (FDL) together describe the timing of melt. If cloud cover did not contaminate the data, the FDL would be exactly 1 day larger than the LDS.

An important consideration in extracting the FDL and LDS is ephemeral snowfall. If a pixel melts and subsequently recovered by snow it is difficult to determine whether the first melt or the second melt is captured by the FDL and LDS. If the ephemeral snowfall events are captured in the FDL and LDS then this could potentially propagate into the final model. In the model these errors would be incorrect early detection of melt. These types of events are stochastic, and in terms of model development they are generally discarded by using multiple years.

Deriving the PCA_c Models

The NDSI snow cover product gives a percentage of a pixel's snow coverage between 0 and 100%, we denote the snow coverage percent as "*c*". On clear days, this information may be valuable in determining the presence of snow across the whole area of interest; however, under low light conditions we may not record an accurate representation of snow coverage. Woodruff & Qualls (2019) used a single value of "*c*" to develop their PCA model and to convert the NDSI snow cover to a binary snow, or no snow image. They noted areas in their study site which were prone to snow detection errors. We propose altering the NDSI snow cover threshold, or "*c*", as a potential solution to these snow detection errors propagating into the PCA model. We hypothesize that a lower value of "*c*" could produce a higher quality model of the true recurrent pattern of melt.

Choosing a value of "*c*" to convert the NDSI snow cover to a binary snow and snow free image impacts the Last Day of Snow (*LDS*) and First Day of Land (*FDL*) images. We calculate the *FDL* and *LDS* for all the given imagery for 2000-2016 for a given value of "*c*". We also varied the values of "*c*" from 10 to 90 at intervals of 5. The range of "*c"* is based on the MODIS user guide. For continuity between the albedo and the NDSI snow cover product we considered values of less than 10 as snow free (Hall & Riggs, 2016). The selected value of "*c*" is given as a subscript. We have a pair of images, FDL_c and LDS_c, for all 17 years (34 in total) and 17 values of "*c*" for a total of 578 FDL_c and LDS_c images.

The FDL_c or LDS_c images can both be used to calculate the PCA_c model. It was demonstrated by Woodruff & Qualls (2019) that calculating the PCA model with the LDS images is 99.9% correlated to the PCA model found using the FDL images. This suggests the influence of cloud is discarded into Principal Components (PC) not used derive the model. In their case the recurrent pattern was captured completely by PC1. In this study we use the FDL_c images to calculate the PCA_c. The FDL_c values are found and transferred into a matrix, Equation 4.1. There are *M* columns, each for a melt period or FDL_c, and *N* rows, or pixels. Each pixel has an associated centroid of x and y coordinates. For row N_i, there are *M* FDL_c values that all have centroid coordinates of x_i *and* y_i. The PCA_c is applied to the *N* by *M* matrix and Principal Components are calculated. The PCA_c model is calculated by multiplying the *N* by *M* matrix by the vector "PC1". This matrix multiplication results in the PCA_c vector given as *t*. This vector is then reattached to the x and y coordinates and finally converted to a raster. The raster is equal in size and geolocation as the MODIS imagery and is referred to hereafter as the PCA_c model.

Equation 4.1

$$\begin{bmatrix} 1,1 & \cdots & 1,M \\ \vdots & \ddots & \vdots \\ N,1 & \cdots & N,M \end{bmatrix} * \begin{bmatrix} 1 \\ \vdots \\ M \end{bmatrix} = \begin{bmatrix} 1 \\ \vdots \\ N \end{bmatrix} \rightarrow \begin{bmatrix} t_1 & x_1 & y_1 \\ \vdots & \vdots & \vdots \\ t_N & x_N & y_N \end{bmatrix} \rightarrow PCA_c\ (Spatial\ Raster)$$

Comparing the PCA_c Models

The PCA statistical method calculates Eigen Values and Eigen Vectors commonly referred to as Principal Components (PC's). Each Principal Component is orthogonal to the rest and describes a portion of the total dataset variance. Cumulatively the PC's describe the total data variance. The Principal Components are ordered from 1 to *M*, where the first vector describes the largest portion of the total variance and the *Mth* vector describes the least. We use the variance to quantify how well the PCA_c model captures the recurrent pattern. We also analyze the factor loading, or the correlation of the PCA_c to the FDL_c data. Both the variance and factor loadings are calculated for each PCA_c and compared.

A more complete picture of the difference between two PCA_c models can be found by considering the raw pixel values of the models. A pixel value for a given PCA_c describes the *relative timing of melt* of a pixel in relationship to all the other pixels. A value closer to zero melts earlier than a value further away from zero. We order the pixels from 1 to *T* where 1 melts first and *T* melts last. For a given pixel in a PCA_c model we can denote the pixel's *relative timing of melt* as t_i. Because *T* is equal in length for all PCA_c models, a direct comparison of the t_i describes how the *timing of melt* for

pixel t_i changed for each PCA_c model. For example, the PCA_{40} model may record a pixel as the 10,000th pixel to melt (t_i equal to 10,000). For the same pixel, PCA_{10} may record a t_i value of 8,000. Therefore, the timing of melt for that pixel has shifted 2,000 pixels earlier for one model compared with the other. The *true recurrent pattern* would be represented by accurate description of the *relative timing of melt* determined by t_i of each pixel. Comparing the shift in the relative position of t_i for two models graphically communicates the similarity or dissimilarity of the models.

While the comparison of the shift in melt timing communicates how the models differ in timing, a spatial comparison highlights where in the study site these shifts in t_i occur. Certain locations within the watershed may have very poor viewing condition all the time making them more error prone. This spatial comparison can illuminate where and potentially why these errors arise. We normalize the PCA_c models to a 0 to 1 scale and subtract the normalized PCA_c models. The output is a heat map of where the greatest differences between models occurred. This comparison is completed for only select PCA_c models.

Model Performance Validation

Spatial accuracy of each PCA_c model against independent data is the best method for identifying the most accurate model. A wealth of data is available and we use all available MODIS data, not just the independent data, to quantify clear day accuracy. For a given model, PCA_c, we quantify the spatial accuracy for every image (Img_c) with less than 10% cloud cover. It is important to note the image and model are using the same value of "*c*". The best fit PCA_c, SCA is determined by equation 4.2, the *VPE*. To implement equation 4.2, a PCA_c model converted to a binary SCA is compared against a given Img_c. We calculate the number of pixels incorrectly modeled as snow free (I_L), the number pixels of incorrectly modeled as snow covered (I_S), and the total number of visible pixels (T_P). Given an image with 10% cloud cover the total number of visible pixels would be equal to 90% of total pixels in the study site.

Equation 4.2

$$VPE = \sqrt{\frac{{I^2}_L + {I^2}_S}{{T^2}_P}}$$

The spatial accuracy is given as a percentage shown in equation 4.3. We use the same value of "*c*" so as to not introduce errors contained in the selection "*c*" for either the PCA_c or Img_c. We are intentionally comparing the best case scenario. The highest accuracy should be found by comparing,

for example PCA_{10} versus Img_{10}, rather than PCA_{10} versus Img_{50} if each PCA_c accurately captures the recurrent pattern. This issue is discussed below. The accuracy is expressed as a percent.

Equation 4.3

$$ACC = \left(1 - \frac{I_L + I_S}{T_P}\right) \times 100\%$$

Quantifying the Source of Spatial Error

The foundational question we are addressing is what value of "*c*" produces the most accurate model of the *true recurrent* pattern. We must address whether the higher accuracies with a different value of "*c*" are due to a more spatially accurate model, or due to a less robust picture of snow coverage using different values of "*c*"? We compare the most accurate PCA_c as determined by the previous steps against clear day images (Img_c), but with varied values of "*c*". For example, we would compare the PCA_{10} model with a cloud free image with the following values of "*c*": Img_{15}, Img_{20}, Img_{25}, etc. For example, if the PCA_{10} model is truly more spatially accurate than the PCA_{40} model, then the clear day accuracy of the PCA_{10} versus Img_{40} should be higher than PCA_{40} versus Img_{40}. This would indicate that the *true recurrent* pattern is better captured by PCA_{10} rather than PCA_{40}. On the other hand, if the spatial accuracy for PCA_{10} versus Img_{40} is less than the spatial accuracy of PCA_{40} versus Img_{40}, then we can attribute the accuracy difference to the selection of "*c*" rather than the model. This final analysis quantifies if the best fit pattern is robust against different user selections of the value of "*c*".

Results

The results are presented in the following order. First, for each PCA_c model we present descriptive statistics, factor loadings, visual comparisons, and a comparison of the shift in melt timing between select models. Second, a formal analysis of the spatial accuracy of the PCA_c models is presented which allows us to select the best model of the *true recurrent pattern*. Finally, we analyze the source of the spatial errors as it relates to the selection of "*c*" for the Img_c.

PCA_c Model Results

FDL_c images were calculated for values of "*c*" ranging from 10 to 90 for the period of 2000-2016. A PCA is then applied to the FDL_c images to find the resulting PCA_c model. Two descriptive statistics describe how well each PCA_c captured the recurrent spatial pattern of snowmelt: total dataset variance described by PCA_c model and the factor loadings. Factor loadings are the correlation of a given PCA_c model with the corresponding FDL_c images. We calculate 17 correlations, one for

each year. Four values are reported in Table 4.1: the total dataset variance described for each PCA_c, as well as the minimum, maximum, and average factor loadings.

Table 4.1: Descriptive statistics for each PCA_c model. The total dataset variance described by each PCA_c model is given as well as the minimum, average, and maximum factor loadings for the comparison of each PCA_c versus the corresponding FDL_c.

PCA_c	First Principal Component Variance	Factor Loading Minimum	Factor Loading Average	Factor Loading Maximum
10	0.936	0.949	0.968	0.979
15	0.929	0.945	0.964	0.977
20	0.919	0.935	0.959	0.974
25	0.905	0.921	0.952	0.967
30	0.889	0.908	0.943	0.958
35	0.871	0.892	0.933	0.951
40	0.848	0.877	0.920	0.940
45	0.820	0.866	0.905	0.929
50	0.784	0.840	0.884	0.913
55	0.725	0.787	0.851	0.894
60	0.645	0.710	0.797	0.870
65	0.606	0.640	0.763	0.853
70	0.643	0.555	0.786	0.862
75	0.670	0.505	0.797	0.891
80	0.620	0.480	0.750	0.860
85	0.491	0.253	0.596	0.832
90	0.406	0.011	0.386	0.859

There is a steady decrease in the variance described from 0.936 to 0.606 from PCA_{10} to PCA_{65} where a local minimum is recorded. From PCA_{70} to PCA_{75} the variance described increases after which it declines to a value of 0.406 at PCA_{90}. These variance values suggest that at a certain point the recurrent pattern is not captured and instead noise is represented. The factor loadings further support this hypothesis. At PCA_{10}, all three of the factor loadings are the largest with minimum, average, and maximum values of 0.949, 0.968, and 0.979 respectively. The factor loadings steadily decline until PCA_{65}, which mirrors the variance. At PCA_{90}, the lowest factor loadings are recorded with values of 0.011, 0.386, and 0.859 for the minimum, average, and maximum, respectively. The factor loadings are an initial indication of how well the recurrent pattern is or is not captured by each PCA_c model. The factor loadings also describe the quality of the FDL data, discussed later.

Significant decreases in the minimum and average factor loadings are found at PCA_{65} to PCA_{90}, and because of this we can conclude the best recurrent pattern is not captured by these PCA_c models. These results also support our hypothesis that the recurrent pattern is best captured by PCA_{10}.

The results in Table 4.1 indicate there is little difference for PCA_{10} through PCA_{50}. This set of PCA_c models maintain large factor loadings (minimum greater than 0.8) and they describe a large portion of the total dataset variance. A sharp decline in the minimum factor loadings is recorded from PCA_{50} to PCA_{55}. A spatial visualization the difference between PCA_c and FDL_c images may offer more insight. Figure 4.2 shows from left to right the FDL_{10}, FDL_{40}, and FDL_{90} calculated for 2006 in the top row and PCA_{10}, PCA_{40} and PCA_{90} in the bottom row. In all six panes black indicates the first pixels to melt and white the last. A well-defined recurrent pattern, or PCA_c model (bottom row), should look very similar to a topographic map. One can clearly see that PCA_{10}, bottom left, has the smoothest transition from earliest to last pixel to melt, or black to white. PCA_{40} on the other hand, bottom center, has many black (early to melt) pixels completely surrounded by white pixels (last to melt). This is recorded most notably in the Northern third of the watershed. These pixels are likely spurious errors. PCA_{90} is nearly all black with only a few white pixels. As suspected, PCA_{90} does not capture the recurrent pattern of melt.

The quality of the three PCA_c models is mirrored by the quality of the FDL_c images, Figure 4.2. FDL_{10}, top left, shows a smooth progression of melt. A few black pixels surrounded completely by white pixels, or potential errors, exist. An example of these errors can be seen in the Southeastern portion of the watershed. FDL_{40} also shows a fairly smooth description of melt, top center. One difference between FDL_{10} and FDL_{40} is that the most northern tip of the watershed melts first in FDL_{40}, while the southwest portion of the watershed melts first in FDL_{10}. FDL_{40} also has far more dark pixels surrounded completely by white pixels. FDL_{90}, top right, is a complete departure from the other two images in the top row. These FDL_c images presented in Figure 4.2 are calculated for 2006; however, the same relationship is found by the other 16 years. The quality of the FDL_c image has significant implications for the ability of the PCA_c model to capture the recurrent pattern of melt.

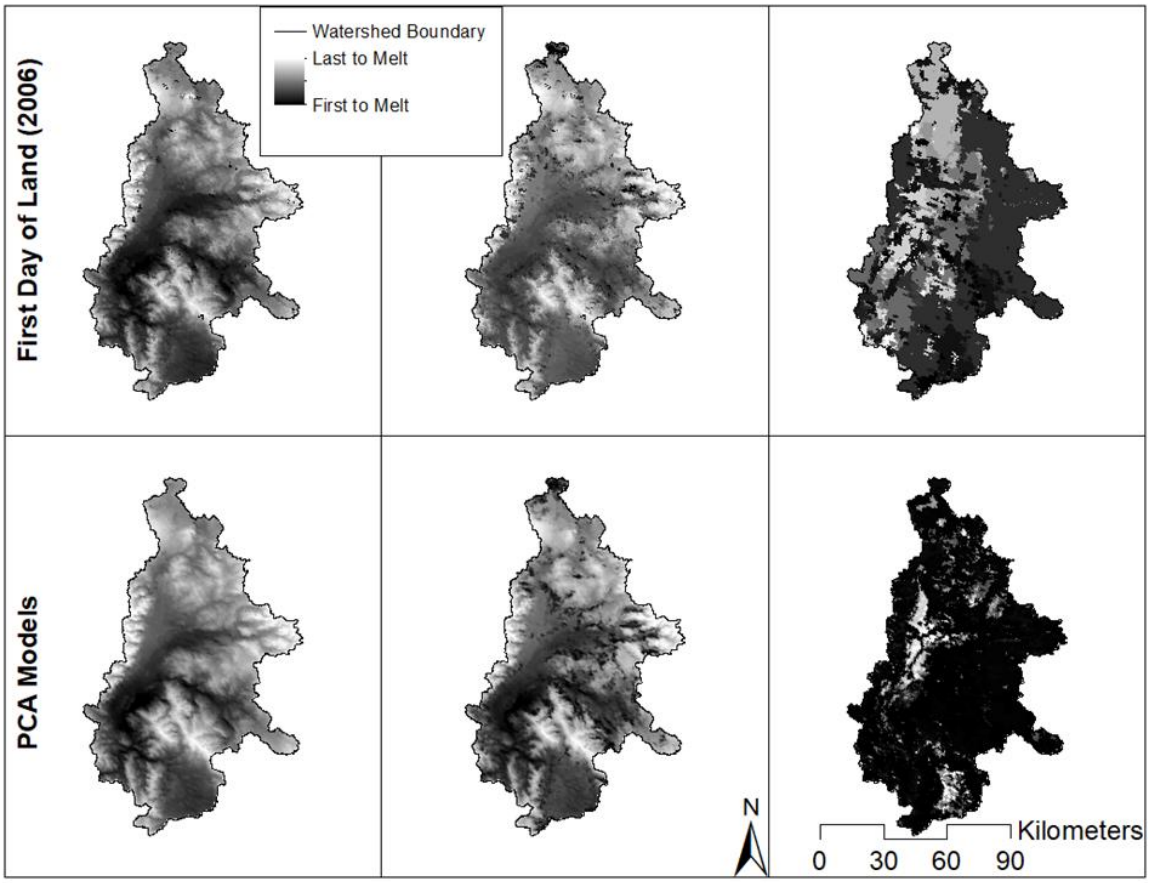

Figure 4.2: FDL images for melt period of 2006 are shown for FDL_{10}, FDL_{40}, and FDL_{90} in the top row from left to right, respectively. The PCA calculated using FDL's for 2000-2016 are shown from left to right, PCA_{10}, PCA_{40}, and PCA_{90}. The darkest areas melt the earliest and the lightest values melt the latest for all 6 images shown.

We have demonstrated the *true recurrent pattern* is best captured by one of the models between PCA_{10} through PCA_{50}. We can visualize what appear to be minute differences in the results presented thus far by conducting a spatial comparison of the PCA_c models. To spatially compare these models, we first normalize the PCA_c models. The normalized models are on a 0-1 scale where zero melts first and one melts last. Next, we subtract the normalized models. The result is a heat map of the differences between the models. This shows the degree to which these models differ. The results from the subtraction of two normalized models are shown in Figure 4.3. On the left, PCA_{10} is subtracted from PCA_{40}. Green areas show where the PCA_{40} model melts earlier than the PCA_{10} model, and red shows where the PCA_{40} model melts later. There are quite a few green areas that correspond to the areas of early melt discussed in Figure 4.2 above. The legend also shows the green values are significantly larger than the red values. Therefore, the greatest difference between these models resides in the pixels which PCA_{40} indicates should melt first. In contrast the right pane of Figure 4.3

depicts PCA_{10} subtracted from PCA_{15}. The range in values is far smaller, -0.15 to 0.11, for this model compared to PCA_{40} and PCA_{10}, -0.56 to 0.16. This demonstrates the PCA_{15} model is far more similar to the PCA_{10} model than the PCA_{40} model is. Interestingly we see that the areas which are green for the left pane of Figure 4.3 are present but smaller in the right pane. These pixels may have difficult viewing conditions leading to these spurious errors. They are a result of less consistent data for those pixels in particular in the daily MODIS images. These errors are present in the FDL_c and propagate through to the PCA_c.

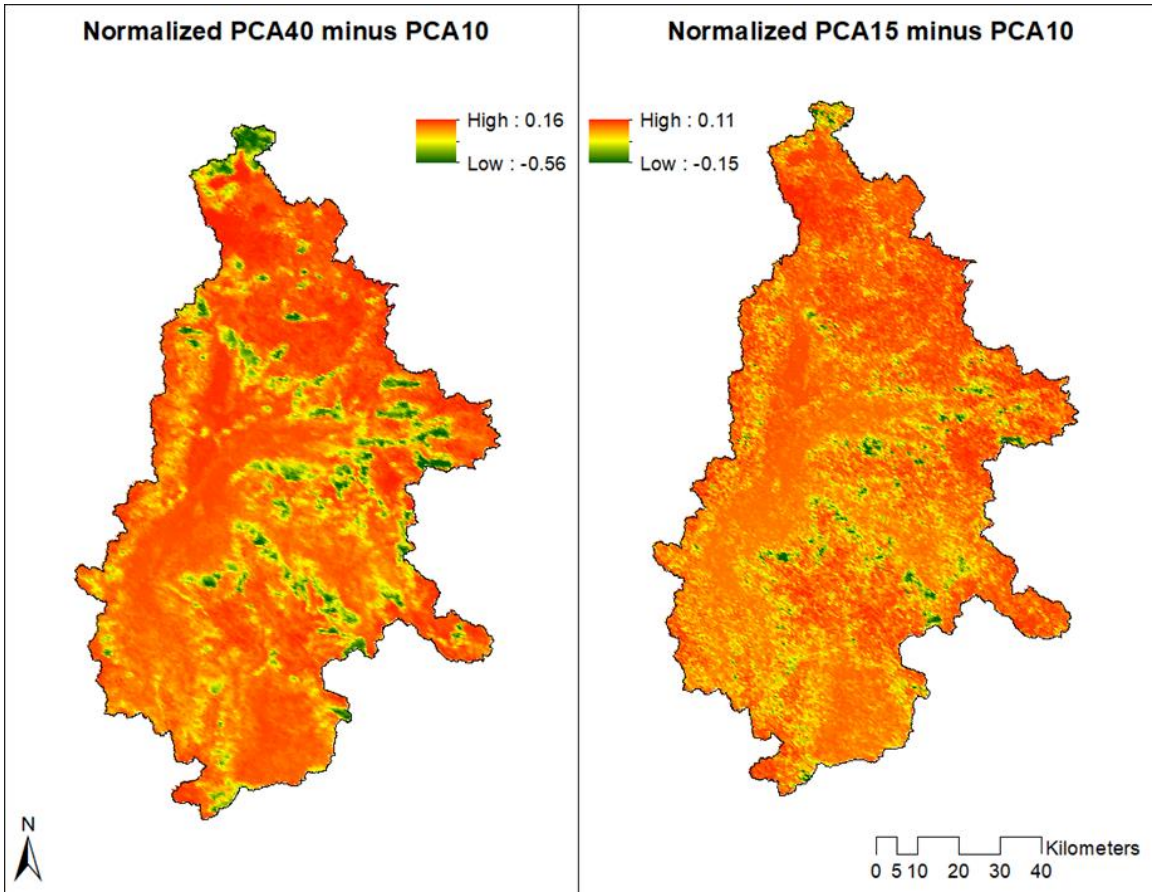

Figure 4.3: Normalized difference between three PCA models are shown as a heat map. On the left the normalized PCA_{10} model is subtracted from the normalized PCA_{40} model. On the right the normalized PCA_{10} model is subtracted from the normalized PCA_{15} model.

One final comparison of the PCA_c models may show the degree to which the models differ in pixel by pixel melt timing. We compare the shift in a pixel's melt timing given different PCA_c. A direct comparison of, for example, PCA_{10} versus PCA_{15} shows how the pixel values changed; however, if we order the pixel values from closest to zero (first to melt) to furthest away from zero (last to melt) we then have each pixel's *relative timing of melt* given by the PCA_c, or simply the pixel

melt order. If we plot the ordered values for two PCA_c model's against one another, we show how the relative timing of melt of each pixel changes for different PCA_c models.

In Figure 4.4 two comparisons are shown. The red triangles show the ordered values for each pixel for PCA_{15} plotted against the ordered values of PCA_{10}. If the two models were exactly the same, the points would fall on a one-to-one line. We can see these two model's produce very similar descriptions of when each pixel melts or the pixel's relative melt timing. The black circles are the ordered values for PCA_{40} plotted against the ordered values of PCA_{10}. Many of the points fall on the one-to-one line which is obscured by the red triangle, but quite a few fall below. Points which fall close to the x-axis at large x values (ordered PCA_{10} values) have significantly different relative melt timing according to these two models. According to PCA_{10}, pixels with large x-values should melt late in relation to other pixels in the study site. In Figure 4.4, many points with large x-values have small y-values. This means the PCA_{40} has assigned these pixels early relative melt timing. Referring back to Figure 4.3 (left), this result makes sense. PCA_{40} showed green areas indicating earlier melt timing compared with PCA_{10}. Woodruff & Qualls (2019) noted these areas as a potential source of error in their model of the recurrent pattern of melt. The PCA_{40} model has locations which incorrectly melt early. This leads to spatial errors until the snowline reaches and absorbs those locations. In Figure 4.4, these two PCA_c models converge to very similar melt timing at around y- axis ordered pixel 30,000 and 35,000. This is associated with about 27% SCA. In Woodruff & Qualls (2019) spatial accuracy was lowest at larger SCA values (smaller y-axis values in Figure 4.4) and largest (above 92% spatial accuracy) for SCA values smaller than 35%. According to Figure 4.4, The PCA_{10} model may more accurately describe relative melt timing. A more accurate description of melt timing should result in greater spatial accuracy.

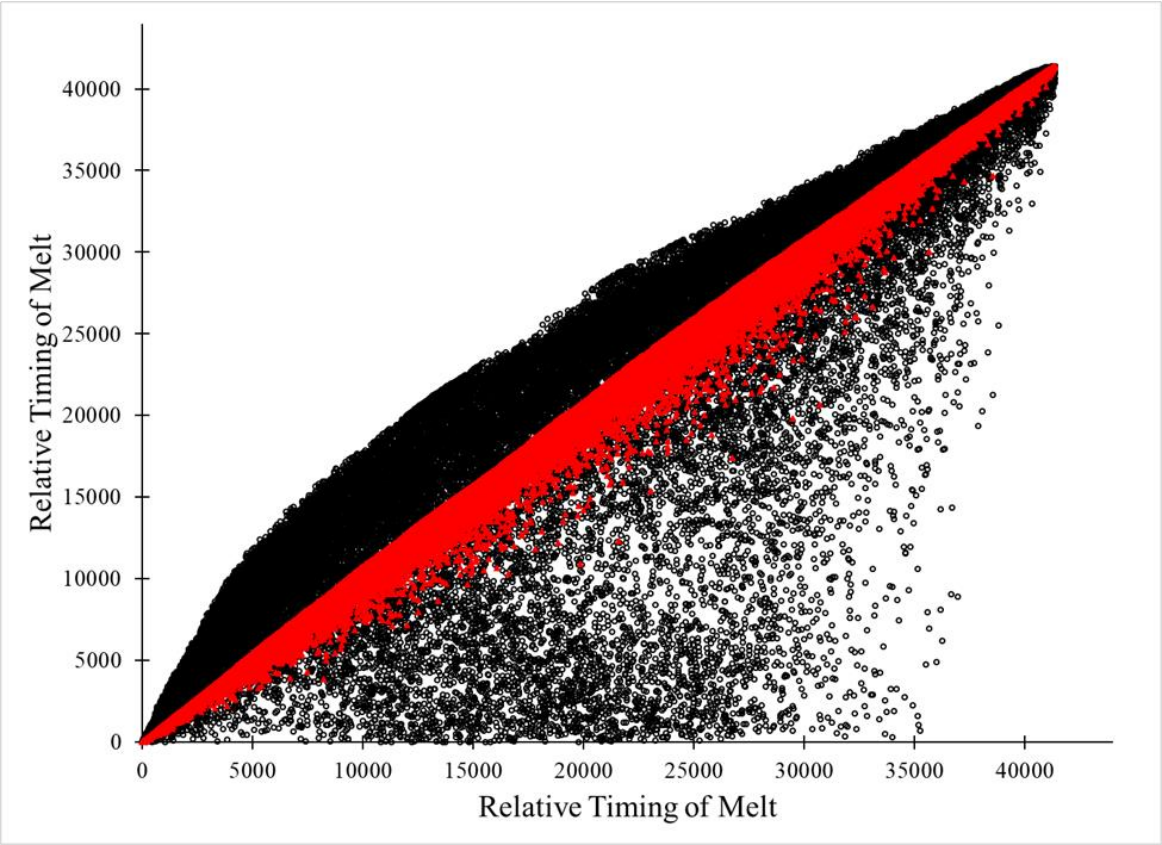

Figure 4.4: The ordered relative timing of melt of all pixels in PCA_c models is shown for three PCA_c models. The black circles show the PCA_{40} ordered relative timing of melt values (y-values) plotted against the PCA_{10} ordered relative timing of melt values (x-values). The red circles show the PCA_{15} ordered relative timing of melt values (y-values) plotted against the PCA_{10} ordered relative timing of melt values (x-values).

Spatial Accuracy of PCA_c Models

Thus far we have compared model to model differences however the true test of a model is validation against raw data. Before we can choose which model best captures the recurrent pattern, an assessment of the spatial accuracy of each model versus clear day imagery was conducted. Every cloud free (<10% cloud cover) image for the periods of 2000-2017 was compared with each PCA_c model. As these models describe the melting period and not the accumulation, we chose to limit the analysis to day of year 1 to 250 beginning on January 1. A total of 945 cloud free images exist for this 18 year period. We compare each PCA_c model with the corresponding Img_c. For example, PCA_{10} would be compared with cloud free images classified into snow and no snow using a value of 10 for "*c*", or Img_{10}. The *true recurrent pattern* should be the most spatially accurate model. Due to the volume of cloud free images available we present the calculated accuracies in boxplots, Figure 4.5.

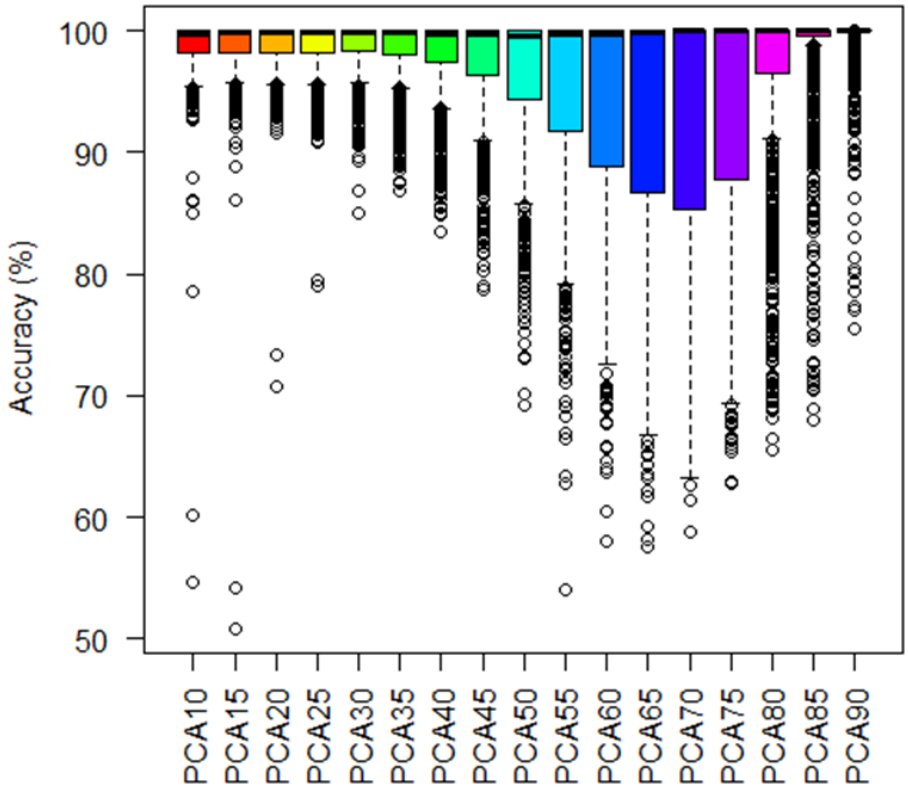

Figure 4.5: Boxplot of accuracies in percent are given for all PCA_c models. Accuracies are calculated for all cloud free images for the period of 2000-2017.

As seen in Figure 4.5, the accuracy of PCA_{10} through PCA_{35} are fairly similar aside from a small number of outliers. Interestingly we see the magnitude of the outlier's decrease between PCA_{30} and PCA_{45}. The median accuracy, indicated by the black line within the box, also remains very large for all PCA_c models. Similar to the variance and factor loadings shown in Table 4.1, we see the lower quartile of the accuracy, indicated by the lowest value of each box, remain large (>95%) for PCA_{10} through PCA_{45}. The minimum accuracy plummets between PCA_{50} and PCA_{70} after which it increases. These results suggest that between PCA_{10} through PCA_{45} the recurrent pattern is captured to some degree. It then breaks down and noise is captured by the model. Both the Img_c and PCA_c at large values of "*c*" do not capture any sort of recurrent behavior. The PCA method captures some degree of the *true recurrent pattern* for a wide range of values of "*c*", but as clearly shown in Figure 4.5 this

breaks down as "*c*" increases. This plot also suggests, contrary to previous results, that PCA_{35} of PCA_{40} may be the best model due to lack of significant outliers noted for PCA_{10} through PCA_{30}.

One important note is the accuracies shown in Figure 4.5 include images with 100% and 0% snow cover at the beginning and end of the melting period. Our purpose is to identify the model that most closely captures the *true recurrent pattern*, therefore these values which potentially over inflate the accuracy, hinder our ability to select the best PCA_c model. A more stringent approach is to restrict our validation window to a SCA range for the actively melting time period. We use the SCA calculated for PCA_{10} (SCA chosen by each model on a given day fluctuates so we use only one model to select the days to include) to filter the results and include only accuracies calculated for the range of 90-10% SCA. The averages accuracies for 2000-2017 for this subset are presented in Table 4.2. We exclude the PCA_c models greater than PCA_{50} because these do not accurately describe the recurrent pattern as shown in Figure 4.5. The average accuracies for the full dataset are given in column one of Table 4.2. The highest average accuracy of 98.76% (indicated by red font) was found at PCA_{20}. The values in column one are nearly equivalent between PCA_{10}-PCA_{25}. When we apply the filter the distribution of the averages describe a different story, see column two. We record the highest average accuracy of 95.46% for PCA_{10}. This is also substantially higher than PCA_{15}, 95.24%. Referring to column one in Table 4.2, one can see the full dataset average accuracies for PCA_{10} through PCA_{25} were all within a range of 0.07%. When we restrict the dataset to only the melt period (SCA 90-10%) there is an immediate reduction in accuracy by 0.22% from PCA_{10} and PCA_{15}. From PCA_{15} through PCA_{45} we record a drop in the average spatial accuracy by 4% for the reduced dataset. This is far larger than the 1.49% range in accuracy for the full dataset, column one. These results clearly identify PCA_{10} as the most accurate representation of the *true recurrent pattern*.

Table 4.2: Average accuracies calculated for PCA10 through PCA45 are shown for all cloud free images in the period of 2000-2017. Also shown are the average accuracies calculated for each model using the subset found by restricting images to the SCA range of 90-10%.

PCA_c	Mean of Full Cloud Free Data	Mean Cloud Free Data with SCA between 90-10%
PCA_{10}	98.69	**95.46**
PCA_{15}	98.72	95.24
PCA_{20}	**98.76**	95.19
PCA_{25}	98.71	94.82
PCA_{30}	98.6	94.3
PCA_{35}	98.38	93.56
PCA_{40}	97.96	92.61
PCA_{45}	97.27	91.39

Determining the Source of Spatial Error

We have demonstrated that the *true recurrent pattern* is best captured by PCA_{10}; however, we have not determined whether that is a function of the model or a function of specific value of "*c*" used to classify the daily imagery. We can determine whether the error lies in the model or in the classification of the daily imagery by calculating the accuracy of the PCA_{10} model versus Img_{15}, Img_{20}, $Img_{25,}$ etc. and comparing it against the accuracy a given PCA_c versus its equivalent Img_c. For example, if the PCA_{10} model versus Img_{20} is more spatially accurate than the PCA_{20} versus Img_{20}, then we can confidently state the PCA_{10} model is the most accurate model.

For this final comparison we use the cloud free data from 2018-2020, which is all independent data. The spatial accuracy of each PCA_c versus the corresponding Img_c was calculated for each PCA_c model. The spatial accuracy of the PCA_{10} model against Img_{15}, Img_{20}, Img_{25}, etc. through Img_{90} was also calculated. The mean spatial accuracy for each year was calculated for both comparisons. We then subtract the mean accuracy calculated for the PCA_c versus Img_c from the mean accuracy calculated for PCA_{10} versus Img_c. A positive result indicates the PCA_{10} model was more spatially accurate than the PCA_c versus Img_c. The results are given in Table 4.3. The PCA_{10} model is the superior model compared with PCA_{15} through PCA_{45} as seen by the total average (far right column). After this point, the benefit of the PCA_{10} declines. This is likely due to the noisy data, which

also describes why the PCA method loses spatial accuracies at larger values of "*c*". The source of the spatial error in PCA_c models is a result of the FDL_c development because the Img_c values are noisier at larger values of "*c*".

We can conclude two equally important points from Table 4.3. One, the errors we see in the PCA_c model is likely due to early identification of melt in the FDL_c models. This is clearly communicated by the increase in accuracy using the PCA_{10} mode. Persistent errors exist in the other models. Two, every PCA_c model from PCA_{10} though PCA_{45} captures some degree of the recurrent pattern. This does not mean a pattern cannot be extracted at greater values of "*c*" (greater than 50), but it does mean our method cannot accomplish this with reasonable accuracy.

Table 4.3: Difference in spatial accuracy of a given PCA_c model compared with its corresponding Img_c images compared with PCA_{10} model compared with Img_c image for 2018-2020 cloud free images. A positive result indicates the PCA_{10} model more accurately represents SCA than the straight across comparison of the corresponding PCA_c model.

PCA_{10} - PCA_c	2018	2019	2020	Total Average
PCA_{15}	0.04	0.04	0.04	0.04
PCA_{20}	0.10	0.08	0.04	0.07
PCA_{25}	0.17	0.13	0.05	0.12
PCA_{30}	0.22	0.21	0.08	0.17
PCA_{35}	0.35	0.33	0.12	0.27
PCA_{40}	0.55	0.55	0.23	0.45
PCA_{45}	**0.76**	0.77	**0.39**	**0.64**
PCA_{50}	0.51	**0.80**	0.35	0.55
PCA_{55}	0.28	0.37	0.00	0.22
PCA_{60}	-0.37	-0.92	-0.81	-0.70
PCA_{65}	-0.87	-3.45	-2.19	-2.17
PCA_{70}	-0.74	-5.18	-2.50	-2.81
PCA_{75}	-0.13	-4.78	-2.49	-2.46
PCA_{80}	0.02	-2.74	-0.91	-1.21
PCA_{85}	0.15	-0.14	-0.11	-0.03
PCA_{90}	-0.14	-0.09	0.02	-0.07

Discussion

Although the pattern breaks down, we can use the best fit model PCA_{10} to extract more information on a given day about snowmelt than previously thought. There is a gradation of information that can be extracted with the recurrent pattern by comparing the PCA_{10} model versus Img_{15}, Img_{20}, and Img_{25} etc. Each of these represents a description of the how many pixels have

changed on that day. This information was previously useless because we lacked a normalized method of comparison. A significant amount of research has been invested in producing subpixel resolution SCA and improved SCA data based on variations in the NDSI (Painter et al. 2009; Rittger et al., 2020). Far fewer have approached the SCA information from an image patterning perspective, as we do here. Ultimately the pattern approach lends itself to ideas that support the use of ANN, specifically higher order patterns that we do not represent in our current snowmelt modeling frameworks. This result opens the door to new analyses about snowmelt modeling as described by the recurrent pattern versus different thresholds. We have demonstrated there is a range in values of "*c*" that are useful: 10-45. The potential for this application is shown in Figure 4.6.

In Figure 4.6 we show the multiple SCA values found by comparing PCA_{10} versus varied Img_c values for the 2018 melt period. In the top pane of Figure 4.6, the PCA_{10} model was compared against Img_{10}, Img_{25}, and Img_{40} which a given by a black hollow circle, red X's, and blue hollow triangles, respectively. We can see quite clearly that the points are all very similar at the beginning (before DOY 100) and end of melt (after DOY 200). The vertical distance between the points for a given DOY signifies the difference in SCA by simply altering the value of "*c*" used to classify Img_c. The vertical distance increases through the middle of melt. Rather than a single SCA value for a given day we now have information about the distribution of melting pixels in relationship to the recurrent pattern of melt. To further verify that the recurrent pattern breaks down at values of "*c*" greater than 45 we have plotted SCA values calculated for Img_{10} (for reference), Img_{50}, Img_{70}, and Img_{90} in the bottom pane of Figure 4.6 as hollow black circles, solid black circles, red triangles, and blue crosses, respectively. The Img_{90} values do not resemble the Img_{10} values at all. Img_{70} values are a departure from the time series of Img_{10} as well. Img_{50} values are the most similar to the baseline Img_{10}, but we can note there is significant variability early in the melt period. These plots demonstrate the existence of a recurrent pattern for values of "*c*" between 10 and 45, and a breakdown of the pattern above 45.

Applying the PCA_{10} model against all the applicable Img_c values (10-45) can offer a snapshot of the snowmelt progression with only a single MODIS image. This is an area of research worth investigating as it may be a foundational step towards forecasting snowmelt given only a remotely sensed images. Rather than a single point of SCA for a given day we now can produce multiple values which theoretically could increase prediction accuracy, similar to how multiple ground-based stations increase simulation accuracy. A similar analysis could be done without the recurrent pattern; however, there would be no normalized way of comparing what is measured at different values of "*c*". It is the existence and application of a pattern that makes this information valuable. The data

collected by MODIS about SCA is spatially normalized across multiple years providing a baseline of comparison in a single year and in a single image. Watershed characteristics offer more than simplifying a complex system. In our case, this watershed characteristic provides a new approach to analyzing how snow melts over a landscape and how it behaves over multiple years. We have demonstrated the accuracy of the PCA model of the recurrent pattern of melt can be increased by lowering the value of "*c*" in the derivation of the FDL and LDS values. From Table 4.2 we can see that during the melting period for 2000-2017 the average spatial accuracy of the previously published model (Woodruff & Qualls, 2019) is 92.61% and by lowering the value of "*c*" we find an average accuracy of 95.46%.

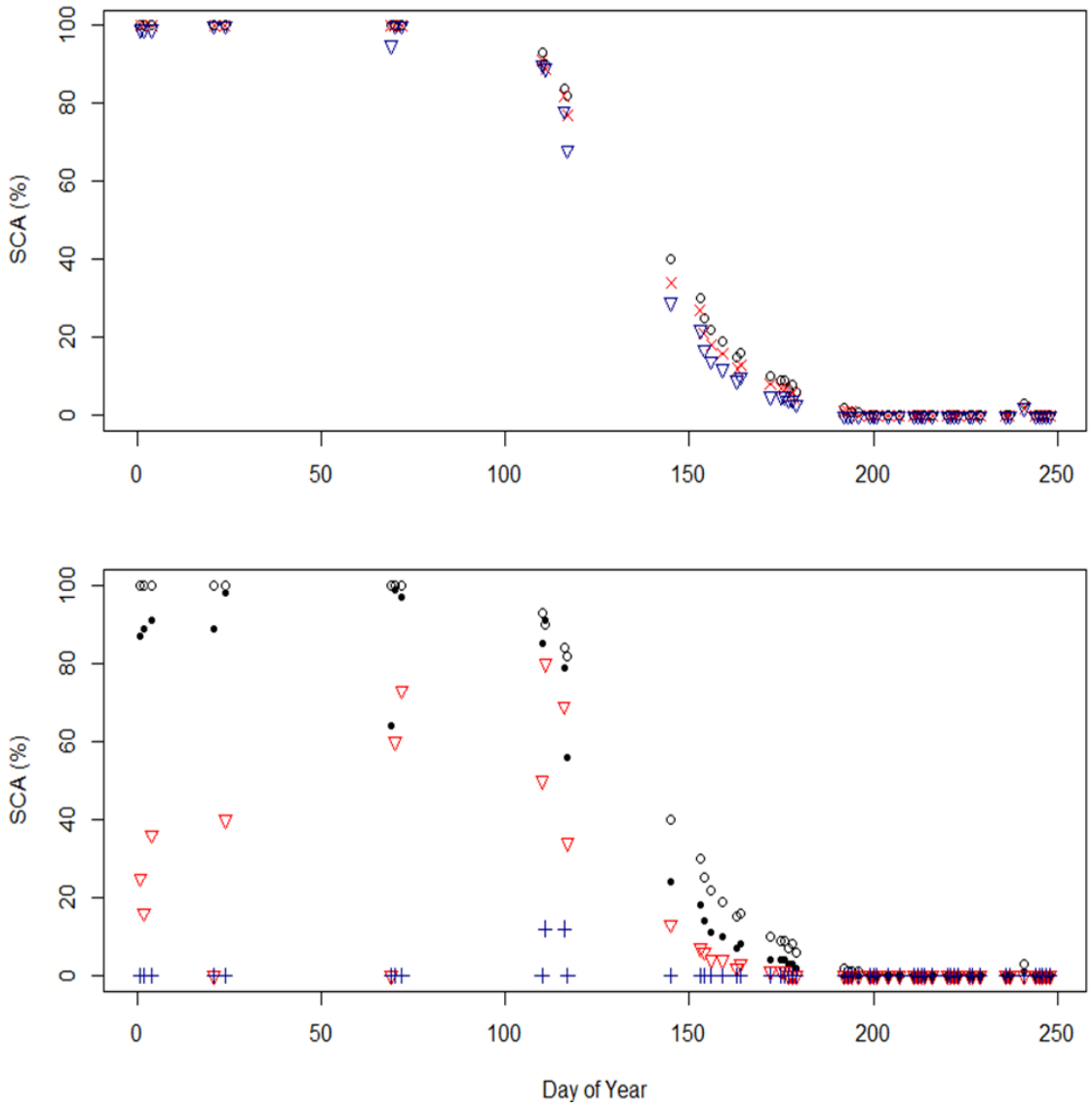

Figure 4.6: Two plots of SCA calculated using PCA_{10} versus Img_c for varied values of 'c' are shown for the melt period of 2018. In the top panel SCA values for Img_{10}, Img_{25}, and Img_{40} are given by the black hollow circles, red X's, and blue triangles, respectively. In the bottom panel SCA values for Img_{10}, Img_{50}, Img_{70} and Img_{90} are given by the black hollow circles, black solid circles, red triangles, and blue crosses, respectively.

Conclusions

In this article we have presented a robust validation of the recurrent pattern of snowmelt using the spatio-temporal PCA model as derived from 17 years of remotely sensed MODIS data for the Upper Snake River Basin. We have demonstrated that increased spatial accuracy can be achieved by altering the user selection of "*c*". We found the PCA_{10} model was the most accurate model and achieved average spatial accuracies of 95.46% for the period of 2000-2017, which includes one independent year. For the independent period of 2018-2020 the PCA_{10} more accurately represented

SCA for a given Img_c with "*c*" varied from 15-90 than the direct comparison i.e., PCA_{15} versus Img_{15}. This robust analysis indicates PCA_{10} is the most spatially accurate model and produces higher average spatial accuracy (95.46%) than the previously published model (92.61%) by Woodruff & Qualls (2019).

The spatio-temporal PCA model of snowmelt has been demonstrated to be spatially and temporally recurrent and, in this work, we show that the spatial accuracy can be increased by tuning the user selection of "*c*". In the data rich world we live in, spatial and temporal patterns are crucial to expanding our knowledge of the complex system of snowmelt. As clearly demonstrated in the literature, ANN, Deep Learning, and other data driven approaches produce exceptionally high accuracies for simulating streamflow, but we sacrifice interpretability. Our physically based models are easily interpreted but lack accuracy and low computational cost that data driven approaches provide. The spatio-temporal PCA model of snowmelt is a potential bridge between data driven ANN and physically based snowmelt runoff models. This pattern is not explicitly described in physically based snowmelt models. It is on average 95.46% accurate during the crucial melt period. The same pattern can be used year after year because it is unchanging. It is not computationally expensive to derive or use. We have derived this higher order pattern, which is an inaccessible characteristic utilized by ANN, and packaged it into an easily digestible framework for use in physically based snowmelt runoff models.

Moving forward the intrinsically valuable spatio-temporal model of snowmelt can and should be directly compared to physically based models and should be worked in as a data input. The value of a recurrent pattern cannot be overstated for the highly variable process of snowmelt. This work clearly and thoroughly demonstrates exactly how robust this pattern is spatially and what a valuable tool it can be to water managers everywhere.

References

Adams, W. P. (1976). Areal differentiation of snow cover in east central Ontario, Water Resources Research, 12(6), 1226– 1234, https://doi.org/10.1029/WR012i006p01226

Barnett, T.P., Adams, J.C. & Lettenmaier, D.P. (2005). Potential impacts of a warming climate on water availability in snow-dominated regions. Nature, 438, pp.303–309.

Bloschl, G., & Sivapalan, M. (1995). Scale issues in hydrological modelling: a review. Hydrological Processes, 9(3-4), 251–290. https://doi.org/10.1002/hyp.3360090305

Cherkauer, K. A., & Lettenmaier, D. P. (2003). Simulation of spatial variability in snow and frozen soil. Journal of Geophysical Research: Atmospheres, 108(D22). https://doi.org/10.1029/2003JD003575

Flores, J. A. (2011). Focus on artificial neural networks. Nova Science Publishers.

Hall, D. K., & Riggs, G. A. (2007). Accuracy assessment of the MODIS snow products. Hydrological Processes, 21(12), 1534-1547. https://doi.org/10.1002/hyp.6715

Hall, D. K. & Riggs, G. A. (2016). MODIS/Terra Snow Cover Daily L3 Global 500m Grid, Version 6. [NDSI snow cover]. Boulder, Colorado USA. NASA National Snow and Ice Data Center Distributed Active Archive Center. doi: https://doi.org/10.5067/MODIS/MOD10A1.006. [January 2017 - July 2021].

Hall, D. K., Riggs, G. A., Digirolamo, N. E., & Roman, M. O. (2019). Evaluation of MODIS and VIIRS cloud-gap-filled snow-cover products for production of an Earth science data record. Hydrology And Earth System Sciences, 23(12), 5227–5241. https://doi.org/10.5194/hess-23-5227-2019.

Homer, C.G., Dewitz, J.A., Yang, L., Jin, S., Danielson, P., Xian, G., Coulston, J., Herold, N.D., Wickham, J.D., & Megown, K., (2015). Completion of the 2011 National Land Cover Database for the conterminous United States-Representing a decade of land cover change information. Photogrammetric Engineering and Remote Sensing, v. 81, no. 5, p. 345-354

Kanishka, G., & Eldho, T. I. (2020). Streamflow estimation in ungauged basins using watershed classification and regionalization techniques. Journal of Earth System Science, 129(1). https://doi.org/10.1007/s12040-020-01451-8

König, M. & Sturm, M. (1998). Mapping snow distribution in the Alaskan Arctic using aerial photography and topographic relationships, Water Resour. Res., 34(12), 3471–3483, https://doi.org/10.1029/98WR02514

Luce, C. H., & Tarboton, D. G. (2004). The application of depletion curves for parameterization of subgrid variability of snow. Hydrological Processes, 18(8), 1409-1422. https://doi.org/10.1002/hyp.1420

Martinec, J. & Rango, A. (1986). Parameter values for snowmelt runoff modelling. Journal of Hydrology, 84(3), pp.197–219.

Mote, P. W. (2003). Trends in snow water equivalent in the Pacific Northwest and their climatic causes. Geophysical Research Letters, 30(12), 1601–n/a. https://doi.org/10.1029/2003GL017258

Newman, A. J., Clark, M. P., Winstral, A., Marks, D., & Seyfried, M. (2014). The Use of Similarity Concepts to Represent Subgrid Variability in Land Surface Models. Journal of Hydrometeorology, 15(5), 1717–1738. https://doi.org/10.1175/JHM-D-13-038.1

Painter, T. H., Rittger, K., McKenzie, C., Slaughter, P., Davis, R. E., & Dozier, J. (2009). Retrieval of subpixel snow covered area, grain size, and albedo from MODIS. Remote Sensing of Environment, 113(4), 868–879. https://doi.org/10.1016/J.Rse.2009.01.001

Parr, C., Sturm, M., & Larsen, C. (2020). Snowdrift landscape patterns: An Arctic investigation. Water Resources Research, 56, e2020WR027823. https://doi.org/10.1029/2020WR027823

Pham, L. T., Luo, L., & Finley, A. (2021). Evaluation of random forests for short-term daily streamflow forecasting in rainfall- and snowmelt-driven watersheds. Hydrology and Earth System Sciences, 25(6), 2997–3015. https://doi.org/10.5194/hess-25-2997-2021

Pflug, J. M., & Lundquist, J. D. (2020). Inferring Distributed Snow Depth by Leveraging Snow Pattern Repeatability: Investigation Using 47 Lidar Observations in the Tuolumne Watershed, Sierra Nevada, California. Water Resources Research, 56(9), n/a–n/a. https://doi.org/10.1029/2020WR027243

Qualls, R. J., Taylor, R. G., Hamilton, J., & Arogundade, A. B. (2013). Climate change opportunities for Idaho's irrigation supply and deliveries. Journal of Natural Resources Policy Research, 5(2-3), 91–105. https://doi.org/10.1080/19390459.2013.811856

Rice, J. S., Emanuel, R. E., & Vose, J. M. (2016). The influence of watershed characteristics on spatial patterns of trends in annual scale streamflow variability in the continental U.S. Journal of Hydrology (Amsterdam), 540, 850–860. https://doi.org/10.1016/j.jhydrol.2016.07.006

Riggs, G.A., Hall, D. K., & Roman, M. O. (2017). Overview of NASA's MODIS and Visible Infrared Imaging Radiometer Suite (VIIRS) snow-cover Earth System Data Records. Earth System Science Data, 9(2), pp.765–777. doi:10.5194/essd-9-765-2017.

Rittger, K., Raleigh, M. S., Dozier, J., Hill, A. F., Lutz, J. A., & Painter, T. H. (2020). Canopy adjustment and improved cloud detection for remotely sensed snow cover mapping. Water Resources Research, 55, e2019WR024914. https://doi.org/10.1029/2019WR024914

Shen, C. (2018). A transdisciplinary review of deep learning research and its relevance for water resources scientists. Water Resources Research, 54, 8558–8593. https://doi.org/10.1029/2018WR022643

Stewart, I., Cayan, T., & Dettinger, D. (2004). Changes in snowmelt runoff timing in western North America under a `business as usual' climate change scenario. Climatic Change, 62(1-3), 217–232. https://doi.org/10.1023/B:CLIM.0000013702.22656.e8

Sturm, M., & Wagner, A. (2010). Using repeated patterns in snow distribution modeling: An Arctic example. Water Resources Research, 46(12), N/a. https://doi.org/10.1029/2010WR009434

Thapa, S., Zhao, Z., Li, B., Lu, L., Fu, D., Shi, X., Tang, B., & Qi, H. (2020). Snowmelt-Driven Streamflow Prediction Using Machine Learning Techniques (LSTM, NARX, GPR, and SVR). Water (Basel), 12(6), 1734. https://doi.org/10.3390/w12061734

Tolson, B. A., & Shoemaker, C. A. (2007). Dynamically dimensioned search algorithm for computationally efficient watershed model calibration. Water Resources Research, 43(1). https://doi.org/10.1029/2005WR004723

Wang, X., & Xie, H. (2009). New methods for studying the spatiotemporal variation of snow cover based on combination products of MODIS Terra and Aqua. Journal of Hydrology, 371(1), 192-200. https://doi.org/10.1016/j.jhydrol.2009.03.028

Wood, E. F., & Hebson, C. S. (1986). On Hydrologic Similarity: 1. Derivation of the Dimensionless Flood Frequency Curve. Water Resources Research, 22(11), 1549–1554. https://doi.org/10.1029/WR022i011p01549

Woodruff, C. D., & Qualls, R. J. (2019). Recurrent snowmelt pattern synthesis using principal component analysis of multiyear remotely sensed snow cover. Water Resources Research, 55. https://doi.org/10.1029/2018WR024546

Chapter 5: Expansion and Sensitivity of the Spatio-Temporal Model of the Recurrent Pattern of Snowmelt over the Snake River Basin with a Principal Component Analysis

Introduction

Snow is an important component of water management world-wide. In the Western United States, it has been estimated that 50-80% of the streamflow is from snowmelt (Stewart et al., 2004). The amount of water contained in the snowpack, or snow water equivalent (SWE), is the most descriptive variable of water availability. Representing SWE has proved difficult, as it is spatially heterogenous. In a study over the upper portion of the Yukon River Kasurak et al. (2007) found that only 50% of the spatial variability of snow depth, and consequently SWE was represented using a complex hierarchical linear spatial mixing model. This study included two years of SWE measurements at 215 sites and 3924 measurements. The spatial heterogeneity of SWE has increased complexity under climate change. An example of this complexity is the declining snowpack in the Cascade Mountains which has long been accepted Mote (2003). Barry & McDonald (2013) demonstrated that the origin of this decline may be an interaction between climate cycles and climate change in the Washington Olympics and Cascades using snow course data. This combination of uncertainty, importance, and heterogeneity marks the importance of understanding and accurately modeling the snowmelt runoff process.

Understanding and accurately modeling these processes in a data rich world can be benefited using Artificial intelligence (AI). (Shen 2018) overviewed the current state of hydrologic modeling stating the use of AI is a necessary advancement. Resistance to this in the hydrologic community has likely been the result of a desire to understand why a system is behaves the way it does. A potential area of interest is pattern recognition, which unites understanding why a system behaves the way it does and AI. The use of pattern recognition in remote sensing is widespread. Pasquale et al. (2014) used a pattern recognition algorithm to identify riverbed forms with terrestrial photographs. Guevara et al. (2021) applied pattern recognition to gap-fill soil moisture and increase the spatial resolution of the European Space Agency Climate Change Initiative soil moisture dataset. Snow has long been noted as having spatial patterns (Adams, 1976; König & Sturm, 1998; Luce & Tarboton, 2004; Sturm & Wagner, 2010; Wang & Xei, 2009). Parr et al., (2020) demonstrated that even redistribution of snow by wind forms patterns predetermined by the landscape. Woodruff & Qualls (2019) developed a model of the recurrent pattern of snowmelt and used it to interpolate cloud covered pixels. However, patterns exist across many disciplines including snow hydrology, but often these patterns are used as

methods to infill data. However, patterns simplify complex problems. AI produces some of the most accurate snowmelt runoff modeling and relies on patterns in data which we as scientists fail to represent in our models.

Remote sensing has been used in operational snowmelt runoff modeling for many years (Rango, 1988). Hesitation due to the quality of remote sensing has been widespread. Compared with the highly accurate point measurements of SWE, remote sensing offers lower quality of data. Andreadis & Lettenmaier (2005) compared the output of the VIC model snow location versus the moderate resolution imaging specroradiometer (MODIS) pixels and reported agreement only 75.2-84.8% of the time. A mismatch of data type and spatial extent exists in the comparison. Furthermore, using the point locations a model has been calibrated to and comparing point accuracy to spatial remotely sensed pixels is inappropriate. A fair comparison would be to calibrate the model with the remotely sensed imagery as well. Anything less introduces data bias.

The MODIS sensor collects daily world-wide snow-covered area (SCA) data at a spatial resolution of 500 meters and has shown 93% accuracy with ground verification on cloud free days (Hall & Riggs, 2007). The difficulty with using this data for snowmelt runoff modeling is that cloud cover is extensive during the melt period. This data loss is compounded with issues related to topography, viewing angle, illumination, and vegetation (Riggs et al., 2017). Significant research has been invested in cloud removal, and in 2021 NASA released a cloud free dataset which uses a temporal filtering interpolation scheme to infill cloud covered pixels (Hall et al., 2019). Even though cloud cover is a significant issue, inclusion of MODIS data in snowmelt runoff models has increased streamflow accuracy. Nourani et al. (2021) tested different calibration techniques for the Snowmelt Runoff Model using MODIS as SCA input noting validation R^2 values of 0.66 and 0.8 over the Aji-Chay River in Northern Iran. Siemens et al. (2021) used the SRM model to simulate runoff under climate scenarios and found during the calibration and validation period of 2000-2010 Nash-Sutcliffe Efficiencies of 0.822 to 0.923 over the Athabasca River Basin. MODIS is especially useful in ungauged watersheds. Qiu et al., (2014) applied the SRM model with MODIS data over the ungauged Lhasa River basin and reported streamflow simulation R^2 values of 0.86 and 0.87 for calibration and validation respectively over 2002-2003.

Overall, MODIS data can help with accuracy when modeling snowmelt runoff. With MODIS we can also extract patterns. Woodruff & Qualls (2019) extracted the recurrent pattern of snowmelt over the Upper Snake River Basin and applied the model to cloud removal, reporting spatial accuracies of 84.9-97.5% when compared to two independent years of MODIS data. They termed this

model the principal component analysis (PCA) model. This novel approach joined the practicality of patterns with the large amount of data available with MODIS. In the context of snowmelt runoff modeling, a spatial pattern simplifies representation of snow depletion in space and time. In this work we further analyze the accuracy and scaling requirements of the methods developed by Woodruff & Qualls (2019) over larger basins.

The objectives of this research can be summarized with four points. One, determine how many years are required to develop a robust PCA model of the recurrent pattern of snowmelt. Two, develop PCA models for large watersheds testing their accuracy against cloud free data, and analyze whether accuracy is lost at the sub-basin scale when area is increased. Three, develop a method for determining whether two watersheds can be grouped into a single PCA model. Four, develop relationships between ground-based data and the PCA model. These objectives directly address significant remaining questions about the nature, expansion, accuracy, and development requirements of the PCA model. With this groundwork laid, expansion of this model and use within snowmelt runoff models can be accomplished with confidence.

Study Site and Data

Study Site

The study site includes seven watersheds, which together cover the Upper and Middle Snake River Basins (Figure 5.1). The watersheds cover a total area of 279,469.88 square kilometers. All seven watersheds are at the Hydrologic Unit Code (HUC) 6 size. The Snake Headwaters and the Upper Snake make up the Upper Snake Basin, shown in blue Figure 5.1. The remaining five watersheds include the Middle Snake Boise, Middle Snake Powder, Salmon, Clearwater, and the Lower Snake; these make up the Middle Snake Basin, shown in red in Figure 5.1. The Middle Snake Boise is the largest area at 85,150.16 km^2, and the Middle Snake Powder is the smallest at 10,645.52 km^2. These watersheds cover a variety of topography and snow conditions. Many of these watersheds do not receive complete snow coverage in every year. The Boise River is a sub-basin within the Middle Snake Boise and is comparable in size and snow coverage conditions to the area used by Woodruff & Qualls (2019). Also shown in Figure 5.1, are three SNOTEL locations within the Salmon watershed. Bear Basin is located at 1631 meters in elevation, Deadwood Summit at 2566 meters, and Morgan Creek at 2316 meters. Data from 2010-2020 was downloaded for all three SNOTEL sites.

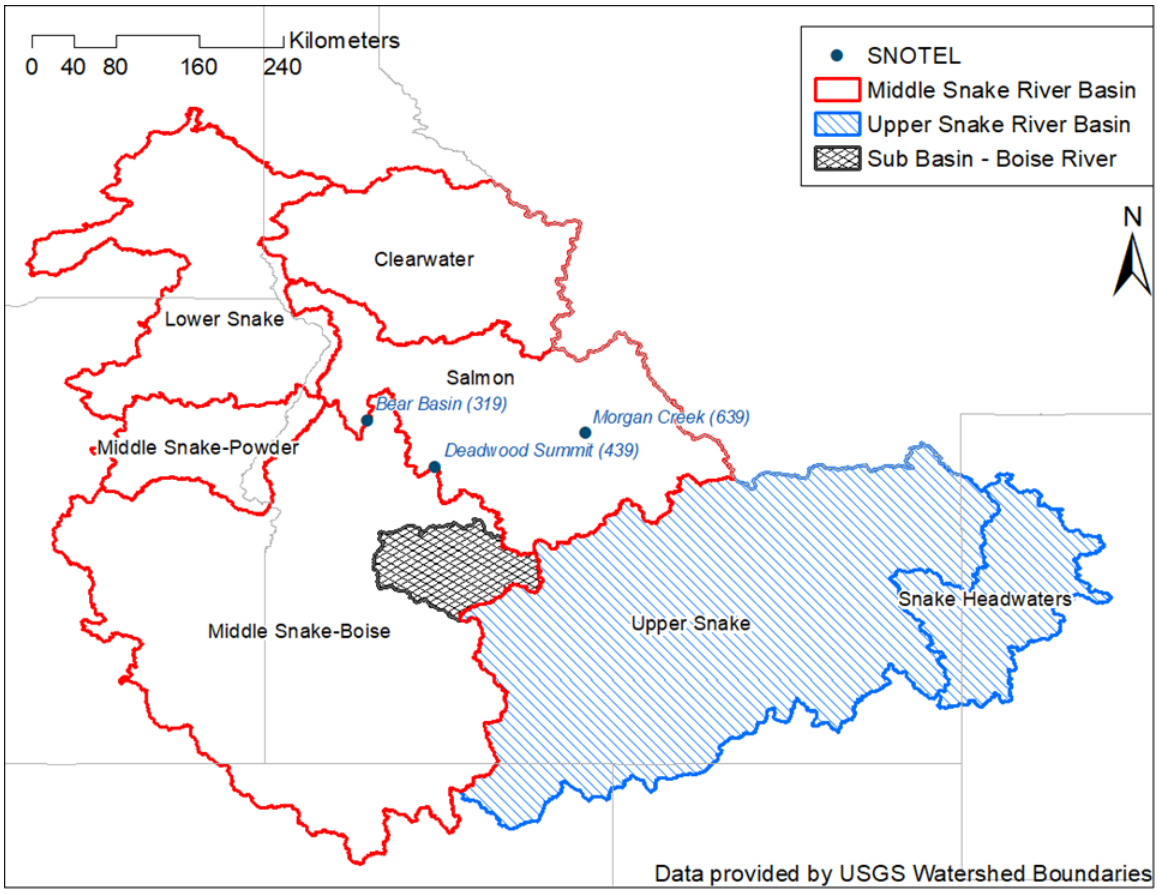

Figure 5.1: Study site with HUC-6 boundaries. Middle Snake River Basin HUC-6 boundaries are shown in red. The Upper Snake River Basin HUC-6 boundaries are shown in blue. The Boise River watershed, shown in black, is a sub basin within the boundary of the Middle Snake-Boise watershed. Watershed names are also shown. Three SNOTEL locations within the Salmon watershed are also shown.

Data Sources

The Moderate Resolution Imaging Spectroradiometer (MODIS) is onboard the Terra and Aqua satellites. Both MODIS sensors can be used; however, one of the Aqua satellite sensor bands failed and even after the algorithm was restored, the commission errors for this product are larger than the Terra satellite (Hall et al., 2019). We use the Terra satellite MODIS data product from the version 6 dataset. The NDSI snow cover data product is used for all the analyses. The MODIS h09v04 and h10v04 swaths are required to cover the study site, and all available daily imagery was downloaded for the period of 2000-2020. No cloud removal was conducted. A NDSI snow cover value of 10-100 was used to represent snow and 0-9 to represent snow free. All imagery was used in model development regardless of cloud cover, but only cloud free (<10% by area) imagery was used for validation.

Methods

PCA Model Methods

A fundamental component of the analysis to follow is the data pre-processing and derivation of the PCA model. These methods are outlined in full in Woodruff & Qualls (2019); however, for clarity a brief explanation is presented. The development of the PCA model requires two steps. One, consolidation of the MODIS daily imagery into First Day of Land (FDL) images. Second, the FDL images are the ingested into a principal component analysis.

Derivation of the FDL images is completed one year at a time. All the available MODIS data is iterated through and the first day land is seen for each pixel is stored in the FDL image. Through this preprocessing, each year's melt information is consolidated into a single image. Woodruff & Qualls (2019) used FDL images from 2000-2016 to develop their PCA model. We develop our PCA models using the same number of years unless otherwise noted i.e., selection of the minimum number of years.

FDL images are then transformed from their gridded data structure to a matrix. Within this matrix, a row contains all the FDL value for one pixel. A column contains all the FDL values for a year. A principal component analysis is applied. The results are eigen values and vectors. Woodruff & Qualls (2019) demonstrated the spatio-temporal recurrent pattern of snowmelt is extracted by the first Eigen Vector or principal component. This is used to linearly transform, through matrix multiplication, the FDL data into one resulting vector. This vector is then replotted into the grid format and is termed the "PCA model".

Selecting Minimum Number of Years

To identify the minimum number of years necessary to derive a robust spatio-temporal model of the recurrent pattern of melt, we implement a monte carlo simulation. We consider the model derived using 17 years to be the best model, which we will refer to as PCA_{best}. This assumption is reasonable, given the influence of cloud and the necessity to discard this information in the derivation of the model. We develop a PCA model for combinations of 3 years, 4 years, 5 years and so on up to 16 years with the FDL images. We define the number of years used to develop a PCA model as Q. We identify the smallest combination of years required to develop a robust model by sampling from all possible combinations. A random sample (N) consists of 10% of the total number of possible combinations up to 100 combinations and at least 17. For example, for a Q of 3 years a total number of possible combinations is 680. Our random sample size N equals 68. The random samples

determine which years (FDL images) are used to develop the PCA model. The PCA model vector output of each is saved along with the years used.

The random sampling of years used for each PCA model allows us to assess the variability in the results for a given *Q*. The metric used to determine the quality of the PCA model is the correlation of the PCA_{best} with the PCA model for a given *Q* within the sample set *N*. Correlations are used because they capture the similarity of the pattern. This mirrors the application of factor loadings in PCA analysis (Jensen, 2016).

We record descriptive statistics about each correlation for a given *Q*. In the case of *Q* equal to 3, our sample size *N* is 68. There is a total of 68 PCA models generated all with different years used. A correlation is calculated for each PCA model against PCA_{best}. The maximum, minimum, average, and standard deviation of these correlations is calculated once all 68 models have been developed. With these values recorded, we can select a good practice number of years required to develop a robust PCA model for the watershed analyzed.

Determining Spatial Extent

The PCA model method for extracting the recurrent pattern of snowmelt has only been published for the Snake Headwaters with an area of 8,894 km^2. This large watershed records complete snow coverage in every year. Applying the method to a watershed which does not always receive 100% snow coverage introduces a new source of variance. The HUC-6 boundaries produced by the United States Geological Survey offer a variety of topographic variance and a variety of snow coverages over 2000-2016. We use these HUC-6 boundaries to develop PCA models of the recurrent pattern of melt. HUC-6 boundaries vary significantly in area (Figure 5.1). Martinec et al. (1983) stated the SRM model has been tested without issue on watersheds ranging in size from 2.65 km^2 to 4000 km^2 and at sizes larger than this sparse meteorological data reduced modeling accuracy. Many macro-scale hydrologic models operate at watershed sizes larger than 4000 km^2. The VIC has been widely tested at large scales (Demaria et al., 2007; Haddeland et al., 2002; Troy et al., 2008), however the data used to run these models varies across space allowing it to adapt to the region. As we are developing a watershed specific snowmelt pattern model, we must rely on snow water equivalent trends to guide size parameters at first pass. Mote (2003) demonstrated there are varied trends in Snow Water Equivalent across Idaho. For this reason, we use the HUC-6 boundaries.

Two questions are addressed in the spatial extent sensitivity analysis. One, is the HUC-6 size an applicable size for applying this method. Two, can the recurrent pattern of snowmelt be extracted

for watersheds that do not receive complete snow coverage in each year. Both questions require development of the PCA model using the FDL images for 2000-2016. The accuracy of a PCA model is calculated by comparing it against cloud free (<10% cloud cover by area) MODIS images. To calculate accuracy a fitting algorithm must be completed to determine the spatial coverage of snow as described by the PCA model. A PCA model is comprised of unique values for each pixel. Converting the PCA model to a binary snow and no snow image requires selection of a threshold, t^*. This threshold identifies the PCA value used to split the pixels into either snow or no snow. A characteristic of the PCA model is the values are ordered in terms of their *relative melt timing*. Because of this, selection of t^* allows us to represent SCA on a given day. We select t^* by optimizing the *VPE* (equation 5.1) following the methods of Woodruff & Qualls (2019).

Equation 5.1

$$VPE = \sqrt{\frac{{I_l}^2 + {I_s}^2}{T_p}}$$

Optimizing the VPE is done by first converting the model to a snow and no snow image by selecting a t^*. The binary model representation is then directly compared against a cloud free MODIS image. For the t^* used we calculate I_l, the number of incorrectly modeled land or snow free pixels, I_s, the number of incorrectly modeled snow pixels, and the total number of visible pixels in the MODIS image. The t^* is selected to optimize the *VPE*, which produces the best fit PCA model representation of SCA for that MODIS image. Once the best fit t^* is selected we calculate the spatial accuracy by equation 5.2. All cloud free daily MODIS images from 2017-2020, independent years, were used to calculate spatial accuracy for all 7 watersheds (Figure 5.1).

Equation 5.2

$$Accuracy = \left(1 - \frac{I_l + I_s}{T_p}\right) \times 100\%$$

The applicability of the HUC-6 size for a PCA model is determined by calculating the PCA model for all seven watersheds (Figure 5.1). Each PCA model is calculated with FDL images from 2000-2016, and the accuracy of each model is found using cloud free images from 2017-2020. All cloud free images from the melt period were used to calculate accuracy excluding the accumulation phase.

The second question is addressed by comparing the PCA model for the Middle Snake-Boise (MS-Boise) against the PCA model for the Boise River sub-basin (Figure 5.1). A PCA model is

developed for the Boise River with FDL images from 2000-2016. The PCA model for the MS-Boise is clipped to the Boise River watershed boundary. The MS-Boise does not record complete snow coverage and includes a large valley. The Boise River sub-basin records complete or nearly complete snow coverage between 2000-2016. We directly compare the PCA model results of the clipped MS-Boise with the Boise River sub-basin. A plot is presented of the values contained in each model and correlations are given. The correlation describes the similarity of the melt timing of each pixel specifically the t^*, which is simply the similarity of the pattern.

Identifying Ideal Groupings

A final question we seek to address in this article is whether any theoretical boundaries exist between melt rates of adjacent watersheds. If the melt ratio of the total snow accumulation between two watersheds varies from one year to another, one might expect the relative timing of melt between the two watersheds to differ from year to year. In this case, the PCA model should be synthesized separately for the two watersheds. This separation is fundamental to the recurrent pattern method. Areas which melt asynchronously with respect to one another across years are distinct in their snowmelt timing. The goal of this analysis is two parts: determine the boundaries using remote sensing and develop a ground-based relationship which can be used in the future to identify areas which can be grouped.

The t^* values move linearly with time. This is an outcome of the linear transformation used by a principal component analysis. If we plot the t^* values selected for all the cloud free MODIS images within a year we can fit a linear regression and determine the slope or rate of melt (S). The rate of melt S is simply the change in t^* over the change in time, t. To determine whether two watersheds should be grouped, we compare S for multiple years (2017-2020). With slopes for watershed A and watershed B, we calculate S_i equation 5.3. For a given year we divide S_A by S_B. We use 2017-2020 and therefore we have four values of S_i. If two watersheds can theoretically be grouped together, they must satisfy two constraints. One they must be spatially contiguous. Two, they must produce an S_i of greater than one in every year of less than one in every year. If S_i varies from greater than one to less than one, then the watersheds do not melt in parallel with one another. As we are determining the largest size, we can group we will not conduct any of these analyses on watersheds smaller than the HUC-6 size.

Equation 5.3

$$S_i = \frac{\Delta t^*_A / \Delta t}{\Delta t^*_B / \Delta t}$$

Determining this relationship prior to developing a PCA model must rely on the ground-based SNOTEL data. Let us first identify the variable from the ground-based SNOTEL data that is of greatest importance to this analysis: melt out timing. The spatio-temporal characteristic of the PCA model requires a ground-based verification which indicates a time and space dependent change. Changes in the *z-direction* of snow depth or SWE only describe snow presence when comparing SCA. The current validation methods apply a snow or snow free comparison for pixel to ground-based data (Dong & Menzel, 2016; Parajka & Blöschl 2006; Klein & Barnett, 2003). While this method is applicable for validation of snow presence, melt out date describes a point in time as well as a spatial value. This approach assumes the melt out date is associated with a given SCA rather than a given pixel. We can simplify this comparison further by relating the linear *t** values with time instead of the non-linear SCA.

To develop this relationship more data is necessary than 2017-2020. We use cloud free MODIS data from 2010-2020 for the Salmon watershed. A linear regression is applied to the *t** values and dates for the cloud free MODIS images for each year. The linear regression is necessary to interpolate the *t** values for dates without a cloud free MODIS image. The melt out dates for three SNOTEL sites (Figure 5.1) are recorded for 2010-2020 and *t** values can be calculated. We then use a two-tailed paired t-test to determine whether these *t** values are significantly different from one another assuming an alpha of 0.05. Demonstrating order in melt out timing related to the *t** values suggest that melt out timing alone can be used to identify which areas can be grouped.

One consideration for completing this analysis is the Salmon is large and encompasses a significant variation in elevation and snowpack. This leads to a condensed representation of the SNOTEL melt out versus *t**. The PCA model developed for sub-basins offers greater distinction among *t** values for melt out timing. In our case the large number of SNOTEL stations in the Salmon and relatively small slice of *t** values that are associated with representing the melt out dates crowds the analysis. In an operational setting the ability to determine which areas can be grouped with less data is meaningful. We use only three SNOTEL stations spread across melt timing: first to melt, middle melt, and last to melt. This data can be gathered from the SNOTEL site. The purpose of this analysis is to develop a relationship that can be used before the PCA model is derived. Establishing

this is the starting point, and further investigation will be necessary to determine whether this is a viable method to group watersheds.

Results

The results are presented in the following format. First, we present the total number of years necessary to develop a robust PCA model of the recurrent pattern of snowmelt for the Boise River sub-basin. Second, the PCA model is applied to all seven HUC-6 watersheds and is verified for accuracy against four independent years. Third, we determine whether the resulting PCA model for a sub-basin is changed by including a larger area that does not receive complete snow coverage. Lastly, we present a method for determining which watersheds can and cannot be grouped, and a ground-based relationship for determining groupings is also derived.

Determining Number of Years

The number of years required to develop a robust PCA model is of significant interest as it could reduce processing time while also increasing the number of independent years for model validation. We use the Boise River sub-basin (Figure 5.1, shown in black) to conduct this analysis as it is nearly equal in size to the study site used in Woodruff & Qualls (2019). A PCA_{best} is developed using all FDL images from 2000-2016. Combinations, Q, of 3-16 were tested as potential combinations to develop a robust PCA model. For a given Q, a sample of the total number of possible combinations is taken and a PCA model is developed for each of the sampled combinations using the FDL images. The correlation of a single sampled PCA model is calculated against PCA_{best}. A correlation is calculated for all PCA models developed within a sample. The minimum (red X), maximum (hollow black square), and average (solid blue dot) correlations are plotted versus Q in Figure 5.2.

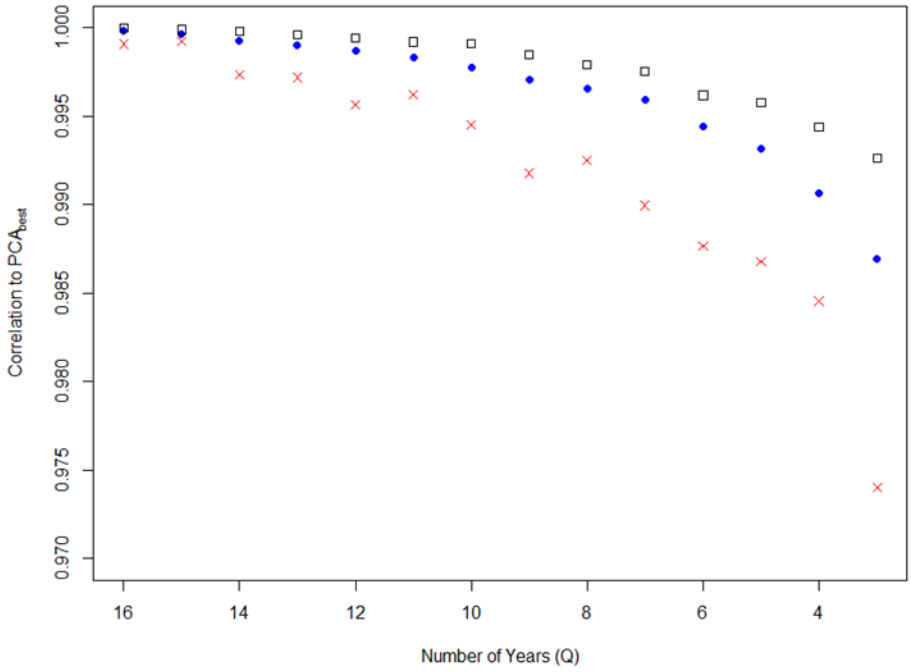

Figure 5.2: Correlations of PCA models versus PCA_{best} plotted against Q varied from 16 to 3. Maximum correlation for a given Q is given by black squares, average correlation is given by blue circles, and the minimum correlation by the red "X".

Figure 5.2 clearly illustrates as *Q* decreases so does the correlation of PCA models with PCA_{best}. For *Q* between 16 and 10 the correlations are all nearly equal. For *Q* less than 10, the minimum correlation drops dramatically and continuously. While the average and maximum correlations remain high for all values of *Q*, between 0.985 and 1, the minimum correlations drop below 0.975 at a *Q* of 3. It is important to recognize the correlations plotted in Figure 5.2 are all exceptional; however, with this large dataset a small change in correlation could indicate significant changes in the *relative melt timing* of individual pixels. The pattern is simply the *relative melt timing* of each pixel, and a small change in timing may lead to larger decreases in spatial accuracy when compared against independent cloud free MODIS data.

The results plotted in Figure 5.2 suggest a *Q* of greater than 3 may adequately extract the pattern with decreased accuracy. A more compelling representation of the stability of the models developed with a varied *Q* can be shown by representing the standard deviation. We plot the theoretical normal distribution defined by the average and standard deviation of the correlations for each *Q* in Figure 5.3.

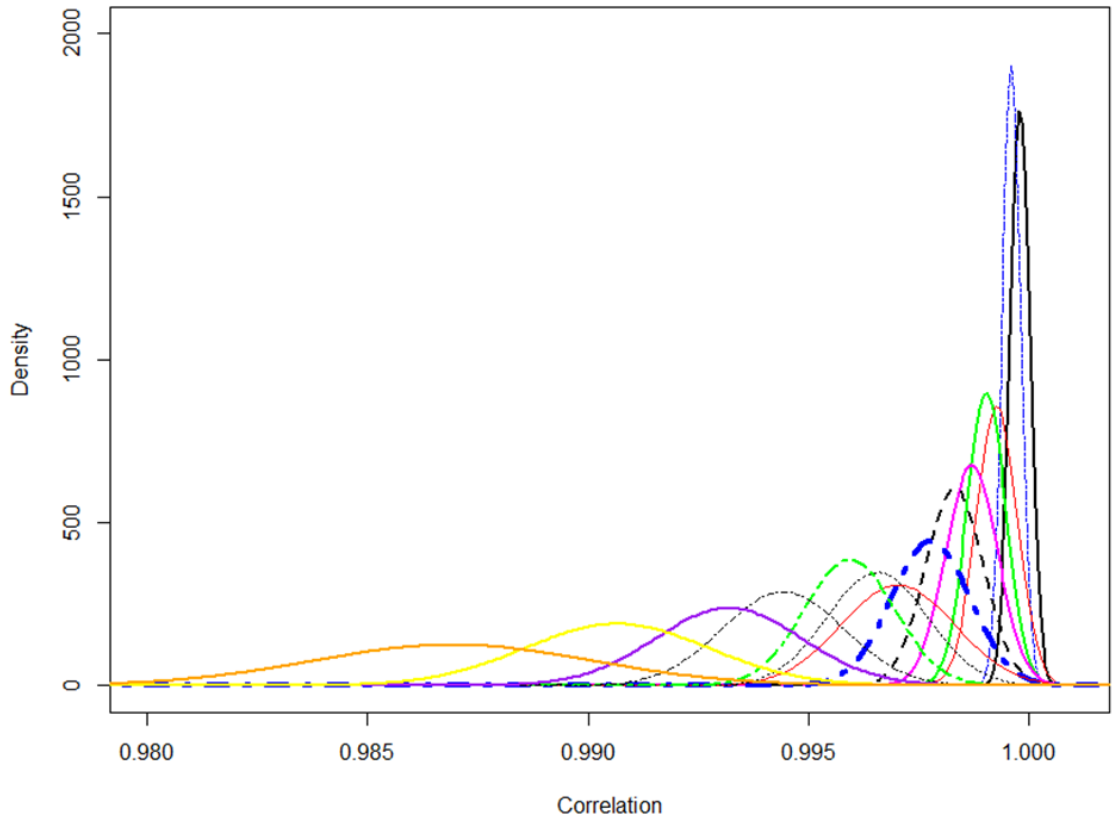

Figure 5.3: Theoretical normal distributions for varied Q. Each value of Q is represented by a single line. A Q of 16 years is given as a thick black line, 15 a blue two dash line, 14 solid red line, 13 solid green, 12 solid magenta, 11 dashed black, 10 heavy dot dashed blue, 9 thin solid red, 8 dotted black, 7 two dashed green, 6 dot dashed black, 5 solid purple, 4 solid yellow, and 3 solid orange.

There is significant degradation in the output of the PCA model with *Q* less than 10 in Figure 5.3, given as the heavy dot dashed blue line centered around 0.9975. An ideal resulting normal distribution in Figure 5.3 is tall and narrow centered very close to a correlation of one. This would indicate we are producing the same PCA model with every sampled combination for that *Q*. As the distribution decreases in height and flattens, the confidence that you will produce the same PCA model with any combination decreases. Every combination greater than 10 produces a tall narrow theoretical normal distribution. For the Boise River sub-basin, we can conclude at least 11 years, shown as the dashed black line, is necessary to develop a robust PCA model. A *Q* of 10 or less can be used to develop a PCA model; however, the model may contain more error and it may fluctuate depending on the years used in the combination than one developed using a *Q* of greater than 10. This analysis offers insight into this specific watershed; however, a good practice for developing the PCA

model would be to use all the years possible. The source of this variability in the PCA model output is undetermined at this time, although it may be due to cloud influence in the FDL images. Potentially, a critical minimum number of years is necessary to extract the pattern and discard the influence of cloud. For this watershed it is 11.

Determining Spatial Extent

Snake River Basin PCA Models

The PCA model was developed for all seven HUC-6 watersheds in the Upper and Middle Snake River Basins across Idaho. The PCA models are presented in Figure 5.4. An important consideration in visually analyzing these models is each PCA model was developed independently for each watershed. This means that early melt (black) in one watershed does not indicate the same time of melt in another watershed. These models are to be analyzed separately. This is best described by the two watersheds in the Upper Snake River Basin (blue). We can see that the Snake Headwaters (smaller watershed) has a black area in the center which is early to melt. The Upper Snake (larger watershed) is dominated by a valley floor which appears to melt from west to east with the eastern portion melting later (lighter grey pixels). The lighter eastern portion of the Upper Snake in fact melts before the black pixels in the Snake Headwaters. This points out why these PCA models cannot be interpreted as continuous across watershed boundaries.

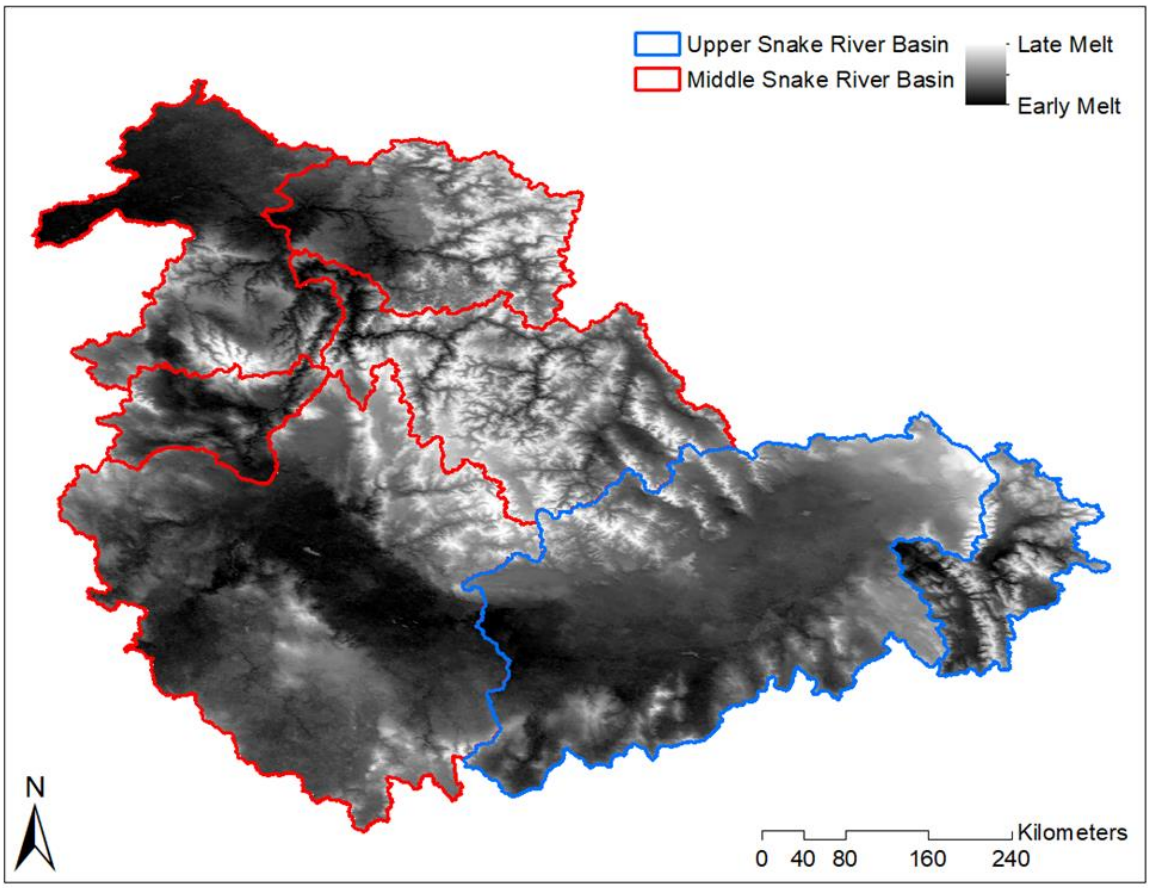

Figure 5.4: PCA models for the seven HUC-6 watersheds in the study site. Each PCA model is independent of one another. Black areas within a watershed boundary melt earliest within that boundary and white pixels melt latest. The values are not continuous across watershed boundaries.

We can note some interesting characteristics of the watersheds in Figure 5.4. The Salmon watershed has extremely varied and well-defined melting behavior, likely due to the elevational changes and consistent snowpack in this mountainous area. In the MS-Boise we see a more subtle description of melting where the Boise River Mountains in the Northeast melt latest, but there is a more mottled melt appearance in the south of the watershed. These characteristics may be attributed to elevation, slope, aspect, vegetation, and accumulation. Each watershed carries its own characteristic melt pattern.

Snake River Basin PCA Model Accuracy

The PCA models shown in Figure 5.4 were validated for spatial accuracy against cloud free MODIS images from four independent years (2017-2020) using equations 5.1 and 5.2. Spatial accuracy was considered only during the melt period and excluded any significant accumulation events after the watershed reached SCA of 0%. Table 5.1 presents the minimum, maximum, and

average spatial accuracy (equation 5.2). Overall spatial accuracies are exceptional. Average spatial accuracies ranged from 96.95% (Salmon, 2019) to 99.58% (Lower Snake, 2017). Maximum spatial accuracies were 100% in many cases and minimum spatial accuracy ranged from 72.94% (MS-Boise, 2017) to 98.88% (Lower Snake, 2017). In fact, only three minimum spatial accuracies were below 90%, shown in red. The lowest spatial accuracy of 72.94% can be attributed to a secondary snowfall event which traveled through the valley of the MS-Boise depositing snow erratically across the valley floor. Once this melted, spatial accuracies returned to the 90% range.

Table 5.1: Spatial accuracies by HUC-6 PCA models are given. Minimum, maximum, and average spatial accuracies calculated for cloud free data over the independent period of 2017-2020 are given by year.

Watershed		*2017*	*2018*	*2019*	*2020*
Clearwater	Min	95.36	95.74	95.32	94.22
	Max	100.00	100.00	100.00	99.96
	Average	**99.10**	**99.25**	**98.05**	**98.04**
Lower Snake	Min	98.88	95.40	98.56	95.37
	Max	99.92	100.00	100.00	99.94
	Average	**99.58**	**99.44**	**99.58**	**98.86**
Middle Snake Boise	Min	72.94	95.59	89.86	94.44
	Max	99.99	100.00	100.00	100.00
	Average	**98.93**	**99.39**	**98.19**	**99.08**
Middle Snake Powder	Min	98.68	93.76	92.22	96.71
	Max	99.89	100.00	100.00	99.94
	Average	**99.52**	**99.35**	**98.69**	**99.04**
Salmon	Min	93.38	93.72	94.19	92.72
	Max	100.00	99.98	100.00	99.99
	Average	**97.39**	**97.65**	**96.95**	**97.55**
Snake Headwaters	Min	93.55	93.53	94.65	94.15
	Max	100.00	100.00	100.00	100.00
	Average	**98.02**	**98.52**	**99.09**	**99.00**
Upper Snake	Min	88.60	91.98	92.82	90.67
	Max	99.92	99.98	99.95	99.98
	Average	**98.44**	**98.98**	**97.90**	**98.56**

The PCA Models represent snow depletion with exceptional spatial accuracy over all seven watersheds when compared against independent cloud free MODIS data. The PCA method accurately extracts the recurrent pattern of snowmelt for each watershed. The HUC-6 size is handled with ease

by the PCA method. The variation in topography, accumulation of snow, and melt timing does not impede the ability of the PCA method to extract the recurrent pattern.

Incomplete Snow Coverage Impacts on Spatial Model

The cloud removal results show the model accurately extracts a robust spatial pattern of snowmelt. A remaining question for water management is does inclusion of areas which do not receive complete snow coverage reduce the spatial accuracy of the PCA model. Snowpack accumulates and persists with regularity in the mountainous areas in Idaho but is ephemeral in the lower elevations. The MS-Boise is a suitable watershed to address this question as it contains a massive area which does not receive complete snow coverage in each year. This could potentially lead to noise in the FDL images used to develop the pattern thereby reducing the ability of the principal component analysis to extract the recurrent pattern. We approach this problem by analyzing the PCA model developed for the mountainous Boise River sub-basin (Figure 5.1) two ways. First, we develop the PCA model for the entire MS-Boise and clip the model to the Boise River sub-basin. Second, we develop the PCA model for the Boise River sub-basin. PCA models for both watersheds are produced using the FDL images from 2000-2016. These models are compared.

The results of the PCA models are shown in Figure 5.5. The PCA values contained in the MS-Boise clipped to the Boise River are plotted against the PCA values of the Boise River model. These values describe a pixel's *relative melt timing*. A difference between the two models in a pixel's value indicates the pixel's relative melt timing is very different between the two models. If both models are equal, we can expect a perfect 1:1 line. This would indicate the relative timing of melt of each pixel is the same in both models. We see a nearly perfect 1:1 line in Figure 5.5. Even more interesting is the range of values has not changed. The values of -100 are the first pixels to melt. The early stages of melt from -100 to -300 are slightly scattered about the 1:1 line. After this brief scatter nearly all the pixels are equal from -300 to -750. The overall correlation of these values is 0.9999. Inclusion of the lower elevation areas in the MS-Boise PCA model has not changed the representation of melt timing the Boise River sub-basin.

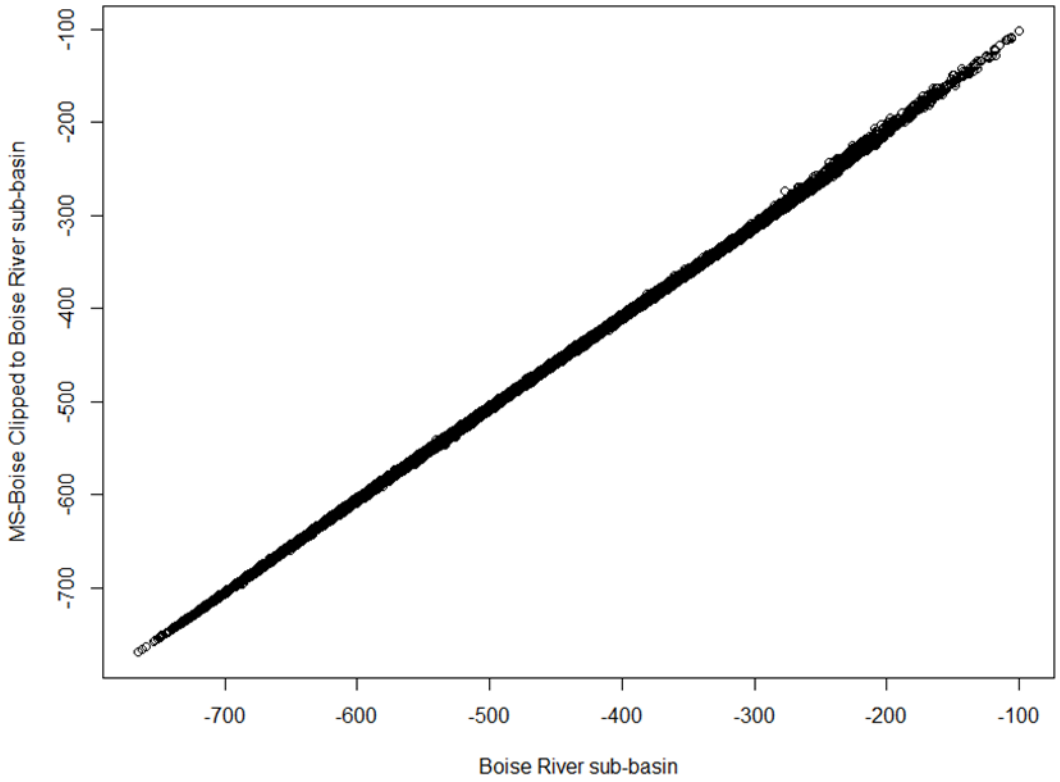

Figure 5.5: PCA values for the MS-Boise PCA model clipped to the Boise River sub-basin are plotted against PCA values for the PCA model developed for the Boise River sub-basin. A 1:1 line indicates the values have not changed. Individual points are plotted as hollow black circles.

Determining Ideal Groupings

Using t* to Determine Ideal Groupings

Thus far we have shown the HUC-6 watershed boundary is an applicable watershed size; however, we have not developed any methods for determining which watersheds should be grouped. We can identify groupings through equation 5.3. The rate of melt in one watershed compared with another should produce a stable S_i over multiple years if these areas can be grouped into a single PCA model. Using cloud free imagery from 2017-2020 we fit a linear regression to the t^* values plotted with time for each year for the Salmon, Snake Headwaters, Upper Snake, and Clearwater watersheds. The comparison of slopes is given in Table 5.2 by year. We also suggested a constraint that only contiguous areas can be joined into one PCA model. These areas are not all contiguous, but comparison shows the strength of the method to determine which areas can be joined. The sign of the t^* values is arbitrary.

From Table 5.2, the Salmon and Snake Headwaters exhibit the most similar melt behavior of all the pairs. From 2017-2019 S_i is all less than -1, however in 2020 it is greater than -1. This shows these watersheds do not melt in parallel with one another in every year and should not be grouped. The comparison of the Upper Snake to the Snake Headwaters also indicates these watersheds should not be grouped; however, we can note the spread in values of S_i are larger for this comparison than for the Salmon versus the Snake Headwaters. The same is true for the Salmon versus the Upper Snake. Both watersheds are contiguous with the Upper Snake. The larger and more widespread snowpack the Salmon and Snake Headwaters leads to a more similar S_i than the comparison of one of these watersheds versus the lower elevation Upper Snake. The lack of consistent snow coverage could explain why the Upper Snake watershed should be analyzed separately from the Salmon and Snake Headwaters. The Clearwater and the Salmon although contiguous also should not be grouped. This mirrors the trends discussed in Mote (2003). Finally, the comparison of the Snake Headwaters and the Clearwater produce wildly different S_i values which is to be expected as storm tracks and accumulation trends differ greatly between these areas.

Table 5.2: Calculation of S_i for 2017-2020 for the Salmon, Snake Headwaters, Upper Snake, and Clearwater watersheds.

Watersheds Compared	*2017*	*2018*	*2019*	*2020*
Salmon/Snake Headwaters	-1.08	-1.12	-1.07	-0.94
Snake Headwaters/Upper Snake	0.95	0.84	1.28	0.89
Salmon/Upper Snake	-1.02	-0.94	-1.37	-0.83
Salmon/Clearwater	-0.75	-0.98	-1.08	-0.99
Snake Headwaters/Clearwater	0.70	0.88	1.01	1.06
Upper Snake/Clearwater	0.74	1.05	0.79	1.19

Table 5.2 demonstrates none of these watersheds should be grouped into a single PCA model. The HUC-6 size appears to be appropriate for the PCA models in the Upper and Middle Snake River Basins. It is beneficial from the point of view of spatially modeling snowmelt to use larger areas for one simple reason: cloud removal. Woodruff & Qualls (2019) demonstrated this method can be used for cloud removal. The larger the selected area is, the more opportunity for visible pixels on a cloudy day. For this reason, as well as the documented accuracy of the PCA model at smaller scales, we do not use the t^* slope analysis to determine sub-basin groupings.

Ground-based Method for Ideal Groupings

We have demonstrated the *t** versus time slope comparisons can be used to determine which areas can and cannot be grouped together into a single PCA model. In an operational setting this knowledge would be most useful before deriving the PCA model. To lay the foundational work for this comparison, we propose relating the *t** values with melt out dates of ground-based SNOTEL sites. The Salmon is selected for this comparison. As discussed in the methods the large watershed area and relatively small range in *t** values for SNOTEL melt out timing led us to use only three sites. These SNOTEL stations: Morgan Creek, Bear Basin, and Deadwood Summit melt out on average in the following order when compared to the other stations within the watershed (2017-2020): first, middle, and last.

The lack of cloud free days requires interpolation of *t** values to associate them with melt out date. For the period of 2010-2020 every cloud free image except for 100% snow coverage images were used to determine the linear regression model of *t** versus time. The slope and intercept for each year can then be used to interpolate the *t** value for missing cloud covered day. The slope, intercept, and R^2 values are given in Table 5.3. The R^2 values are greater than 0.9 except for 2010, which only had cloud free imagery near the end of the melting period. The melt out day of year (DOY) as measured from January 1 for all SNOTEL sites, as well as the interpolated *t** values are also given in Table 3. We perform a two-tailed paired t-test on the *t** values for each site combination. P-values of 8.08E-5, 7.03E -9, and 3.90E-8 for the comparisons of Morgan Creek to Bear Basin, Bear Basin to Deadwood Summit, and Morgan Creek to Deadwood Summit, respectively are calculated. In all three cases with an alpha of 0.05, we reject the null hypothesis that the difference in means is equal to zero. These *t** values are statistically significantly different from one another.

Table 5.3: Melt out timing of Morgan Creek, Bear Basin, and Deadwood Summit are shown for 2010-2020. The linear regression slope and intercept as calculated by the cloud free t* data for each year is shown with R^2 values. The interpolated t* values for each melt out day is also shown.

				DOY			*t**		
Year	*Slope*	*Intercept*	R^2	*Morgan Creek*	*Bear Basin*	*Deadwood Summit*	*Morgan Creek*	*Bear Basin*	*Deadwood Summit*
2010	4.8201	-183.11	**0.843**	137	154	172	477.24	559.19	645.95
2011	4.2526	-128.36	**0.958**	156	169	188	535.05	590.33	671.13
2012	3.4521	85.953	**0.950**	117	142	179	489.85	576.15	703.88
2013	3.91	54.586	**0.977**	127	131	160	551.16	566.80	680.19
2014	3.9261	10.697	**0.965**	127	143	174	509.31	572.13	693.84
2015	3.3713	158.62	**0.924**	110	121	151	529.46	566.55	667.69
2016	3.5186	98.577	**0.980**	113	136	166	496.18	577.11	682.66
2017	3.6674	28.444	**0.973**	131	148	183	508.87	571.22	699.58
2018	4.5137	-46.757	**0.970**	128	136	158	531.00	567.11	666.41
2019	4.5374	-84.581	**0.991**	118	151	174	450.83	600.57	704.93
2020	3.9765	2.052	**0.985**	125	149	166	499.11	594.55	662.15

The relationship identified in Table 5.3 demonstrates the use of melt out date as a potential substitute for *t**. A statistically significant relationship between melt out date for a SNOTEL site and the *t** values exist. We can therefore apply the melt out date as a substitute for the S_i calculations we conducted earlier. The purpose of this analysis is to develop the foundational relationships between *t** and melt out date rather than use melt out date to determine which watershed can be grouped. As we have demonstrated the HUC-6 size is the appropriate size for many of the watersheds in this study (Table 5.2).

Discussion

We have demonstrated a PCA model of the recurrent pattern of snowmelt requires several years, has size constraints, is spatially accurate at the HUC-6 size, and we have demonstrated potential methods for identifying watersheds which can and cannot be grouped through remote sensing and ground-based data. A guiding principle for this analysis, and application of the PCA model, is watershed characteristics.

The recurrent pattern is unique for each watershed and should be treated as a watershed characteristic. The process of extracting the pattern requires many years of data. There is variability in the timing of melt, secondary snowfall events, cloud cover, snow accumulation, as well as potential land cover changes due to fires or land use change. We demonstrated for the Boise River sub-basin 11 years were necessary to produce a robust and similar pattern with any potential combination of years.

For other watersheds a different number of years may be necessary. This is by no means a best practice suggestion, rather a watershed specific proof of concept. Using the methods outlined here this can be determined for any PCA model for a given watershed.

The applicable spatial extent of the PCA model was also analyzed. The HUC-6 boundaries varied significantly in area from 10,645.52 km^2 for the Middle Snake-Powder to 85,150.16 km^2 for the Middle Snake-Boise. The changes in elevation and snowfall also dramatically change over these areas. Even with all this variation, these hydrologic boundaries could be used to develop a PCA model with exceptional spatial accuracy when compared against independent cloud free MODIS data. Overall, the Lower Snake had the highest overall average spatial accuracy (99.37%), calculated as the average of the averages. The lowest overall average of four years spatial accuracy was recorded in the Salmon watershed (97.39%). For all seven basins, we demonstrated the PCA model accurately represented snow covered area with a total average spatial accuracy of 98.65%. Only four images across all 4 years for every watershed recorded a spatial accuracy of less than 90%. If this watershed size was inappropriate for developing the PCA model of the recurrent pattern of snowmelt we would not record such exceptional spatial accuracies when compared against independent data. This pattern approach is not only spatially accurate, but it contains predictive qualities for each pixel and for the time component.

The relationship between the PCA model t^* values and time is linear for the Salmon watershed. The watershed recorded the worst average spatial accuracy, but still recorded R^2 values of 0.843 to 0.991 for the period of 2010-2020. The lowest R^2 of 0.843 was recorded in 2010, which did not have any cloud free images until DOY 163 when melt was nearly finished. This value may be a spurious error due to the lack of cloud free images as all the remaining 10 years recorded R^2 values of greater than 0.92. The PCA model describes the spatial progression of snowmelt, and when associated with time it can linearly describe the rate of snowmelt. With this relationship we can effectively determine which areas can and cannot be grouped into a single PCA model.

The simplification of snowmelt into a linear description based on spatial properties is a function of the stable drivers of snowmelt. Attributes such as topography, aspect, and slope do not change (Hock, 2003). When the time component of snowmelt is added this process is made more complex, as sun angle at different times of the year fluctuates This fluctuation changes the interaction of slope and aspect in the melt process. This may appear at first glance to disagree with our linear representation of snowmelt timing; however, it suggests the melt timing is also strongly related to the spatial location of the snow. The snowline itself plays an important role in the repeatability of the

snowmelt pattern. When advection near the snowline is analyzed, increases in ablation have been recorded to increase 25-30% as demonstrated over the Dischma Valley in the Swiss Alps (Schlogl et al., 2018). In 2011, significant late snowfall occurred in the Salmon. In this case shortwave radiation is higher during melt as it began melting later in the year. Even so, we still recorded a linear progression of melt with a high R^2 of 0.958 (Table 5.3). The snowmelt pattern and snowmelt timing are not independent of one another. As we have demonstrated once snowmelt begins, the t^* values follow a linear trajectory with time. This complex process can be distilled down to a simple linear regression. Analyzing the relationship between ground-based melt out data to the t^* values is simplified because of the linear description of t^* with time. In the Salmon watershed Morgan Creek, Bear Basin, and Deadwood Summit all melt out at a given statistically significant unique t^* value each year (2010-2020). With this relationship established a formal assessment should be conducted on whether watersheds can be identified and grouped by SNOTEL melt out data alone. Further research into this area is required for seamless expansion.

Limitations

In this study we did not compare, nor attempt to group, smaller watersheds using the t^* relationships with time. The PCA model has demonstrated accuracy at smaller scales (Woodruff & Qualls, 2019). In their foundational work, a different NDSI snow cover value was used to determine snow or snow free leading to the accuracy differences reported here. There is a benefit to using larger watersheds from a management point of view as well as a cloud removal point of view. We found that anything larger than the HUC-6 size could not be grouped for the Snake Headwaters, Upper Snake, Salmon, and Clearwater watersheds. In other areas a larger size may be grouped so long as the snowmelt moves in parallel for the two watersheds. While the results of the t^* values with melt out dates of the SNOTEL stations are promising, a more in-depth analysis is required. As we include more SNOTEL sites the results may be muddied. Smaller watershed PCA models may help address this issue. We have presented a relationship and method; however, further investigation is required.

Conclusions

In this study we identified four objectives. For the first objective we determined for the Boise River sub-basin eleven years were necessary to develop a robust pattern of the recurrent pattern of snowmelt with the PCA method. Fewer years could be used; however, the consistency of the resulting model will vary by years included to develop the model. The source of this is unclear. Expansion of the PCA method should be done using as many years as possible to avoid inconsistencies and errors.

The second objective required applying the PCA method to larger watersheds and assessing the spatial accuracy of the resulting models. We applied the PCA model to seven HUC-6 size watersheds which comprise the Snake River Basin over Idaho. Areas ranged from less than 11,000 square kilometers to over 80,000 square kilometers. We found an average spatial accuracy of 98.65% when the models were compared against independent cloud free data for 2017-2020. Only four images recorded a spatial accuracy of less than 90%. We also demonstrated the PCA method extracts the recurrent pattern for sub-basins even when the larger basin is included in the analysis. The Boise River sub-basin PCA model was 0.9999 correlated with the PCA model developed for the MS-Boise clipped to the Boise River boundary. Areas which do not receive complete snow coverage in every year do not impact the integrity of the recurrent pattern of snowmelt for mountainous sub-basins.

The third objective focused on developing a method for grouping watersheds into a single PCA model analysis. We used the slope of the linear relationship between the t^* values versus time for watersheds to determine whether they melted in parallel. We demonstrated for the Snake Headwaters, Upper Snake, Salmon, and Clearwater watersheds that they could not be grouped, and the HUC-6 size was the largest grouping. If the HUC-6 size was too large we would not have calculated such high spatial accuracies as varied melt timing within sub basin in a watershed would influence the location of snow and the spatial accuracy of the independent validation set 2017-2020.

Finally, in the fourth objective we related the t^* values to melt out date of ground-based SNOTEL sites. We demonstrated each SNOTEL site over the period of 2010-2020 had a statistically significant unique t^* value associated with its melt out timing. This relationship not only can be used to potentially relate watersheds which can be grouped into a single PCA model but also serves as a spatio-temporal ground-based verification metric. If the pattern shifted within a year, the t^* values would vary for the melt out date. Although we used a linear regression to interpolate t^* values this did not force the melt out day to be associated with a given t^*.

Overall, the PCA model has demonstrated excellent spatial accuracy at the varied spatial scales described by the HUC-6 sizes over the Snake River Basin. It can be expanded with confidence by including many years, and it produces a linear description of snowmelt with time. The potential applications of this type of model are numerous including normalizing melt timing, increasing available spatial data, and potentially as an input in snowmelt runoff models. Further research is necessary to determine if larger watersheds can be grouped in different snow regimes and to identify the number of years required to develop a robust model at larger and smaller scales.

References

Adams, W. P. (1976). Areal differentiation of snow cover in east central Ontario, Water Resources Research, 12(6), 1226– 1234, https://doi.org/10.1029/WR012i006p01226

Andreadis, K. M., & Lettenmaier, D. P. (2006). Assimilating remotely sensed snow observations into a macroscale hydrology model. Advances In Water Resources, 29(6), 872–886. https://doi.org/10.1016/j.advwatres.2005.08.004

Barry, D., & McDonald, S. (2012). Climate change or climate cycles? Snowpack trends in the Olympic and Cascade Mountains, Washington, USA. Environmental Monitoring and Assessment, 185(1), 719–728. https://doi.org/10.1007/s10661-012-2587-z

Demaria, E. M., Nijssen, B., & Wagener, T. (2007). Monte Carlo sensitivity analysis of land surface parameters using the Variable Infiltration Capacity model. Journal of Geophysical Research: Atmospheres, 112(D11), D11113–n/a. https://doi.org/10.1029/2006JD007534

Dong, C., & Menzel, L. (2016). Producing cloud-free MODIS snow cover products with conditional probability interpolation and meteorological data. Remote Sensing of Environment, 186, 439.

Guevara, M., Taufer, M., & Vargas, R. (2021). Gap-free global annual soil moisture: 15 km grids for 1991-2018. Earth System Science Data, 13(4), 1711–1735. https://doi.org/10.5194/essd-13-1711-2021

Haddeland, I., Matheussen, B. V., & Lettenmaier, D. P. (2002). Influence of spatial resolution on simulated streamflow in a macroscale hydrologic model. Water Resources Research, 38(7), 29–29–10. https://doi.org/10.1029/2001WR000854

Hall, D. K., & Riggs, G. A. (2007). Accuracy assessment of the MODIS snow products. Hydrological Processes, 21(12), 1534-1547. doi:10.1002/hyp.6715

Hall, D. K. & Riggs, G. A. (2016). MODIS/Terra Snow Cover Daily L3 Global 500m Grid, Version 6. [NDSI snow cover]. Boulder, Colorado USA. NASA National Snow and Ice Data Center Distributed Active Archive Center. doi: https://doi.org/10.5067/MODIS/MOD10A1.006. [January 2017 - July 2021].

Hall, D. K., Riggs, G. A., Digirolamo, N. E., & Roman, M. O. (2019). Evaluation of MODIS and VIIRS cloud-gap-filled snow-cover products for production of an Earth science data

record. Hydrology And Earth System Sciences, 23(12), 5227–5241. https://doi.org/10.5194/hess-23-5227-2019.

Hock, R. (2003). Temperature index melt modelling in mountain areas. Journal of Hydrology, 282(1), 104-115. doi:10.1016/S0022-1694(03)00257-9

Jensen, J. (2016). Introductory Digital Image Processing: A Remote Sensing Perspective (4th ed.).

Kasurak, A., Kelly, R., Brenning, A., & Pelto, Mauri S. (2011). Linear mixed modelling of snow distribution in the central Yukon. Hydrological Processes, 25(21), 3332–3346. https://doi.org/10.1002/hyp.8168

Klein, A. G., & Barnett, A. C. (2003). Validation of daily MODIS snow cover maps of the Upper Rio Grande River Basin for the 2000–2001 snow year. Remote Sensing of Environment, 86(2), 162–176. https://doi.org/10.1016/S0034-4257(03)00097-X

König, M. & Sturm, M. (1998). Mapping snow distribution in the Alaskan Arctic using aerial photography and topographic relationships, Water Resour. Res., 34(12), 3471–3483, https://doi.org/10.1029/98WR02514

Luce, C. H., & Tarboton, D. G. (2004). The application of depletion curves for parameterization of subgrid variability of snow. Hydrological Processes, 18(8), 1409-1422. https://doi.org/10.1002/hyp.1420

Martinec, J., Rango, A., & Major, E. (1983). Snowmelt Runoff Model (SRM) User's Manual; New Mexico State University: Las Cruces, NM, USA, 2008.

Mote, P. W. (2003). Trends in snow water equivalent in the Pacific Northwest and their climatic causes. Geophysical Research Letters, 30(12), 1601–n/a. https://doi.org/10.1029/2003GL017258

Nourani, V., Afkhaminia, A., Andaryani, S., & Zhang, Y. (2021). Multi-station calibration strategy for evaluation and sensitivity analysis of the snowmelt runoff model using MODIS satellite images. Hydrology Research, 52(6), 1389–1404. https://doi.org/10.2166/nh.2021.075

Parajka, J. & Blöschl, G. (2006). Validation of MODIS snow cover images over Austria, Hydrol. Earth Syst. Sci., 10, 679–689, https://doi.org/10.5194/hess-10-679-2006

Parr, C., Sturm, M., & Larsen, C. (2020). Snowdrift landscape patterns: An Arctic investigation. Water Resources Research, 56, e2020WR027823. https://doi.org/10.1029/2020WR027823

Pasquale, N., Perona, P., Wombacher, A., & Burlando, P. (2014). Hydrodynamic model calibration from pattern recognition of non-orthorectified terrestrial photographs. Computers & Geosciences, 62, 160–167. https://doi.org/10.1016/j.cageo.2013.06.014

Qiu, L., You, J., Qiao, F., & Peng, D. (2014). Simulation of snowmelt runoff in ungauged basins based on MODIS: A case study in the Lhasa River basin. Stochastic Environmental Research and Risk Assessment, 28(6), 1577–1585. https://doi.org/10.1007/s00477-013-0837-4

Rango, A. (1988). Progress in Developing an Operational Snowmelt-Runoff Forecast Model with Remote Sensing Input. Hydrology Research, 19(2), 65–76. https://doi.org/10.2166/nh.1988.0005

Riggs, G.A., Hall, D. K., & Roman, M. O. (2017). Overview of NASA's MODIS and Visible Infrared Imaging Radiometer Suite (VIIRS) snow-cover Earth System Data Records. Earth System Science Data, 9(2), pp.765–777. doi:10.5194/essd-9-765-2017

Schlogl, S., Lehning, M., Fierz, C., & Mott, R. (2018). Representation of Horizontal Transport Processes in Snowmelt Modeling by Applying a Footprint Approach. Frontiers in Earth Science, 6, Frontiers in Earth Science, Oct 8, 2018. https://doi.org/10.3389/feart.2018.00120

Shen, C. (2018). A transdisciplinary review of deep learning research and its relevance for water resources scientists. Water Resources Research, 54, 8558–8593. https://doi.org/10.1029/2018WR022643

Siemens, K., Dibike, Y., Shrestha, R., & Prowse, T. (2021). Runoff Projection from an Alpine Watershed in Western Canada: Application of a Snowmelt Runoff Model. Water (Basel), 13(9), 1199. https://doi.org/10.3390/w13091199

Stewart, I., Cayan, T., & Dettinger, D. (2004). Changes in snowmelt runoff timing in western North America under a `business as usual' climate change scenario. Climatic Change, 62(1-3), 217–232. https://doi.org/10.1023/B:CLIM.0000013702.22656.e8

Sturm, M., & Wagner, A. (2010). Using repeated patterns in snow distribution modeling: An Arctic example. Water Resources Research, 46(12), N/a. https://doi.org/10.1029/2010WR009434

Troy, T. J., Wood, E. F., & Sheffield, J. (2008). An efficient calibration method for continental-scale land surface modeling. Water Resources Research, 44(9), W09411–n/a. https://doi.org/10.1029/2007WR006513

Wang, X., & Xie, H. (2009). New methods for studying the spatiotemporal variation of snow cover based on combination products of MODIS Terra and Aqua. Journal of Hydrology, 371(1), 192-200. https://doi.org/10.1016/j.jhydrol.2009.03.028

Woodruff, C. D., & Qualls, R. J. (2019). Recurrent snowmelt pattern synthesis using principal component analysis of multiyear remotely sensed snow cover. Water Resources Research, 55. https://doi.org/10.1029/2018WR024546

Chapter 6: Concluding Remarks

In this work we have discussed the importance of snow and the utility of remote sensing to extract spatial patterns. The existence of a pattern has long been accepted however we are the first to utilize it beyond cloud removal. The recurrent pattern of snowmelt has significant advantages in simplifying snowmelt. The literature and hydrologic community use remote sensing as a data source for measurement and in many cases, it is regarded as a lesser data source. We have demonstrated throughout this work that remote sensing also can be used to develop a model.

The spatio-temporal model of the recurrent pattern of snowmelt not only accurately represents the spatial depletion of snow but also describes snowmelt linearly with time. We provided a thorough analysis of the linearity of the time component. Secondary snowfall events impact the timing of snowmelt, but only as a brief interruption. Overall, the spatial component is intrinsically tied to the temporal component of snowmelt. Snowmelt has been viewed as temporally variable, but we simplified it into a linear regression.

Development of a pattern is completed with a Principal Component Analysis throughout most of this work however other methods can be applied. A K-means clustering analysis also can produce a model of the recurrent pattern. This method is hindered by the discrete steps identified by the number of clusters defined by the user. User decisions hinder the K-means clustering model, but they are also an important consideration in the PCA method. We found that a slight alteration to the previously published PCA model NDSI snow cover threshold value led to significant increases in spatial accuracies. These analyses communicate the importance and sensitivity of big data models to simple decision such as what we consider snow.

Finally, we investigated spatial and temporal scaling questions. We demonstrated the PCA model can be applied to HUC-6 watershed sizes with exceptional accuracies. We also provided an analysis of the changes in the resulting PCA model dependent on the number of years used to develop the model. While these findings were area specific, they provide insight into some good practices for developing the PCA model of the recurrent pattern of snowmelt.

The spatial and temporal pattern of snowmelt is investigated in depth in this dissertation. The impact this work could have on how we approach climate change is significant. Although we expect to see changes to the mean temperature and precipitation the year-to-year variability we captured in our study period suggests the pattern will remain the same under a changing climate. So long as snow accumulation leads to a winter snowpack the pattern will exist. The work in Chapter 5 discussed the

ability of the PCA model to extract the pattern in a watershed which did not see complete snow coverage (Middle Snake Boise). The pattern for the mountainous sub basin was extracted and nearly equivalent using only the sub basin as input and using the whole watershed as input. There is potential to use this methodology to track the changes, to plant succession for example, under climate change. Given sufficient years we can recalculate the PCA model and compare changes in the melt timing. Similarly, we can quantify from a spatio-temporal normalized perspective the elevational zones and aspects subject to the most change under climate change. These potential applications require more research but given the robust nature of the pattern they are avenues of application.

The work completed in this dissertation identifies theoretical applications, sensitivities, and scaling all with validated spatial accuracy assessments against independent data. These are foundational steps necessary to expand and apply this method world-wide. This emerging field of spatial patterns of snowmelt has the potential to alter how we approach snowmelt modeling in real-time and under climate change simply because we can normalize snowmelt across years.